University of Liège

Faculty of Applied Sciences

Master thesis

Study of passive and active attitude control systems for the OUFTI nanosatellites

Supervisor : Prof. Christophe Geuzaine

Vincent Francois-Lavet
2^{nd} Master in Engineering Physics

Academic Year 2009 – 2010

Acknowledgments

My first thanks go to my supervisor Prof. Christophe Geuzaine for his availability and the pick discussions we had together. The numerous advices he gave me were of considerable help for this thesis. I would also like to thank Prof. Gaëtan Kerschen for his availability and for the several good reference works he provided me. I am also grateful to Sébastien Hoffait and Prof. Olivier Brüls for their efficient help on the dynamical effects of the antenna's deployment. In addition, I want to warmly thank Samuel Hannay for his help in continuing the good work he had done during the previous academic year. I also thank David Colignon and Prof. Christophe Geuzaine who gave me accesss to a computer unit to perform the most time-consuming simulations. I also warmly thank Jasper Bouwmeester, the Delfi-C3 project manager, for the precious documentation he gave me as well as Muriel Noca, the SwissCube project manager, for the interesting discussion on the hypotheses of the high rotation rate which SwissCube experiences since its launch.

I also wish to thank all the master students involved in this inovative and exciting project: Kerem Can, Nicolas Crosset, Nicolas François, Mirko Heukemes, Marie Kolodziej, Nicolas Marchal, Ngoc An Nguyen, Jean-Yves Nicolas, Jean-Philippe Noël, Loïc Questiaux, Ludovic Renson and Julien Tallineau. I also want to thank all the members of the OUFTI team: the project manager, Amandine Denis, and the system engineering team, Jonathan Pisane, Laurent Chiarello, Laurent Rainaut and last but not least Jérôme Wertz. In addition, I would like to thank Prof. Pierre Rochus and Prof. Jacques Verly for their implication in the project.

Finally, I would like to thank Jean-Francois Kaisin who kindly accepted to proofread this master thesis as well as my family for their continuous support.

May 2010
Vincent Francois-Lavet

Contents

List of Symbols

General symbols

B : Magnetic flux density [T]
B_r : Remanent Induction [T]
B_s : Saturation Induction [T]
c : Speed of light in vacuum [$= 1/\sqrt{\epsilon_0 \mu_0} = 2.99792458\ 10^8$ m/s]
e : elongation
j : Current density [A/m^2]
H : Magnetic field [A/m]
H_c : Coercive Field [A/m]
N_d : Demagnetizing factor
m : Masse [kg]
M : Magnetization [A/m]

Greek symbols

α : Angle between the magnetic field lines and the permanent magnet
Γ : Boundary of Ω [$= \partial\Omega$]
Δ : Laplace operator
ϵ_0 : Electric permittivity of vacuum [$\approx 8.854187817\ 10^{-17}$ F/m]
μ_0 : Magnetic permeability of vacuum [$= 4\pi\ 10^{-7}$ H/m]
μ_r : Relative magnetic permeability [$= \mu/\mu_0$]
ρ : Volumic mass [Kg/m^3]
ϕ : Magnetic scalar potential [A]
χ_m : Magnetic susceptibility
Ω : Bounded open set of E3

Tensors and vectors

$\boldsymbol{F}$: Force [N]
I : Inertia Tensor [$kg.m^2$]
$\boldsymbol{L}$: Angular momentum [N.m.s]
$\boldsymbol{r}$: Position vector (represents the position of a point in a given reference frame) [m]
$\boldsymbol{T}$: Torque [N.m]
$\boldsymbol{v}$: velocity vector[m/s]
$\boldsymbol{\mu}$: Magnetic moment [$A.m^2$]

Abbreviations

ACS : Attitude Control System
ADCS : Attitude Determination and Control System
BNC : Beacon
COM : Communication
CPU : Central Process Unit
D-STAR : Digital Smart Technology for Amateur Radio.
ECI : Earth Centered Inertial
ECEF : Earth Centered Earth Fixed
EPS : Electrical Power System
FOV : Field Of View
GPS : Global Positioning System
LEO : Low Earth Orbit
LQR : Linear Quadratic Regulator
MEMS : Micro-Electro-Mechanical System
MOEMS : Micro-Opto-Electro-Mechanical System
NED : North-East-Down
OBC : On-Board-Computer
PID : Proportional-Integral-Derivative controller
PMAS : Passive Magnetic Attitude Stabilisation
P-POD : Poly Picosatellite Orbital Deployer
PSLV : Polar Satellite Launch Vehicle
RMI : Royal Meteorological Institute of Belgium
RPM : Rotations per minute
SRP : Solar Radiation Pressure
ULg : University of Liege

Operators

$\frac{d\circ}{dt}$ or $\dot{\circ}$: Time derivative
$grad$: Gradient
$curl$: Curl
div : Divergence
$\wedge$: Cross product
$\cdot$: Scalar product

Abstract

The university of Liege is currently developing the first nanosatellites ever made in Belgium : OUFTI-1 and OUFTI-2. The satellite conception is led by students supported by professors and a system engineering team formed by teaching assistants and PhD students. The objectives of the nanosatellite projects are to provide hands-on experience in space applications and to design a satellite which will serve for a variety of space experiments.

OUFTI-1 is a cube with a size of $10 \times 10 \times 10 cm$ and a weight of at most one kilogram. It is the first satellite equipped with a recently-developed amateur radio digital-communication protocol: the D-STAR technology. Other experiments that will fly aboard OUFTI-1 are an innovative electrical power system as well as high-performance solar cells. The satellite is not required to point in one specific direction and the Attitude Determination and Control System (ADCS) subsystem relies on Passive Magnetic Attitude Stabilization (PMAS). The first part of this thesis presents this design made of a permanent magnet and hysteretic bars. The magnet orients the satellite along the Earth's magnetic field lines and the hysteretic bars damp its rotational velocities. The influence of the magnet on the hysteretic bars as well as the finite elongation of the bars are carefully studied.

OUFTI-2 is the next satellite in the series. Its size is planned to be twice the size of OUFTI-1 and its main payload will be a radiometer to perform a direct measurement of the net heating of the Earth. The radiometer is developed in cooperation with the Royal Meteorological Institute of Belgium and is called Sun-earth IMBAlance (SIMBA) radiometer. The second part of this master thesis focuses on the feasibility study of an active attitude control system which satisfies the requirements of the payload.

1 Introduction

1.1 The CubeSat concept

Technological development gives the opportunity to create ever-smaller scale devices. The miniaturization trend in many fields of technology has opened new possibilities for space applications. While bigger-scale satellites must use special materials which take many years of design and must be space qualified, the miniaturization provides many advantages. Smaller-scale satellites are launched as auxiliary payloads at reduced costs. In addition, smaller satellites can afford the luxury of using commercial off-the-shelf elements, and they can be entirely designed in one or two years. The lower launch costs and easier design make them very attractive for space experiments.

One of the last breakthrough in simplifying the access to space at lower cost is the CubeSat concept. The CubeSat standard addresses all the critical issues from test and integration procedures, to the dimensions of the satellite and to the CubeSat-specific Poly-Picosatellite Orbital Deployer launcher (P-POD).

The CubeSat satellites lie between the classes of nano-satellites (0.1 to 1 Kg) and pico-satellites (1 to 10 Kg). They have all a square $10 \times 10cm$ cross section so that they can all be launched and deployed using a common deployment system. The standard $10 \times 10 \times 10$ cm basic CubeSat is often called "one unit". CubeSat standards such as "two units" ($10 \times 10 \times 20$) and "three units" ($10 \times 10 \times 30$ cm) also exist.

The concept of CubeSat began in 1999 at California Polytechnic State University (Cal Poly) and Stanford University. A few companies have built CubeSats, but the majority of development come from academies. One of the advantages of CubeSat is to be an ideal tool for educational programs. It actually provides easy access to space, and it is a viable option for high schools and universities across the world. With this concept, students gain a valuable hands-on education in space applications.

1.2 The OUFTI family

The OUFTI nanosatellites meet the CubeSat standards, and they all started with OUFTI-1 in 2007. University of Liège (ULg) is now involved in the final phase of de-

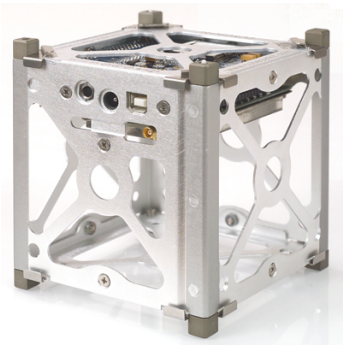

Figure 1.1 – *The "one unit" CubeSat structure provided by Pumpkin* and used for OUFTI-1

sign of the OUFTI-1 nanosatellite, and two other projects are scheduled. It is planned to develop the OUFTI-2 nanosatellite in collaboration with the Royal Meteorological Institute and one satellite within the QB50 constellation proposed by the Von Karman Institute.

1.2.1 OUFTI-1

OUFTI-1 is the first nanosatellite from the ULg, as well as the first nanosatellite ever developed in Belgium. It is a "one unit" CubeSat which is scheduled to be launched on the maiden flight of Vega as one of the secondary payloads. The nanosatellite project has an educational goal, and it will also serve for several space experiments.

OUFTI-1's mission will be a technology demonstration mission. The three main innovations are

- An amateur radio digital-communication protocol: D-STAR. This technology will be made available to ham-radio operators worldwide.
- High-efficiency solar cells from Azurspace.
- An experimental and innovative digitally-controlled electrical power system proposed by Thales Alenia Space ETCA.

1.2.2 OUFTI-2

The university of Liège recently undertook the conception of a new and ambitious satellite which will be called 'OUFTI-2'. The OUFTI-2 project was started recently, and it is currently in the first phase of development. The feasibility study is undertaken, and the requirements are being defined.

1.3 Attitude Determination and Control System

The attitude is the orientation of a body fixed coordinate frame with respect to an external frame. The Attitude Determination and Control System (ADCS) is made of two different parts : attitude determination and attitude control.

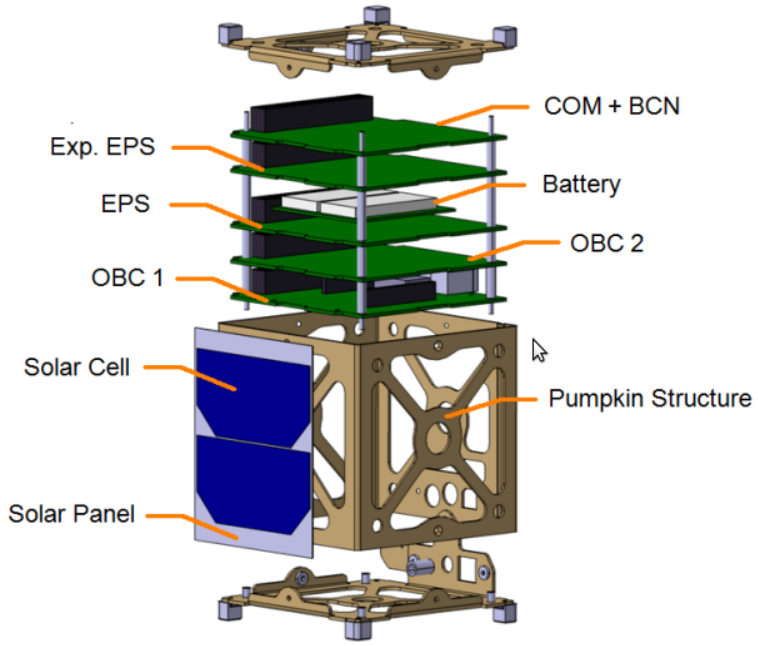

Figure 1.2 – *Exploded view of OUFTI-1 nanosatellite (Reference [1])*

Attitude determination refers to the process of measuring and determining spacecraft orientation. For OUFTI-1, an accurate attitude determination is not necessary, and the use of solar panels on the sides of the satellite will allow an estimation of the attitude. For OUFTI-2, sensors as well as an on-board algorithm which provides attitude estimation from the measurements have to be used. A wide variety of attitude determination hardware is available, and a short overview of the possibilities for a nanosatellite will be presented.

Attitude control refers to the process of orienting the spacecraft in the given direction. It is accomplished using a wide variety of techniques. The requirements for pointing accuracy, stability, and manoeuvrability, as well as other mission requirements such as cost, weight, reliability, orbital motion and lifetime are the key parameters which drive the decision of which technique to use. The various techniques can be grouped according to whether the applied torques are passive or active.

1.3.1 Passive attitude control and OUFTI-1

The nanosatellite OUFTI-1 does not require high-precision orientation or specific manoeuvres during the flight. Passive attitude controls are in that condition the best solution. They have the advantages of being robust, cheap, simple, light and consuming no power. Moreover it does not require attitude determination to work properly. It has however limited pointing accuracy, and it gives very tiny choices on the pointing direction.

There exists two main passive control types for satellites. The first one uses gravity gradient, and it leads to two stable states with the long axis (axis with smallest moment of inertia) pointing towards the Earth. The other passive system orients the satellite along the earth magnetic field thanks to a magnet. In the case of OUFTI-1, the use of gravity gradient would complicate heavily the design. The chosen method was therefore the alignment parallel to the magnetic field thanks to a magnet.

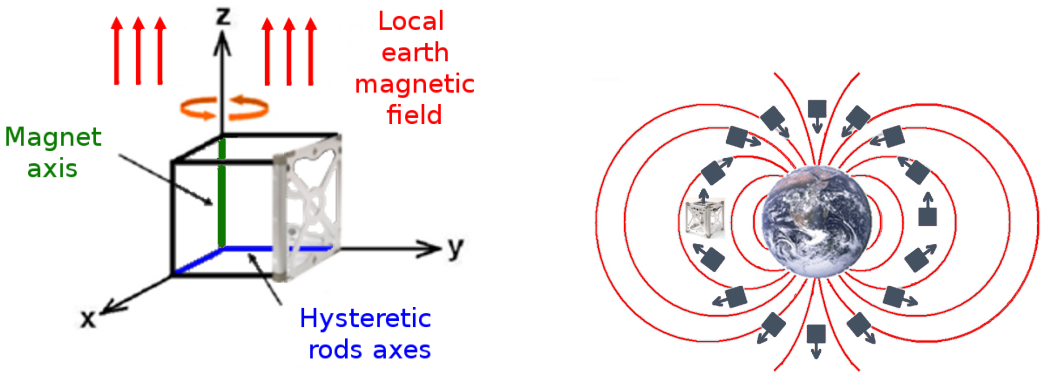

Figure 1.3 – *Passive ACS : the satellite's orientation follows the Earth's magnetic lines*

Unless some means of damping is provided, the spacecraft will oscillate around energy minima. This drawback is overcome by adding a damper. The damper will convert oscillation and rotation energy into heat. A good damping method for Low Earth Orbit spacecraft is the use of hysteretic materials.

The Passive Magnetic Attitude Stabilisation (PMAS) requires a fine mathematical simulation of the hysteresis phenomenon and of the satellite dynamics. Moreover, there are strict requirements on the arrangement of the hysteresis materials and the magnet in the satellite.

1.3.2 Active attitude control and OUFTI-2

Active attitude control is needed for more stringent requirements. The system uses attitude sensors as well as a control algorithm to determine the current attitude, and it uses control actuators to perform attitude manoeuvres and to compensate for the disturbance torques. There are two main types of active control :

- *Spin-stabilized* : the satellite is spun like a top around the axis that one wishes to maintain in a given direction. The satellite resists small perturbing torques and keep its orientation in the inertial space due to conservation of angular momentum. However the constant spin is less practical for payloads and communication for instance.
- *Three-axis stabilized* : the satellite attitude is fully determined and controlled.

Active attitude control is a wide subject which involves a variety of different fields. It is a combination of dynamics and control.

1.4 Outline of the thesis

Chapter 2 presents the basis for any attitude control system. The thesis is then divided in two main parts. The first part (mainly chapter 3) presents the work performed within the framework of the PMAS of OUFTI-1. It is built on the basis of the work performed by Samuel Hannay for the ADCS of OUFTI-1 during the academic year 2008-2009 (Reference [2]). The second part (chapters 4 to 5) presents a feasibility study for the active control of the OUFTI-2 nanosatellite project.

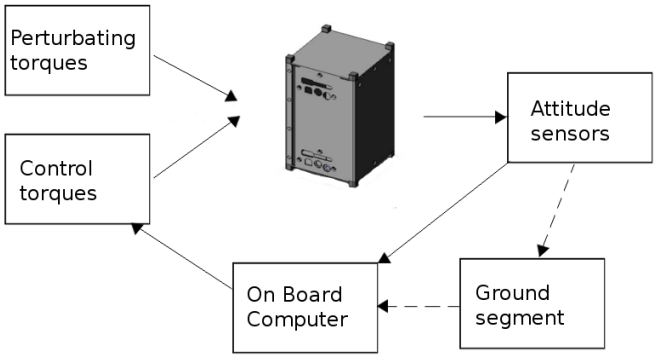

Figure 1.4 – *Bloc diagram of an active Attitude Control System*

The first part consists in defining the final design of the OUFTI-1 nanosatellite. The design has to fulfil mission requirements which take into account efficiency, mass concerns and room constraints. Various aspects are studied in this master thesis to model the exact behaviour accurately. The elongation of the rods as well as the influence of the magnet on the hysteresis bars efficiency are carefully studied. Thanks to this analysis, the likely reasons for the reduced efficiency that the nanosatellite Delfi-C3 has experienced are determined. Finally, the choice of the design and of materials for OUFTI-1 is defined.

The second part deals with the feasibility study of an active control for the OUFTI-2 nanosatellite. The requirements are defined in collaboration with the Royal Meteorological Institute of Belgium and ULg. The different solutions are afterwards examined taking into account simplicity, reliability as well as room and mass concerns.

2

Mathematical modelling and Coordinate systems

The content of this chapter is the basis for any attitude control system. A mathematical model of OUFTI-1 and its environment was developed in a large part during the academic year 2008-2009 by Samuel Hannay (Reference [2]). In this chapter, the main equations are recalled and several additional informations are presented. The equations of motion are developed, and the definitions of the different useful coordinate systems are given. Finally, the different environmental torques are described.

2.1 Equations of motion

Dynamics is the study of the relationships between forces and motion. There are two major divisions in space sciences : *celestial or orbit dynamics* and *attitude dynamics*. In this master thesis we are mainly interested in the latter.

Celestial dynamics deals with translation motions, and it is described by two first-order ordinary differential equations.

$$m\frac{d\boldsymbol{v}}{dt} = \boldsymbol{F}_{fictitious} + \boldsymbol{F}_{total}$$

$$\frac{d\boldsymbol{r}}{dt} = \boldsymbol{v}$$

The apparent force $\boldsymbol{F}_{fictitious}$ appears in a non-inertial frame of reference, such as a rotating reference frame.

Attitude dynamics deals with the motion around the centre of mass. The equation which governs attitude dynamics is

$$\frac{d\boldsymbol{L}}{dt} = \boldsymbol{T}_{tot} \tag{2.1}$$

where $\boldsymbol{T}_{tot}$ is the total torque acting onto the satellite, and $\boldsymbol{L}$ is the total angular momentum. For a rigid body, $\boldsymbol{L} = \mathrm{I}\boldsymbol{\omega}$ with I being the moment of inertia tensor.

The operator equation acting on a given vector $\boldsymbol{A}$ which links the rate of change in an inertial coordinate system and the rate of change as observed in a rotating coordinate system with angular velocity $\boldsymbol{\omega}$ (body axes for instance) is

$$\left[\frac{d\boldsymbol{A}}{dt}\right]_i = \left[\frac{d\boldsymbol{A}}{dt}\right]_b + \boldsymbol{\omega} \wedge \boldsymbol{A}$$

This allows to describe Equation 2.1 in the well-known following form

$$\left[\frac{d\boldsymbol{L}}{dt}\right]_b = \boldsymbol{T}_{tot} - \boldsymbol{\omega} \wedge \boldsymbol{L} \tag{2.2}$$

The total torque $\boldsymbol{T}_{tot}$ is composed of disturbance torques and control torques.

If principal axes are used, the angular momentum of a rigid body can be expressed as

$$L = [I_{xx}w_x, I_{yy}w_y, I_{zz}w_z]$$

Equation 2.2 leads then to

$$\begin{cases} I_{xx}\frac{d\omega_x}{dt} - (I_{yy} - I_{zz})\omega_y\omega_z = T_x \\ I_{yy}\frac{d\omega_y}{dt} - (I_{zz} - I_{xx})\omega_z\omega_x = T_y \\ I_{zz}\frac{d\omega_z}{dt} - (I_{xx} - I_{yy})\omega_x\omega_y = T_z \end{cases}$$

From these equations it may be seen that cross-coupling will happen, which means that angular acceleration does not take place solely about the torque axis. However for small angular velocities and similar principal moments of inertia the responses about these axes are in a good approximation uncoupled. We get

$$I_{xx}\frac{d\omega_x}{dt} = T_x, I_{yy}\frac{d\omega_y}{dt} = T_y, I_{zz}\frac{d\omega_z}{dt} = T_z$$

Matlab and Simulink will be used to simulate the attitude behaviour. The "6DoF (Quaternion)" blockset from the Simulink library is the central part of the built simulator. This blockset performs the resolution of these equations given the applied forces, applied torques and system properties (as initial velocity, inertia matrix, ...). The inputs and outputs of this blockset are given in Table 2.1.

2.2 Coordinate systems

In this section we will introduce different frames necessary to the modelling of the attitude. For example the torques will be described in body axes whereas positions will first be calculated in an Earth-centred frame.

2.2.1 The Earth-Centred Inertial frame (ECI)

The origin of the frame is located at the centre of the Earth, and it does not rotate with it. That frame is a pseudo inertial frame in which Newton's laws are valid as a first approximation. We ignore the Sun's acceleration in the Galaxy and the Galaxy's acceleration through cosmos. In our purpose, this is a good approximation.

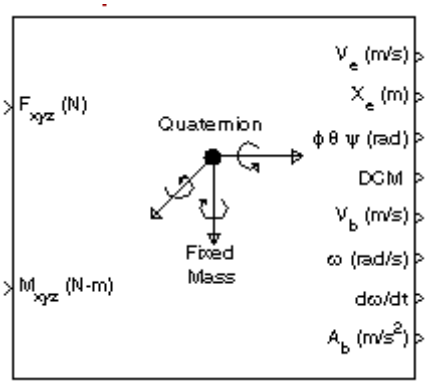

Figure 2.1 – *"6DoF (Quaternion) blockset"*

Type	Description
Input Vector	Three applied forces in body frame
Input Vector	Three applied moments in body frame
Output Vector	Velocity in the ECI reference frame
Output Vector	Position in the ECI reference frame
Output Vector	Euler rotation angles [roll, pitch, yaw], in radians
3-by-3 matrix	Coordinate transformation from ECI axes to body-fixed axes
Output Vector	Velocity in the body-fixed frame
Output Vector	Angular rates in body-fixed axes, in radians per second.
Output Vector	Angular accelerations in body-fixed axes, in radians
Output Vector	Accelerations in body-fixed axes.

Table 2.1 – *Inputs and Outputs of the Simulink blockset "6DoF (Quaternion)" (Reference [3])*

The ECI frame is defined as follow :

- The z-axis points towards the North Pole.
- The chosen convention uses the x-axis that points towards vernal equinox (see Figure 2.2). This convention make the ECI frame perfectly inertial if we suppose an inertial Sun. Another convention uses the x-axis which points towards the Sun. This frame leads to slightly less accurate results because it ignores the Earth's acceleration around the Sun.
- The y-axis completes the right hand Cartesian coordinate system

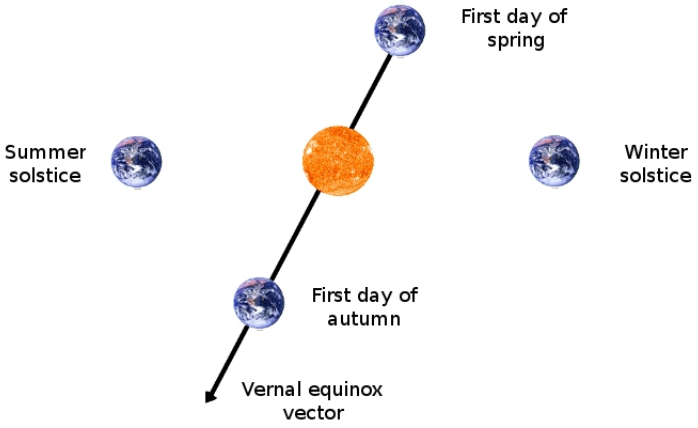

Figure 2.2 – *Vernal equinox representation*

2.2.2 The Earth-Centered Earth Fixed frame (ECEF)

This non-inertial frame has the same origin and z-axis as ECI, but the x- and y-axes rotate with the Earth relative to the ECI frame. The x-axis intersects the Earth's surface at latitude and longitude (0° ,0°). As showed in Figure 2.3, that frame rotates relatively to the ECI frame at a rotation speed [1] of

$$\Omega = \frac{2 \cdot \pi}{sidereal\ day} = 7.2921 \cdot 10^{-5} rad/s$$

.

2.2.3 Body frame

The body frame is a non-inertial coordinate system fixed in both origin and orientation to the satellite. Its origin is placed at its centre of mass. The orientation and the angular velocities are conveniently expressed in the body frame.

[1] If we had chosen an ECI frame with the x-axis pointing towards the Sun,

$$\Omega = \frac{2 \cdot \pi}{mean\ solar\ day} = 7.2722 \cdot 10^{-5} rad/s$$

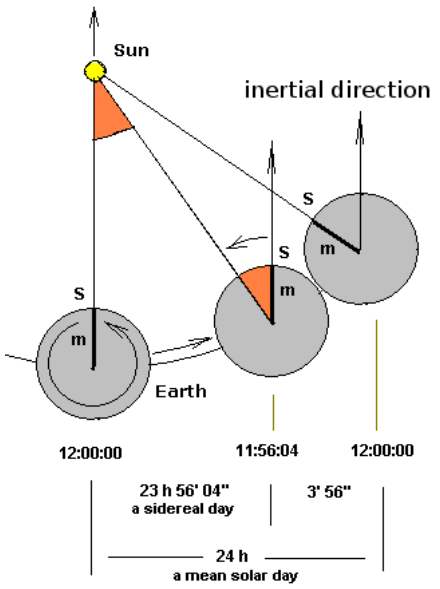

Figure 2.3 – *ECI and ECEF frames*

2.2.4 The 'NED' coordinates

The north-east-down (NED) system is a non-inertial system with its origin fixed at the satellite's centre of gravity. Its axes are oriented along the geodetic directions defined by the Earth's surface.

- The x-axis points north parallel to the geoid surface.
- The y-axis points east parallel to the geoid surface, along a latitude curve.
- The z-axis points downward, towards the Earth's surface, and it completes the right hand Cartesian coordinate system.

2.3 Euclidean transformations

Some quantities are easily calculated in specific frames, and they must afterwards be translated into other frames for modelling purposes. These transformations from one system to another are described by Euclidean transformations.

2.4 Disturbance torques

Disturbance torques are torques caused by the environment, which prevent the satellite from staying in a given orientation as seen from an inertial frame. Torques can be classified into two kinds : cyclic torques and secular torques. On the one hand, cyclic torques have no null frequency torque contribution. They prevent a satellite from remaining pointed in a given direction, and they tend to give birth to oscillations in the satellite behaviour, but they do not imply an angular acceleration over time. On the other hand, secular torques

have a continuous torque contribution which tends to imply an angular acceleration over time. In a non-rotating satellite, environmental torques lead to secular torques that must be handled. On the contrary, a rotating spacecraft undergoes cyclic torques, which on average does not lead to angular acceleration.

In this section, the main disturbance torques are briefly exposed, and the main formulas are given. The calculation of disturbance torques implemented in the simulator is based on the work done by my predecessor Samuel Hannay in Reference [2], and some additional details are here discussed.

2.4.1 Atmospheric drag

The atmospheric force which acts on the satellite can be described with the following formula:

$$\boldsymbol{F}_{Drag} = \frac{1}{2}\rho S C_{Drag} V^2 \boldsymbol{e_V}$$

where ρ is the density of the atmosphere, S is call the 'master torque', C_{Drag} is the drag coefficient, V the speed of the satellite and $\boldsymbol{e_V}$ is the unit vector which points towards the velocity vector. The resulting torque is given by :

$$\boldsymbol{T}_{Aero} = (\boldsymbol{r_{cp}} - \boldsymbol{r_{gc}}) \wedge \boldsymbol{F_{Drag}}$$

where $\boldsymbol{r_{cp}}$ is the centre-of-pressure vector in body coordinates and $\boldsymbol{r_{gc}}$ the centre of gravity vector in body coordinates as well. The centre-of-pressure is at the centre of symmetry for simple satellite shapes.

The air density in low Earth Orbit depends on many parameters. It mainly depends on solar activity, diurnal and annual effects and geomagnetic activity. As can be seen in Figure 2.4, air density can vary by at least one order of magnitude. This makes it a very demanding task to get accurate estimations.

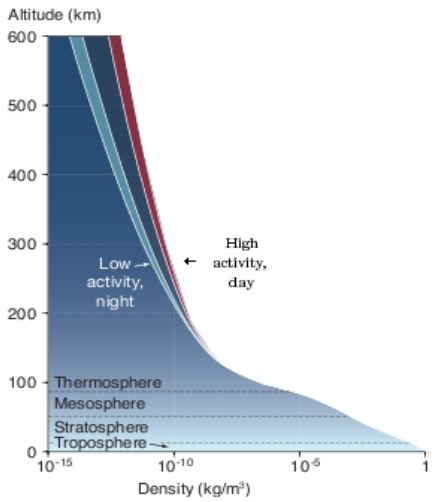

Figure 2.4 – *Air density as a function of altitude (Reference [4])*

The simulator will have two models implemented. It can use Harris Priester model or a simpler model with measurements done for a fixed local time of $10.5h$ and an average solar activity. The data of the simpler model come from Reference [5], and they can be seen in Figure 2.5.

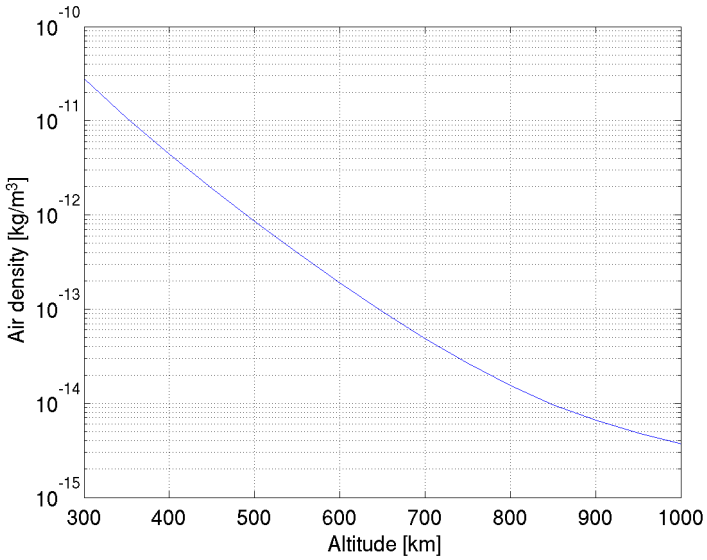

Figure 2.5 – *Air density as a function of altitude with seasonal and longitudinal average, a local time of* $10.5h$ *and an average solar activity*

2.4.2 Gravity gradient torque

Any non symmetrical object in orbit is subjected to a gravitational torque due to the variation of the Earth gravitational force onto the object. The gravitational force decreases as $\frac{1}{r^2}$ with r the distance from the centre of the Earth. This causes a satellite in orbit to experience a stronger attraction on its "lower" side than its "upper" side, and the satellite is therefore submitted to a gravity gradient torque. This environmental torque is given by the following formula :

$$\boldsymbol{T} = \frac{3\mu}{r^5}\boldsymbol{r} \wedge \underline{I}\boldsymbol{r}$$

where $\boldsymbol{r}$ is the position vector in an Earth-centred frame and μ is the Earth gravity constant $(3.986 \cdot 10^{14} m^3 s^{-2})$.

The gravity gradient torque depends on $1/r^3$ with r the distance from the satellite to the centre of the Earth. Figure 2.6 shows the relative dependence of the gravity gradient with altitude, and it can be seen that it is of the same order of magnitude for any low Earth orbit.

2.4.3 Solar pressure torque

Solar radiation pressure produces a force onto the satellite. The exact expression of the force acting onto the satellite depends on whether the incident radiations are absorbed, reflected specularly or reflected diffusely.

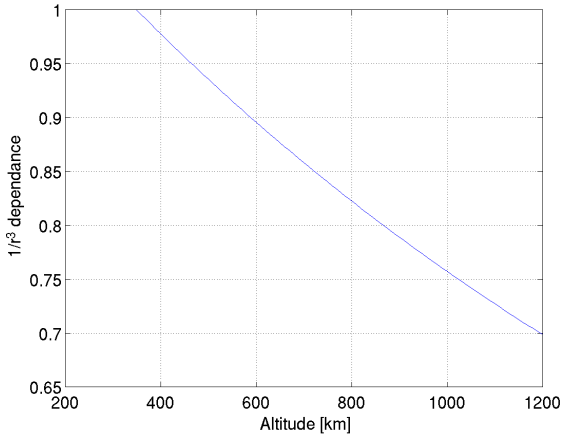

Figure 2.6 – *Relative decrease of the gravity gradient as a function of altitude*

For the absorbed radiations, the solar pressure $P_{absorption}$ acting on a surface normal to the Sun is given by the momentum flux of light P :

$$P_{absorption} = P = \frac{\Phi}{c}$$

where Φ is the power flux density, and c is the speed of light. A typical value for the power flux density of the Sun in orbit is $\Phi = 1370 W m^{-2}$. The radiation force due to the portion of the radiation that is completely absorbed is given by

$$df_{absorbed} = -PC_a cos\theta \boldsymbol{S} dA$$

where C_a is the absorption coefficient, θ is the incidence angle and $\boldsymbol{S}$ is the unit vector from the satellite to the Sun

For the reflected radiations, the solar pressure acting on a surface normal to the Sun is given by

$$P_{specular} = \frac{2\Phi}{c} = 2P$$

The radiation force due to the part of the radiation that is reflected specularly is given by

$$df_{specular} = -2PC_s cos^2\theta \boldsymbol{n} dA$$

where C_s is the specular reflection coefficient.

The radiation force due to the radiation that is reflected diffusely depends on the distribution of the radiation over all directions and is found by integrating the contribution of the reflected radiation over all angles. Assuming a Lambertian reflection with the intensity of the reflected light varying as $cos\theta$, the radiation force due to that portion of the radiation is given by

$$df_{diffuse} = -PC_d cos\theta (\boldsymbol{S} + \frac{2}{3}\boldsymbol{n}) dA$$

where C_d is the diffuse reflection coefficient.

The total force is found by summing up $df_{absorbed}$, $df_{specular}$, $df_{diffuse}$ over all lighted area. For an opaque surface (without transmission), it can be noted that $C_a + C_s + C_d = 1$.

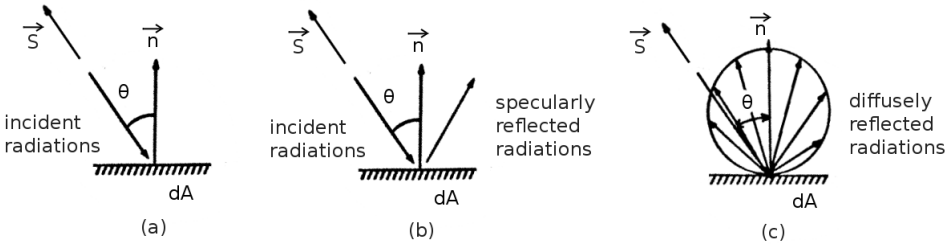

Figure 2.7 – *(a) Absorption, (b) Specular reflection (c) diffuse reflection*

The resulting torque is then calculated in the same way than in the case of the aerodynamic drag :

$$\boldsymbol{T}_{solar} = (\boldsymbol{r_{cp}} - \boldsymbol{r_{gc}}) \wedge \boldsymbol{F_{Drag}}$$

2.4.4 Comparison of the main disturbance torques

The aerodynamic torque decreases as an exponential with altitude whereas the gravity gradient torque depends on $1/r^3$ with r the distance from the satellite to the centre of the Earth. The gravity gradient is of the same order of magnitude for all low Earth orbit, and it becomes predominant for altitudes higher than about $500km$.

Torque sources	Dependence on the distance to the Earth centre r	Altitudes where it is dominant
Aerodynamic drag	$e^{-\alpha r}$	below 500km
Gravity gradient	$1/r^3$	500 to several thousands kilometres
Solar radiation	independent	Interplanetary space

Table 2.2 – *Disturbance torques dependences on altitude*

3

Passive ADCS of OUFTI-1

3.1 Introduction

This chapter presents the Passive Magnetic Attitude Stabilization (PMAS) that is developed for OUFTI-1. The goal is to align the satellite with the magnetic field direction thanks to a magnet, the damping being produced by hysteretic materials. The tolerable time of reaching the nominal motion must be no more than a month, and deviation from local earth magnetic field H should not exceed 10° to 15° after the stabilisation time.

The hysteresis phenomenon is at the heart of the chosen damping method. Hysteresis is a lag which occurs between the application of a field or a force and its subsequent effect. It occurs in the magnetic behaviour of materials, as well as in the mechanical behaviour for instance. For most of the hysteresis phenomena, the term "lag" shouldn't be interpreted as a time lag. In the magnetic hysteresis, it is the lag which appears between a varying magnetic field H and the subsequent magnetic induction B. That is equivalent to say that the magnetic induction depends on the current H-field and the previous magnetic states. The cover of a hysteresis loop is associated with energy loss, and it causes heating.

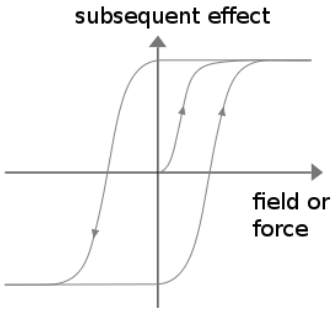

Figure 3.1 – *Illustration of the hysteresis cycle*

As the satellite rotates in low earth orbit, the hysteresis rods experience the earth magnetic field which varies along its length. The magnetization of the rod will then undergo a hysteresis cycle. Rotational motion will consequently be dissipated as heat, and it produces damping. The rate of loss per cycle is proportional to the area of the hysteresis loop, and

it is given by the equation

$$E = V \oint HdB$$

Requirements

The requirements that can be fixed for the attitude control of OUFTI-1 are

- An angle between the permanent magnet and the local earth magnetic field smaller than 30° after stabilization. The smaller the better.
- A stabilization time as short as possible.

Outline of this chapter

Section 3.2 lists the material possibilities which can be used in a PMAS, and Section 3.3 presents the main characteristics of a PMAS.

The in-orbit data obtained for the nanosatellites SwissCube and Delfi-C3 have been used as a basis to study the potential problems encountered for an attitude stabilization. SwissCube has experienced high initial rotational velocity and this threat is studied in details in section 3.4. Delfi-C3 showed an anomalous slow damping in orbit. Two reasons of efficiency reduction are identified in this master thesis and they are studied in section 3.5 and 3.6. The expected behaviour of the Delfi-C3 PMAS taking into account these two causes of efficiency reduction is then studied in Section 3.7.

Finally, OUFTI-1's case is treated. A practical design of a PMAS for OUFTI-1 is developed, and a method for attitude determination thanks to the solar panels is envisaged.

3.2 Material possibilities

3.2.1 Permanent magnet

The magnetic moment $\boldsymbol{\mu}$ of a magnet is expressed as :

$$\boldsymbol{\mu} = \boldsymbol{M}V \ [A.m^2]$$

where V is the volume, and M is the magnetization which is given by

$$\boldsymbol{B_r} = \mu_0 \boldsymbol{M}$$

Two different types of magnets have been considered : AlNiCo-5 and rare-earth magnets such as neodymium. Some important properties used to compare permanent magnets are:

- Remanence (B_r) : measures the strength of the magnetic field created by the magnet
- Coercivity (H_c) : the material's resistance to becoming demagnetized
- Mechanical properties

name	$\rho[g/cm^3]$	$H_c[A/m]$	$B_r[T]$
$AlNiCo-5$	$7,3$	$5,09 \cdot 10^4$	$1,25$
Neodyme Iron bore ($NdFeB$)	$7,5$	$1,500 \cdot 10^6$	$1,3$

Table 3.1 – *Magnet properties*

AlNiCo magnets are common and relatively cheap. They mainly consist of aluminium, nickel and cobalt hence their name of Al-Ni-Co. These components are either casted or sintered. Before the development of rare-earth magnets in the 1970s, they were the strongest type of magnet.

In general, Neodymium magnets have slightly higher remanence than AlNiCo magnets. However some brands of AlNiCo such as AlNiCo-5 are anisotropic, and they therefore have a comparable magnetic capacity in the preferred orientation. In conclusion, AlNiCo-5 has a remanence very close to the one of Neodymium, and that criterion is therefore not predominant.

Neodymium magnets have much higher coercivity than AlNiCo magnets. Materials with low coercive forces such as *AlNiCo-5 is easily demagnetized if not handled with care.* Bringing together poles in repulsion would lead to the loss of magnetization. For optimum performance of AlNiCo-5, the magnetic length should be approximately 5 times the other typical dimensions of the rod. If this geometry is used, the risk of demagnetization is lowered. This criterion is not predominant if it is carefully handled and stored.

AlNiCo and Neodymium magnets are hard and brittle. Special care must therefore be taken. Typical values of mechanical properties of these two kinds of magnets can be found in Reference [10].

In general, it is preferable to store magnetized materials under vacuum-sealed film so that the magnets do not collect ferromagnetic dust particles over time.

Cast AlNiCo-5 is the most commonly used of all the cast AlNiCo magnets. It has already been used in several PMAS in space.

Alnico-5 is chosen for its cost, its background in space applications and for its high remanent induction.

3.2.2 Hysteresis material

For the hysteretic bars, two different possibilities have been considered : Permenorm 5000 H2 and Hy-Mu-80. Table 3.2 lists the main properties of the two hysteretic materials.

The energy loss per cycle is proportional to the area of the hysteresis loop. If a full cycle is covered, the product $B_s \cdot H_c$ is an important parameter since it gives an approximation of the loss per cycle. That parameter is 7 times as important for Permenorm as for $Hy-Mu-80$. However the parameter $B_s \cdot H_c$ is only an indication since the cycle will not be covered fully due to the finite elongation of the rods as it will be explained in Section 3.5.

Quantity	$Hy - Mu - 80$	*Permenorm* 5000 *H2*
$\rho\ [g/cm^3]$	$8,747$	$8,25$
$H_c\ [A/m]$	$1,59$	5
$B_s\ [T]$	$0,73$	$1,55$
$B_r\ [T]$	$0,35$	$0,755$
$B_s \cdot H_c\ [J/m^3]$	$1,16$	$7,75$

Table 3.2 – *Hysteretic material properties*

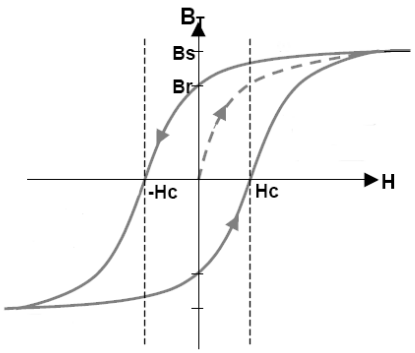

Figure 3.2 – *The hysteresis cycle*

Permenorm is a soft magnetic material alloy made of Nickel and Iron. "Anhyster", "Supranhyster" (societé Metallurg. d'Imphy, France) or "High Permeability 45" (Carpenter, USA) and others have similar characteristics. It has a sufficiently high permeability and a good coercive field. In other terms, it is an excellent candidate to provide significant damping. Moreover it has already been used in many other satellites (such as Delfi-C3, ESRO-1, ...).

The German company VACUUMSCHMELZE GmbH & Co. accepted to offer us sample rods with 4 mm diameter of Permenorm 5000 H2. The offer was accepted since the quantity of material required for OUFTI-1 PMAS is not enough to start dedicated production in any company. Shaping and heat treatment must however be performed.

3.3 Attitude Behaviour in orbit

3.3.1 Damping efficiency

The damping efficiency of the rods is determined by their volume and the material used, but other parameters have a significant impact. The scheme of their arrangement, the technique of heat treatment and their elongation drastically changes the PMAS efficiency.

The decrease rate in angular velocity can be characterized, and the importance of different parameters will then appear. With I the inertia moment in the $\boldsymbol{\omega}$ direction, the angular kinetic energy is given by

$$K_{rot} = \frac{1}{2} I \omega^2$$

Moreover if D is the energy dissipation per cycle, the time derivative of the angular kinetic energy is

$$\dot{K}_{rot} = -D\frac{\omega}{2\pi}$$

Therefore,

$$\begin{aligned}\dot{\omega} &= \frac{d\omega}{dK_{rot}}\frac{dK_{rot}}{dt} \\ &= \frac{-D}{2\pi I}\end{aligned}$$

The decrease rate in angular velocity is thus a linear function of time :

$$\omega(t) = \omega_0 - \frac{D}{2\pi I}t \tag{3.1}$$

That comes from the fact that K_{rot} is proportional to ω^2 and that the energy dissipation is proportional to ω.

The simple and optimistic case where the full hysteresis cycle is covered within one rotation is considered. Assuming the rough estimate for the energy dissipation per cycle of $4B_rH_c$, the energy dissipated per unit volume and per cycle is $15,1J/cycle/m^3$, which is a realistic value. On the one hand, a full hysteresis cycle has an energy dissipation often approximating $4B_rH_s$ which is about twice as important. On the other hand, minor loops due to the rotation around the hysteretic bar or along the magnetic field lines lead to less efficient damping. From this approximation, the time necessary to slow down by $0,1rad/s$ as a function of the hysteresis volume used is given in Figure 3.3.

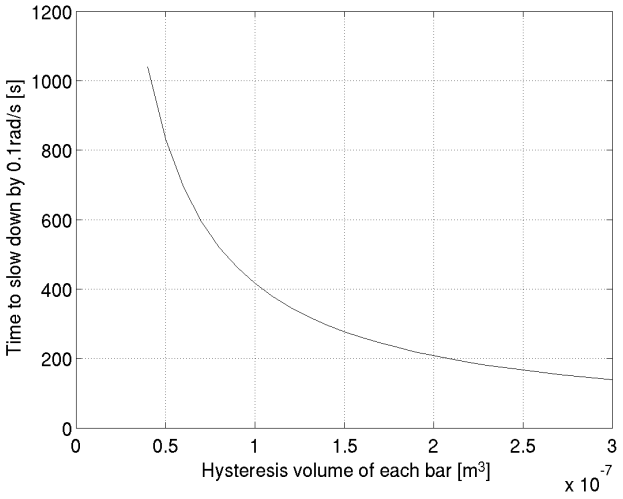

Figure 3.3 – *Stabilization time as a function of the hysteresis volume used with the approximation of the full cover of the hysteresis loop*

This approximation of the full cover of the hysteresis loop is used in many references ([12],[11], ...), but it can however be too optimistic by orders of magnitude because causes of efficiency reduction are not taken into account. These effects will be explained in Sections 3.5 and 3.6.

3.3.2 Final stabilization of the attitude

The orbital parameters for OUFTI-1 as well as OUFTI-1's mass distribution parameters necessary for the attitude simulations are given in Appendix A.1. The block diagram for the attitude simulations is given in Appendix A.2.

The target equilibrium is to align the permanent magnet axis with the Earth's magnetic field lines. The remaining angle between the magnet and the field lines after stabilization is called the system resolution. That angle is mainly due to the magnetic moment created by the hysteretic material. It adds to the magnetic moment of the permanent magnet and deviates it by an angle α given by

$$\alpha = \arccos\left(\frac{\left|\vec{\mu_{magnet}}\right|}{\left|\vec{\mu_{tot}}\right|}\right) \tag{3.2}$$

A trade-off between a fast damping and the obtained remaining angle can be a decisive criterion to determine the volume of hysteretic material used.

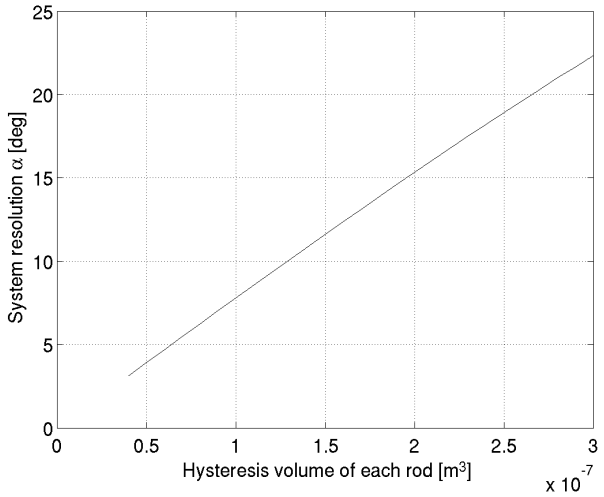

Figure 3.4 – *System resolution as a function of the hysteresis volume considering the use of Permenorm 5000 H2 material as hysteretic bar with B_r being $0,755T$*

As damping happens, the angle θ between the magnetic field lines and the permanent magnet's direction decreases to reach the system resolution α. Before any damping, an angle θ of about 90° provides maximum damping since the hysteretic bars will undergo an external magnetic field along the length sweeping from $-H_{earth}$ to H_{earth}. As the damping occurs, the angle θ decreases, and the magnetic field component along the length sweeps from $-H_{earth} \cdot sin\theta$ to $H_{earth} \cdot sin\theta$. This behaviour significantly reduces the damping of the PMAS for low rotational energy.

If α is important, the damping will be reasonably efficient until it reaches steady state. That can be seen in Figure 3.5 where $\alpha = 15°$ as predicted by Equation 3.2. Once energy is dissipated, the total magnetic moment of the satellite aligns itself with the Earth's magnetic field. From that time, the satellite precesses around the local magnetic field line. In the body frame of the satellite this corresponds to the main component of the

angular velocity aligned with the magnet axis. Moreover, when stabilization is reached, the components of the Earth's magnetic field described in the body frame of the satellite do not anymore show any reversal, and practically zero damping occurs.

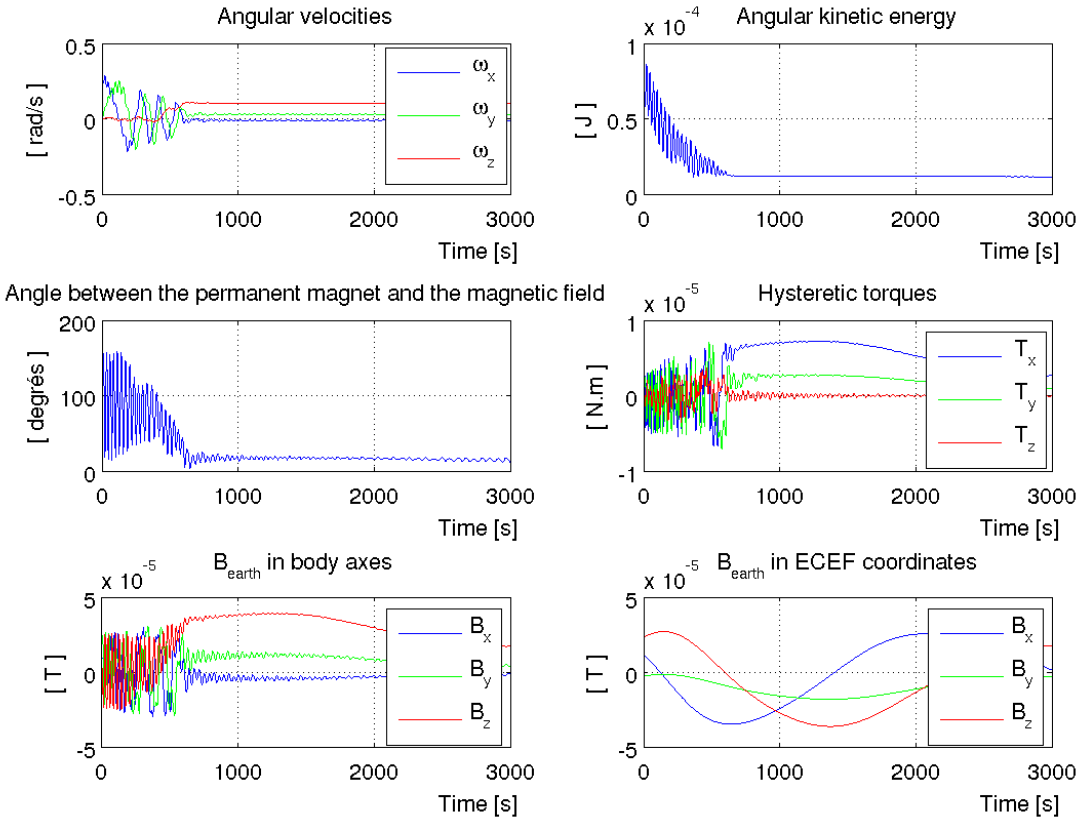

Figure 3.5 – *Simulation of OUFTI-1 attitude with an initial rotation rate of (0,3; 0; 0) rad/s. The possible causes of efficiency reduction are ignored, the AlNiCo magnet's volume is* $0,625cm^3$ *and 2 perpendicular Permenorm 5000 H2 rods of* $0,2cm^3$ *are used.*

If α is small, the damping efficiency will decrease with the angle between magnet and local earth magnetic field, and the oscillations are slowly damped until it gets close to α.

3.4 High rotational velocity hypothesis

A first study of the antennas deployment has shown that a non-negligible rotational velocity could possibly result from it (Reference [13]). The rotational velocity that was feared was of the order of π rad/s. That hypothesis was reinforced by the problems the SwissCube was subjected to after launch on 23^{rd} September, 2009. Although it is counter-physical, the SwissCube team also suspected the antennas deployment to be one potential reason for the observed high rotational velocity.

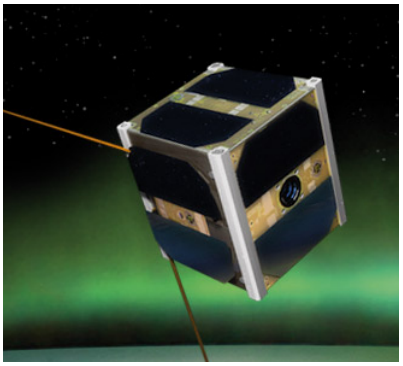

Figure 3.6 – *Representation of the Swisscube nanosatellite with deployed antennas (Reference [15])*

From those observations this threat had to be studied in more details. Some simulations have therefore been performed, and the plausibility of the high initial rotational velocity has been studied in parallel.

3.4.1 Simulation of the attitude control

Ignoring the possible causes of efficiency reduction, four simulations were performed to get an idea of the behaviour of the satellite after antennas deployment. A high torque due to antennas is feared, and a quite big amount of hysteretic materials were therefore used. The drawback is that the resolution gets worse.

Permanent magnet	Hysteretic bars	Stabilization time	Residual rotation	System resolution
AlNiCo-5 $1cm^3$	Hy-Mu-80($2 \times 0.4cm^3$)	$11h$	$5(^o/s)$	26^o
AlNiCo-5 $1cm^3$	Permenorm($2 \times 0.2cm^3$)	$5h$	$16(^o/s)$	31^o
AlNiCo-5 $2cm^3$	Hy-Mu-80($2 \times 0.4cm^3$)	$9h$	$2(^o/s)$	15^o
AlNiCo-5 $2cm^3$	Permenorm($2 \times 0.2cm^3$)	$4h$	$8(^o/s)$	24^o

Table 3.3 – *Simulations of OUFTI-1 attitude with an initial rotation rate of (2; 3,5; 0,75) rad/s. The simplified switch model of the hysteresis is used and the possible causes of efficiency reduction are ignored.*

3.4.2 In depth study of the high initial rotation rate

The antennas deployment system of SwissCube and OUFTI-1 are similar. Figure 3.7 represents the two deployment mechanisms. The antennas are coiled up around a guide, and they are held back with a wire. The melting of the wire at least fifteen minutes after launch releases the antennas to their final configuration.

In order to investigate the transient response of the attitude to the antennas deployment, a finite element model was made by Hoffait S. and Brüls O. (Reference [14]). This study confirms that no high rotational velocity should come from antennas deployment after the transient period (see Figure 3.9). Even though the torque is non-negligible, antennas deployment produces only a transitional torque which has no continuous component. A quite high angular velocity up to about $150^o/s$ during the transient period is slowed down back to the initial rotation rate after the damping of the antennas oscillations. This is

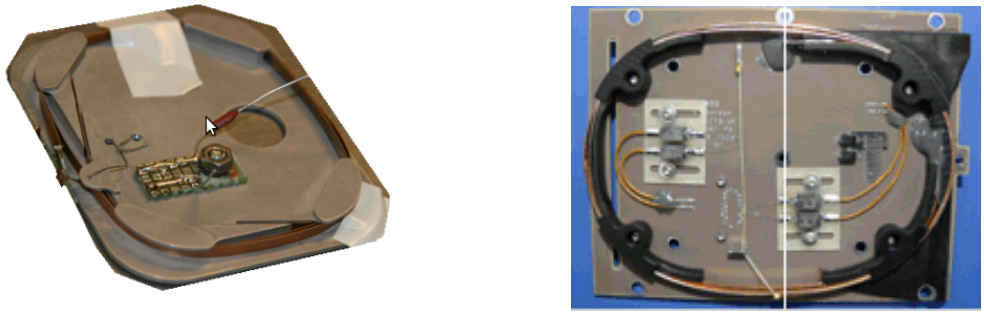

Figure 3.7 – *Prototype of the OUFTI-1 Antennas deployment system on the left (Reference [16]) and the SwissCube deployment mechanism on the right (Reference [15])*

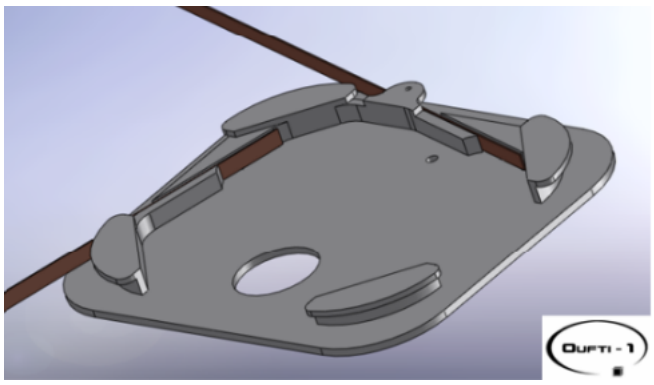

Figure 3.8 – *Preliminary design of the OUFTI-1 deployment mechanism (Reference [17])*

in accordance with what was expected from the conservation of angular momentum of an isolated system.

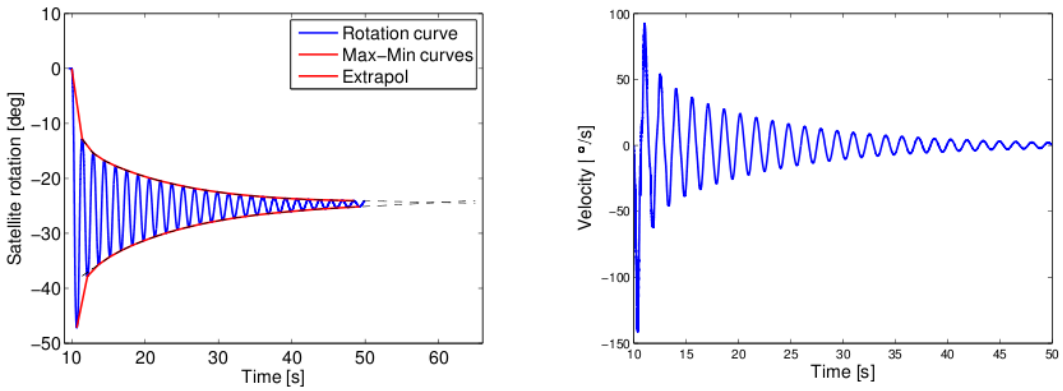

Figure 3.9 – *(a) Satellite rotation and (b) Satellite velocity (Reference [14])*

As it seems that antennas deployment cannot be the direct cause of the high initial rotation rate that SwissCube experienced, other hypotheses have emerged. The collision with another CubeSat could be the cause, but that is not likely according Muriel Noca, the SwissCube project manager. The CubeSats were launched out of the P-POD with an interval of 20 seconds between each of them. Moreover, such a collision would have

damaged the solar cells. Another hypothesis which is investigated by the SwissCube team involves a partial deployment of the antennas inside the P-POD, which would have led to a high angular velocity during the expulsion.

3.5 Influence of the finite elongation of hysteretic rods

The efficiency of a hysteretic rod is not only determined by its volume and the material used. The scheme of the arrangement, the technique of heat treatment and especially the shape of the rod can considerably change its efficiency.

A good modelling of the hysteresis phenomenon is of huge importance in the modelling of passive magnetic attitude control. Vector study is normally required to model the hysteresis phenomenon due to a rotating magnetic field (Reference [18]). Indeed, the magnetic field and magnetization vectors are in that case not parallel because of remanence, and this therefore requires vector study. However to model elongated rods, scalar hysteresis models such as Preisach model and the Jiles-Atherton models can be used, and they have been developed in Reference [2]. Kinetic energy dissipation is then approximated with the magnetic field reduced to only the component in the longitudinal direction of the hysteretic rod.

The elongation of the hysteretic rods plays a crucial role in the efficiency of the PMAS. The parameters given for soft ferromagnets refer to an ideal hysteresis loop obtained in a magnetic circuit without air gaps and after optimum heat treatment (Reference [19]). In that case, the magnetic lines are confined in the material around its perimeter so that all the field lines are closed loops within the material, and the demagnetizing effect is absent. On the other hand, in a rod, there exists a self-generated field that has a direction such as it tends to demagnetize the specimen. This demagnetizing field strongly impacts the hysteresis damping, and it depends mainly on the elongation of the rod.

3.5.1 Hysteresis phenomenon and ferromagnetism

In ferromagnetic materials, two nearby magnetic dipoles tend to align in the same direction because of quantum mechanical effects (due to the electrons' spin and Pauli exclusion principle). These effects reduce the energy of the electrons when their spins are parallel compared to their energy when the spins are anti-parallel, therefore the parallel-spin state is more stable. These quantum mechanical effects imply that every piece of ferromagnetic material has a strong magnetic field. The tendency of magnetic dipoles to align does not occur in classical electromagnetism. Indeed two nearby magnetic dipoles should tend to align in opposite directions which is a state of lower energy. Therefore, ferromagnets spontaneously divide into small magnetic domains and the classical behaviour is then followed at long distances.

Thus, an ordinary ferromagnet material has initially little or no net magnetic moment. However, if it is placed in an external magnetic field, the domains will progressively orient themselves in parallel with the external field, and they will partially remain oriented when the field is turned off. This magnetization as a function of the external field is described by a hysteresis curve.

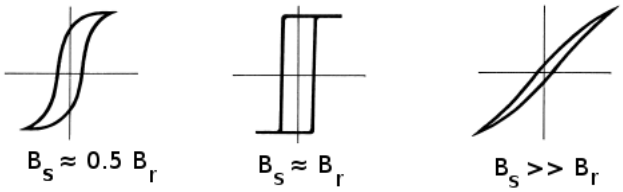

Figure 3.10 – *Different possible hysteresis loop shapes*

3.5.2 The demagnetizing field H_d and the demagnetizing factor N_d

The demagnetizing field explains that the flux density is not uniform and reduced in a rod of hysteretic material. A bar sample magnetized by a field from left to right has a north pole at the right end and a south pole at the left (see Figure 3.11). The H lines radiate from the north pole to the south pole both outside and inside the material. The inside lines tends to demagnetize the material. This effect strongly influences the behaviour of magnetic materials with strong impact on the hysteresis cycle of soft magnetic materials.

The demagnetizing field is also used to shield a volume thanks to soft magnetic materials placed around it. That shield made of high magnetic permeability metal alloys actually reduces the H-field inside the shell thanks to the demagnetizing effect.

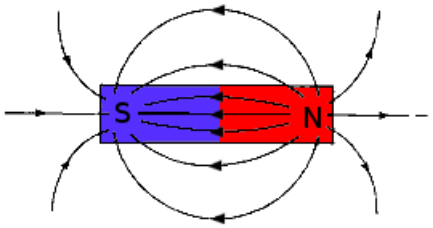

Figure 3.11 – *Demagnetizing field*

The demagnetizing field H_d (sometimes called self-demagnetizing field) acts in the opposite direction of the magnetization M which creates it. The relation

$$B = \mu_0(H_{in} + M) = \mu_0(1 + \chi_m)H_{in} = \mu_0\mu_r H_{in} \tag{3.3}$$

is of course still valid (with χ_m the magnetic susceptibility). However the magnetic field inside the magnet H_{in} is significantly lower than H_{ext} :

$$H_{in} = H_{ext} - H_d$$

The demagnetizing field H_d of a body is proportional to the magnetization which creates it :

$$H_d = N_d M$$

where N_d is the demagnetizing factor. The value of N_d depends mainly on the shape of the body (see for instance Reference [20]). The demagnetizing field will be less if the magnetization is along the long axis than along one of the short axes. Magnetization along

the long axis is thus easier, and the demagnetizing factor N_d tends to zero when magnetized along the length. From the two previous formulas, it follows

$$H_{in} = H_{ext} - N_d M = H_{ext} - N_d \chi_m H_{in}$$

which leads to

$$H_{in} = \frac{H_{ext}}{1 + N_d \chi_m} \tag{3.4}$$

That equation relates the external magnetic field to the magnetic field inside the rod and thus the magnetization. The magnetization reduction due to the demagnetizing effect is thus

$$\frac{1}{1 + N_d \chi_m}$$

That allows to express Equation 3.3 as

$$B_{rod} = \mu_0 \frac{\mu_r}{1 + N_d \chi_m} H_{ext} \tag{3.5}$$

From those equations, it can be seen that the magnetic susceptibility χ_m and the demagnetizing factor N_d plays a crucial role. Even though the magnetization is along the long axis ($N_d \approx 0$), the magnetization reduction can be important if the magnetic susceptibility prevails. That will be studied further in Section 3.5.3.

Figure 3.12 – *Demagnetizing factor*

3.5.3 Efficiency reduction due to finite elongation

The shape of the rod can considerably change its efficiency. As explained in the previous section, the demagnetizing field effect depends on the rod's shape. As an example, the volume of the rods on-board the Transit-2 satellite was four times less than that on the Transit-1 satellite, while the efficiency per unit volume was larger by a factor of five (Reference [21]). The main reason was the elongation twice larger for the Transit-2 rods.

From Equation 3.5, the magnetic flux intensity within the rod B_{rod} is given by

$$B_{rod} = \mu_0 \mu'_r H_{ext}$$

in which H is the magnetic field parallel to the rod. The apparent permeability μ'_r depends on the rod material's true permeability μ_r and the demagnetizing factor N_d. It can be expressed in a good approximation when $\chi_m >> 1$ as

$$\mu'_r = \frac{\mu_r(H)}{1 + N_d \mu_r(H)}$$

where μ_r is the relative permeability which depends on the rod material and the magnetization history, while N_d is the demagnetizing factor which mainly depends on the rod elongation e.

The relation between N_d and e is first evaluated using approximate analytical solutions. The simplest expression of N for a rectangular rod with square cross section (Reference [22]) is

$$N_d = \frac{1}{1+2e}$$

with the elongation $e = \frac{length}{thickness}$. For long cylinders the approximate formula is

$$N_d = \frac{1}{e^2} ln(2e - 3/2)$$

The typical values for the apparent permeability are shown in Figures 3.13 and 3.14.

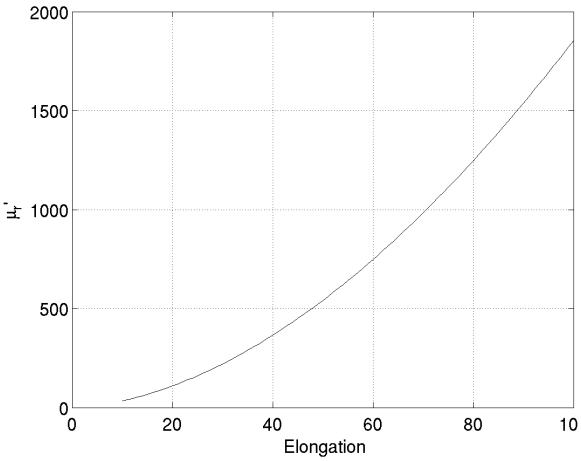

Figure 3.13 – *Apparent permeability as a function of elongation for a circular cross section*

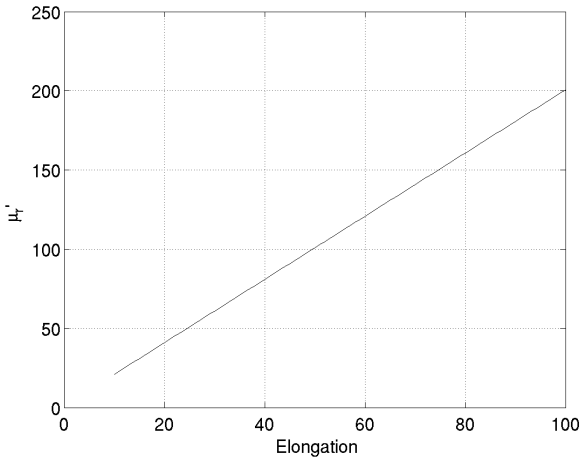

Figure 3.14 – *Apparent permeability as a function of elongation for a square cross section*

Equation 3.4 gives the relation between H_{ext} and H_{in}, and it can be expressed as

$$H_{in} = \frac{H_{ext}}{1 + N_d \chi_m} = \frac{\mu_r'}{\mu_r} H_{ext} \tag{3.6}$$

Analytical solutions will be used for simplicity, but the effect of the demagnetizing field can be calculated using finite element methods, which are presented in Appendix A.3. Illustrations can be seen in Figure 3.15 and 3.16 for a circular cross section and an elongation of 80. The apparent permeability found with finite element methods are similar to the analytical solutions.

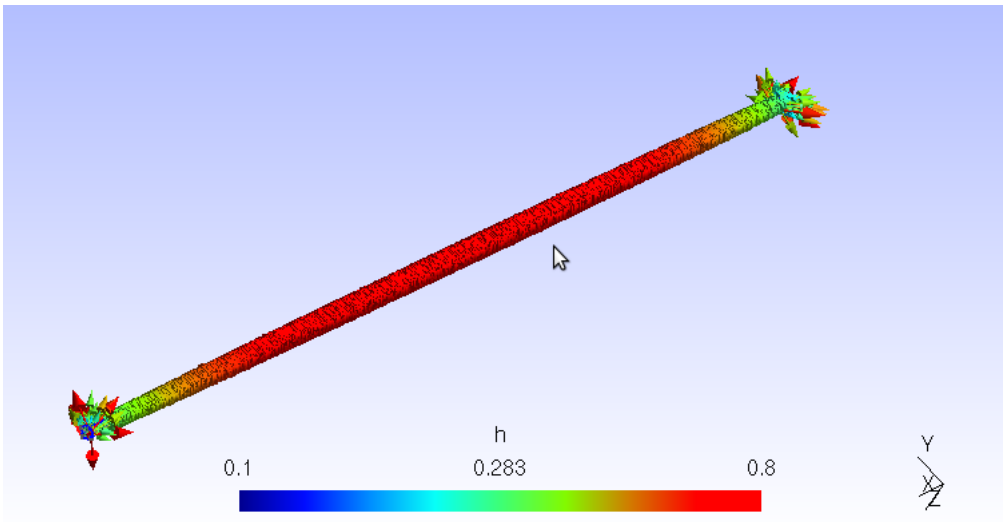

Figure 3.15 – *H-field inside a circular cross section rod with* $\mu_r = 10^5$ *and an external H-field along the rod of 30 A/m*

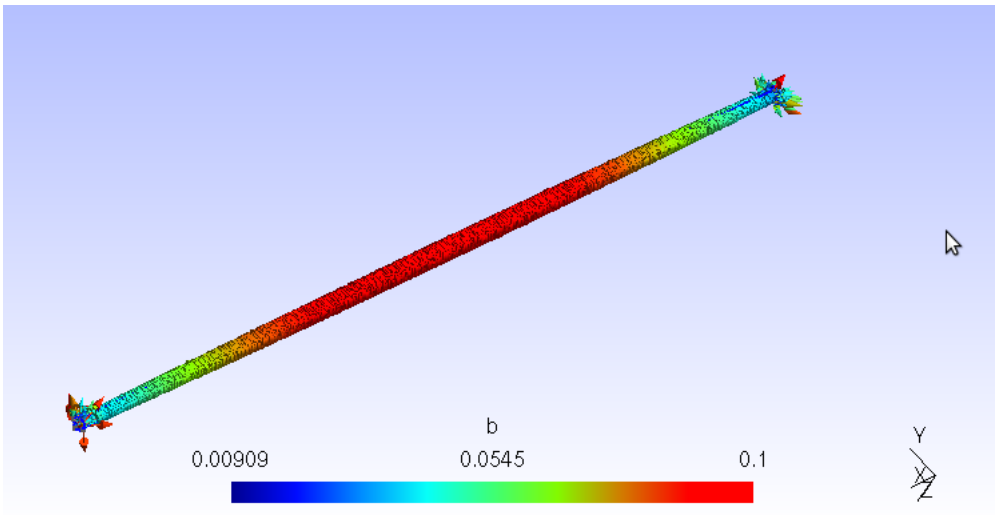

Figure 3.16 – *B-field inside a circular cross section rod with* $\mu_r = 10^5$ *and an external H-field along the rod of 30 A/m*

As can be seen in Figures 3.17 to 3.19, the damping efficiency is approximately proportional to the square of μ'_r. Indeed, H_{in} is proportional to it as stated by Equation 3.6, and B is proportional to H_{in} from Equation 3.3.

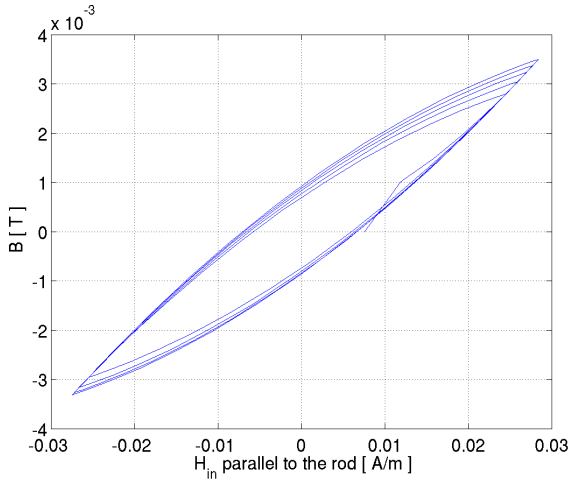

Figure 3.17 – *Illustration of the hysteresis cycle for a circular cross section*
$e = 18$, $\mu_r = 10^5$, $\mu'_r = 100$
The energy dissipation per cycle with $H_{ext} \in [-30; 30] A/m$ *is* $1 \cdot 10^{-5} J/cycle/m^3$.

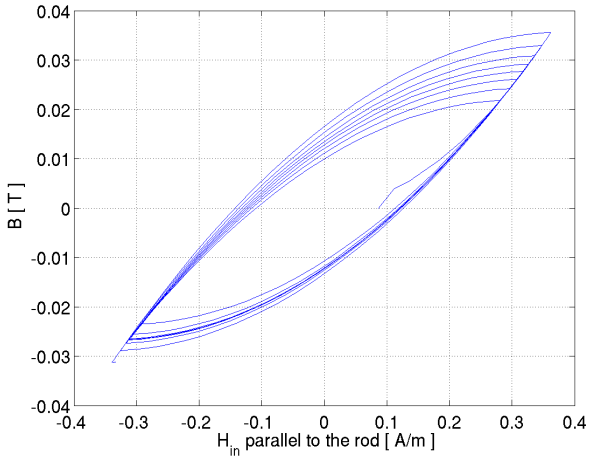

Figure 3.18 – *Illustration of the hysteresis cycle for a circular cross section*
$e = 80$, $\mu_r = 10^5$, $\mu'_r = 1200$
The energy dissipation per cycle with $H_{ext} \in [-30; 30] A/m$ *is* $4 \cdot 10^{-3} J/cycle/m^3$

With materials of identical composition, the shape of the hysteresis loop and the magnetic properties can be altered over a wide range depending on the material properties (composition, heat treatment, ...). Imperfections or incomplete heat treatment in the material provide obstacles to domain wall movement, and they can strongly change the hysteresis loop parameters. Moreover, the rod shape contributes largely to the hysteresis parameters. Accurate predictions cannot be performed for theses reasons (Reference [23]). A procedure to evaluate these parameters should therefore ideally be set up to evaluate the final hysteretic rod magnetic properties.

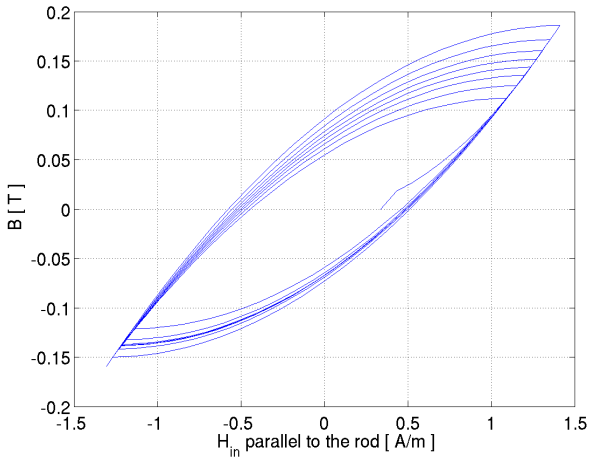

Figure 3.19 – *Illustration of the hysteresis cycle for a circular cross section* $e = 160$, $\mu_r = 10^5$, $\mu'_r = 4000$
The energy dissipation per cycle with $H_{ext} \in [-30; 30] A/m$ *is* $9 \cdot 10^{-2} J/cycle/m^3$

3.6 Influence of the magnet on the hysteretic bars

A first approximation

The B-field can be approximated in the surrounding of the magnet by considering the magnet as a magnetic dipole. That approximation is exact at distances r orders of magnitude larger than the dimensions of the magnet. A reference frame in which the magnet center is at the origin, and the z-axis is pointing in the direction of the magnetic moment $\boldsymbol{\mu}$ is chosen. In this frame, the far magnetic field produced by the system, at any point (x,y,z) in space, is given by (in teslas):

$$B_x(x,y,z) = \frac{\mu_0}{4\pi} 3\mu \frac{xz}{(x^2+y^2+z^2)^{5/2}}$$

$$B_y(x,y,z) = \frac{\mu_0}{4\pi} 3\mu \frac{yz}{(x^2+y^2+z^2)^{5/2}}$$

$$B_z(x,y,z) = \frac{\mu_0}{4\pi} 3\mu \frac{z^2 - \frac{1}{3}(x^2+y^2+z^2)}{(x^2+y^2+z^2)^{5/2}}$$

In the plane $z = 0$, the magnetic field lines are perpendicular to the hysteretic rods. $B(r) = B_z(r)$ is given by

$$\frac{\mu_0}{4\pi}\frac{\mu}{r^3}$$

The results are shown in Figure 3.20.

That is only a first approximation since the dimensions of the magnet are not orders of magnitude smaller than the distance of interest r.

Physical interpretation

The magnetic domains align themselves with the external field. If an alternating magnetic field is applied to the material, its magnetization will trace out a hysteresis loop. It takes some energy to counter the residual alignment and change the orientation of the

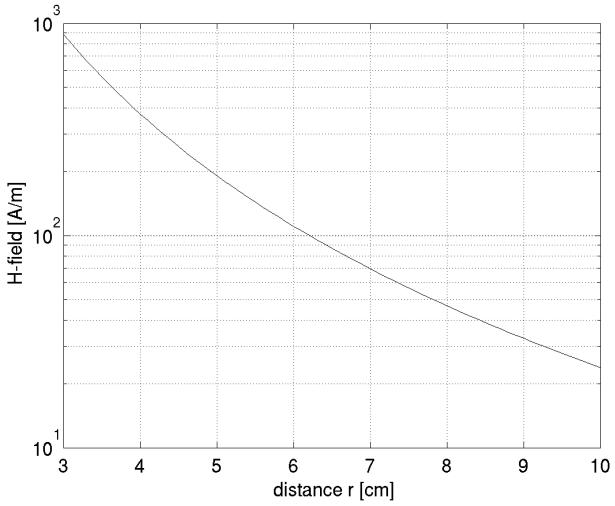

Figure 3.20 – *Magnetic dipole approximation of the H-field for* $\mu = 0.3A/m^2$ *and different distances* r

magnetic domains. The variation of the magnetic field as seen from the hysteretic materials should lead to the cover of the hysteresis loop while the satellite rotates and thus it should produce damping.

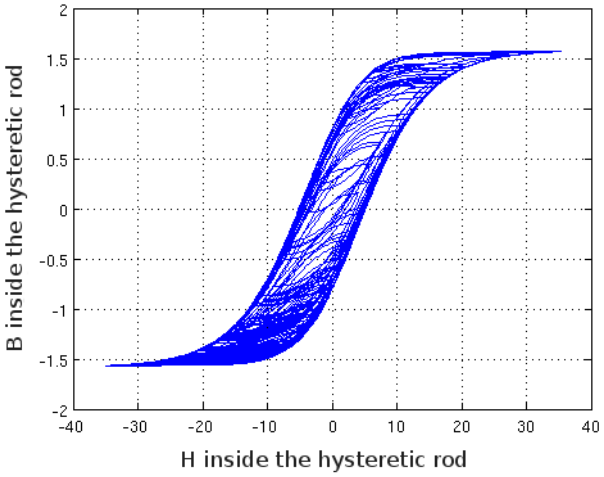

Figure 3.21 – *0-D model of the hysteresis cycle (Preisach model of hysteresis)*

The magnetic field is in this case the superposition of the field due to the magnet and due to earth. The field due to the magnet is unchanged in the body frame of the satellite. If the magnet's field is too important, the local earth magnetic field only causes a small variation to the dominant field produced by the magnet. Therefore the magnetization of the magnetic domains only changes slightly from the direction of the magnet's field. The slight reorientation of the magnetic domains takes less energy compared to a complete reorientation, and it provides significantly less damping. This can be seen as an incomplete cover of the hysteresis loop.

That effect is shown to be one of the causes of a reduced efficiency of the nanosatellite Delfi-C3 in Section 3.7.

3.7 Delfi-C3's case

Delfi-C3 is a nanosatellite of $30 \times 10 \times 10cm^3$ and $2,2kg$ ($I_x = I_y = 0,035$, $I_z = 0,01505$) developed at the Delft university of technology and launched in April 2008. The stabilisation system was composed of two magnetic hysteretic rods and one permanent magnet.

The expected rotational rate was from a maximum of $10^o/s$ to between $0,2-2^o/s$ within one orbit after ejection from X-POD. The behaviour in orbit showed an anomalous slow damping. It took about two months to slow down from $6^o/s$ to less than $2^o/s$.

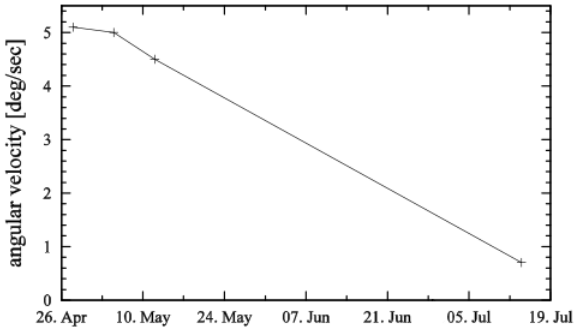

Figure 3.22 – *Delfi-C3 : In orbit results of the attitude behaviour (Reference [11])*

The design of the passive magnetic attitude stabilisation system can be seen in Figure 3.23.

- The Permenorm 5000 H2 hysteretic rods are $70mm$ long, with a diameter of $4mm$ and a volume of $769mm^3$.
- The volume of the AlNiCo magnet is $298mm^3$ and has a shape alike a parallelepiped with dimensions $2,5mm \cdot 4,8mm \cdot 25mm$. Its dipole moment is $0,30Am^2$.

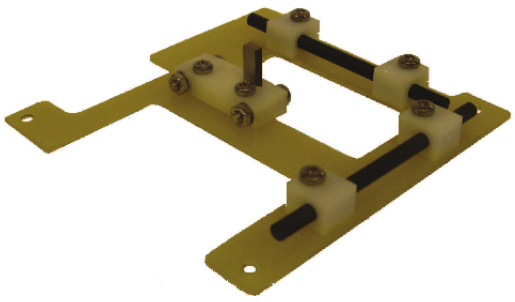

Figure 3.23 – *The rod-board as produced (Reference [11])*

The finite elongation of the rods (Section 3.5) and the influence of the magnet (Section 3.6) are the likely causes of the "anomalous" slow damping of Delfi-C3. The two effects will be studied in this particular case.

3.7.1 Finite elongation of the rods

As explained in Section 3.5, the finite elongation of the rods leads to a demagnetizing field and to a partial cover of the hysteresis loop. For an elongation of the rod of 18 as seen in Figure 3.17, the energy dissipation per cycle and per unit volume is about $1 \cdot 10^{-5} J/cycle/m^3$. The total volume of the rods is $1,5 \cdot 10^{-6} m^3$ which leads to an energy dissipation per cycle of $1,5 \cdot 10^{-11} J/cycle/$. Taking I as $0,02 kg.m^2$ and assuming that this cycle is covered at every rotation, Equation 3.1 can be used to get an estimation of the damping efficiency. The decrease rate is $10^{-10} rad/sec^2$ which suggests a time of several years to slow down by 0,1 radian/s.

That pessimistic estimation has to be moderated. Better performance can in fact have different main contributions. The fact that the two rods are close lead to a mutual influence, which has a similar effect as a higher elongation. An elongation multiplied by two would be equivalent to an improved performance by a factor of ten. The heat treatment can also have a significant impact on the magnetic properties of the rods. For small elongations as it is the case in the Delfi-C3, a decrease of the ideal magnetic permeability has a positive impact on the damping efficiency. Indeed, a decrease of the magnetic permeability reduces the demagnetizing field, and it increases the H-field inside the rods while keeping the B-field in a similar range. That effect can be seen in Figure 3.24. Another likely cause is the presence of other ferromagnetic materials inside the CubeSat.

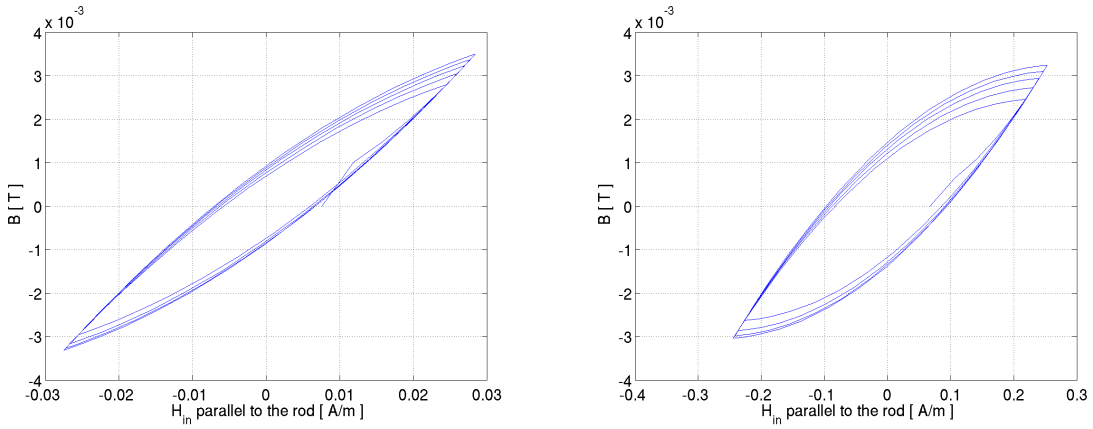

Figure 3.24 – *Illustration of the hysteresis cycle for a circular cross section with* $H_{ext} \in [-30; 30] A/m$ *and e=18*
On the left $\mu_r = 10^5$*, on the right* $\mu_r = 10^4$

3.7.2 System resolution

Delphi-C3 was designed to damp rotational rate but not to align well on the local magnetic field. However, if the finite elongation of the rods is taken into account, the satellite still aligns with the earth magnetic field. Let's first ignore the demagnetizing effect due to the finite elongation of the rods; the predicted behaviour is then explained in an article on the Delfi-C3 attitude (Reference [24]) :

> "The volume of the permanent magnet is $2.977 \cdot 10^{-7} m^3$, the volume of the hysteretic material is $7.69 \cdot 10 - 7m^3$ on each perpendicular axis. (...) The satellite is supposed to align not so well to the magnetic field lines. This is desired by the system design because the two experimental payloads of Delfi-C3, a sun sensor and thin film solar cells, should be lighted from different angles. Therefore the attitude control system is supposed to not align well with the magnetic field lines but mainly to dampen excessive rotational rates."

If the finite elongation of the rod is not taken into account, the residual magnetic moment of the hysteretic rods is higher than the magnetic moment of the small magnet, which leads to no longer perfectly alignment to the magnetic field lines. The magnetic moment of the magnet is $0.3A.m^2$, and the remaining magnetic moment of each rod can be estimated as $\frac{B_r}{\mu_0} V = 0.46A.m^2$. The deviation that is found is then approximated by

$$\alpha = \arccos\left(\frac{\left|\vec{\mu_{magnet}}\right|}{\left|\vec{\mu_{tot}}\right|}\right) \approx 70°$$

Assuming no demagnetizing field effect for the simulation, the behaviour predicted by our simulator confirms this in Figure 3.25, and the satellite aligns almost perpendicularly to the magnet as predicted. Their simulations achieved similar results.

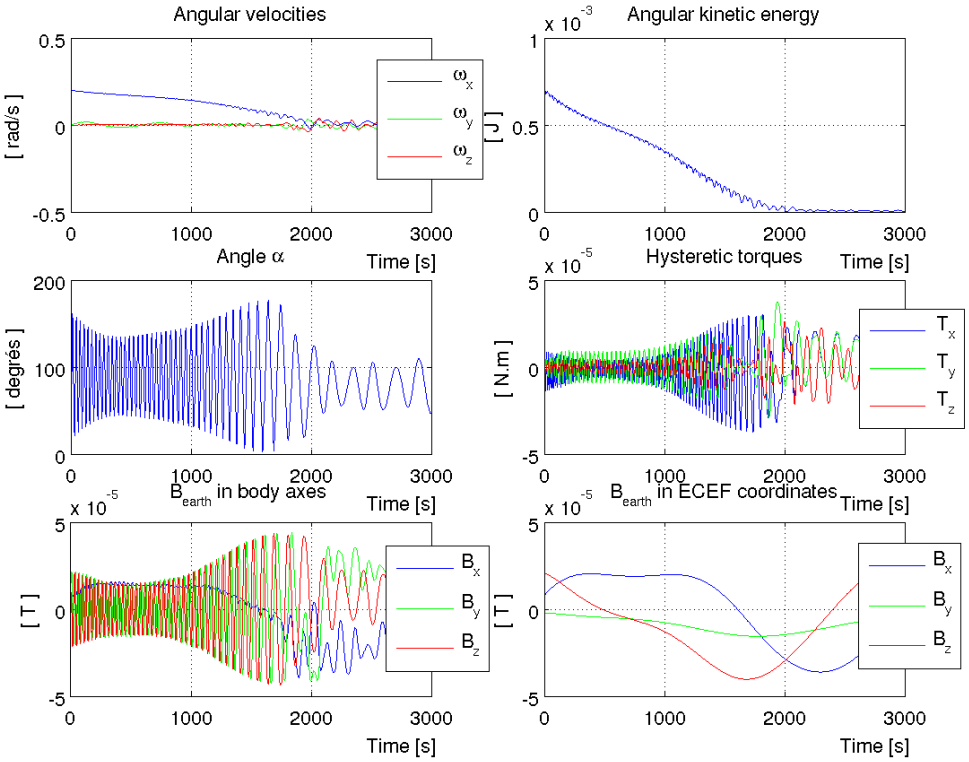

Figure 3.25 – *Simulations of the Delfi-C3 attitude ignoring finite elongation of the rods and interaction between the magnet and the hysteretic rods*

However, this behaviour is not likely to happen in orbit because the hysteresis cycle is not covered completely, and the remanent induction B_r is therefore smaller. For this

reason, the satellite therefore aligns much better on the local earth magnetic field.

3.7.3 Efficiency reduction due to the interaction between the magnet and the hysteretic rods

Finite element methods will be used to get a deeper understanding of the efficiency reduction of the Delfi-C3 PMAS due to the interaction between the magnet and the hysteretic rods.

As can be seen in Figures 3.26 and 3.27, the hysteretic rods undergo an external H-field which is perpendicular to their length. The rod along y axis undergoes a H-field which goes from $45A/m$ at the extremities to $80A/m$ at the centre. It is even more important for the rod along x-axis where it goes from 80 to 500 A/m. Those results are in agreement with the first approximation presented in Section 3.6.

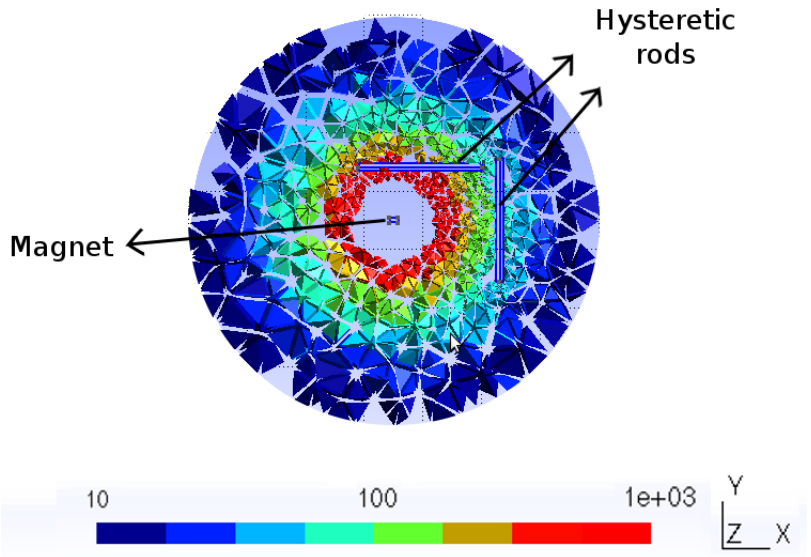

Figure 3.26 – *H-field norm [A/m] representation in the plane of interest*

The apparent permeability μ'_r tends to unity value when the rod is magnetized perpendicular to its length, and it tends to $\mu'_r = 100$ when magnetized through the length (see Section 3.5). That effect is due to the demagnetizing field which is less important along the long axis. Figure 3.28 illustrates this for the perpendicular magnetization of the rod while magnetization illustrations along the length are displayed in Figures 3.29 and 3.30. Without the demagnetizing effect, the rods would be totally saturated due to the magnet and would provide a very reduced damping. The demagnetizing effect has from this point of view a beneficial effect.

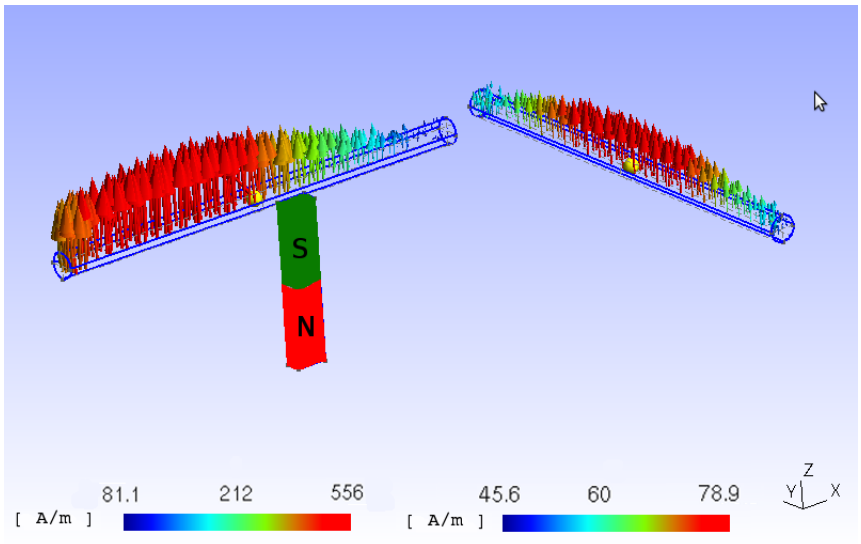

Figure 3.27 – *External H-field in the hysteretic material location. The demagnetizing effect is here not taken into account.*

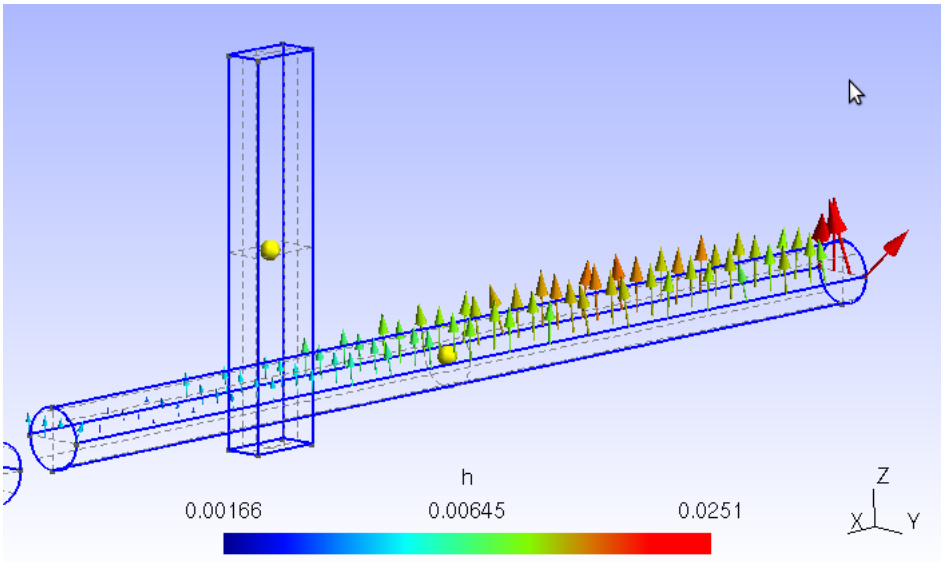

Figure 3.28 – *H-field due to the magnet inside the rod along x-axis when demagnetizing field is superimposed to the external one* ($\mu_r' \approx 1$)

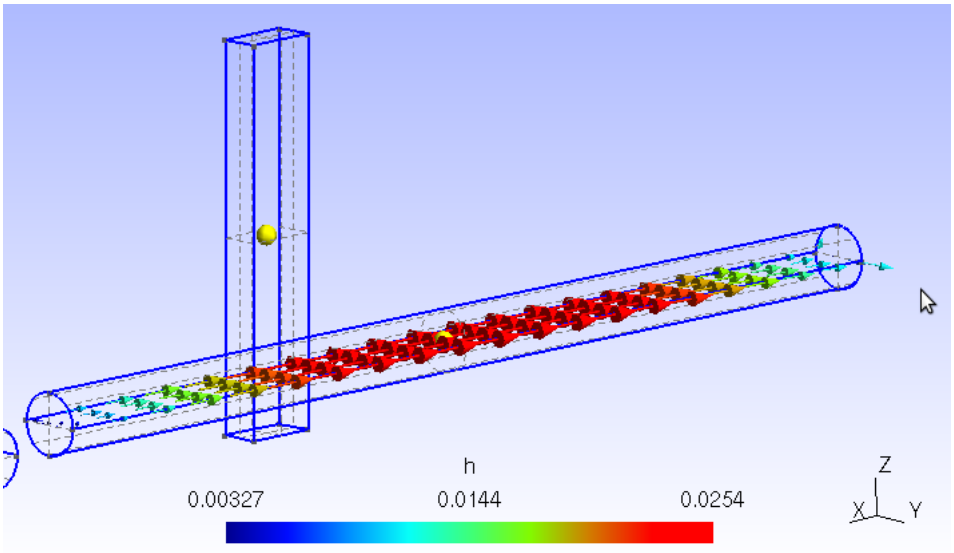

Figure 3.29 – *H-field inside the rod along x-axis due to an external H-field of* $15A/m$ *parallel to the rod* ($\mu_r' \approx 100$)

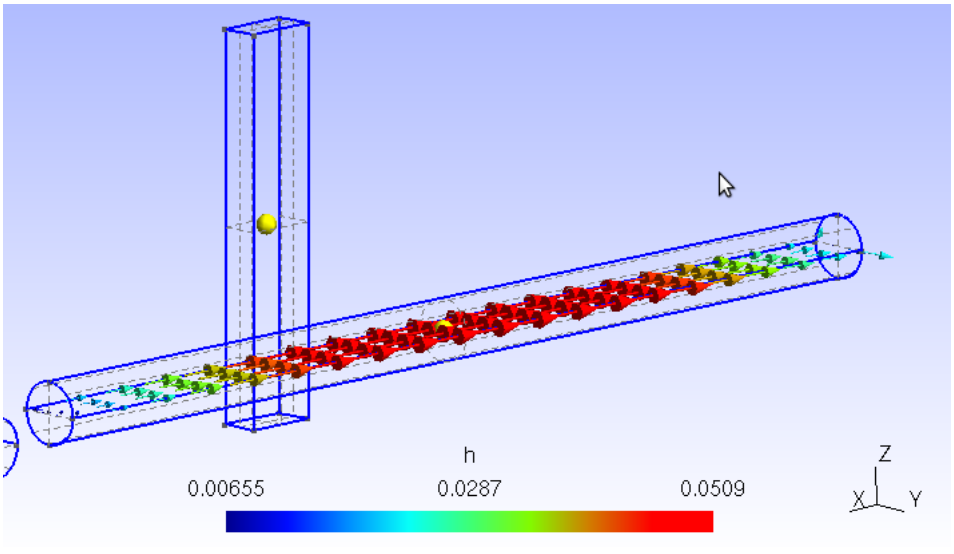

Figure 3.30 – *H-field inside the rod along x-axis due to an external H-field of* $30A/m$ *parallel to the rod* ($\mu_r' \approx 100$)

The earth magnetic field is significantly less than the H-field due to the magnet. An efficiency reduction therefore occurs in the case of Delfi-C3 even though the magnetization along the long axis is much easier. The earth magnetic field H_{earth} is typically of $30 A/m$ on the Delfi-C3 orbit. On the one hand, the efficiency of the hysteretic rod along y-axis is not reduced much because the magnet's field is of the same order of magnitude, and this allows effective magnetization along the length. On the other hand, the external H-field due to the magnet goes, in the rod along x-axis, from 80 to 500 A/m which is much more important than the earth field. In the presence of that important external field perpendicular to the length, the magnetic field *inside the magnet* has two contributions of comparable strength. The contribution of the magnet keeps the same direction, sense and intensity in the rods as seen from the body axes. As the earth magnetic field rotates in the body axes, the magnetization of the magnetic domains only changes slightly around the direction of the magnet's field. The slight reorientation of the magnetic domains takes less energy compared to a complete reorientation, and it provides less damping.

Figures 3.31 and 3.32 illustrate this effect. In the first illustration, the H-field of earth is supposed to have a component towards +x axis of 15 A/m, and it is then reversed to point along -x axis in the second illustration. This situation is supposed to imply a total reversal of the magnetic domains, but only a smaller reorientation occurs due to the magnet's field.

Vector hysteresis models are normally required to quantify the damping reduction due to the magnet's field. It is here assumed for simplicity a constant relative magnetic permeability $\mu_r = 10^5$ in the hysteretic rods. From Figures 3.29 and 3.30, it can be noted that the involved phenomena are then purely linear with the external H-field. By contrast, the actual hysteresis phenomenon comes from a non-linear function between the permeability μ and the magnetization. It can therefore not be modelled perfectly by using only Maxwell equations and finite element methods, but it requires vector hysteresis study to model the hysteresis phenomenon in three dimensions. Vector hysteresis models would not add significant informations and they are out of the scope of this study.

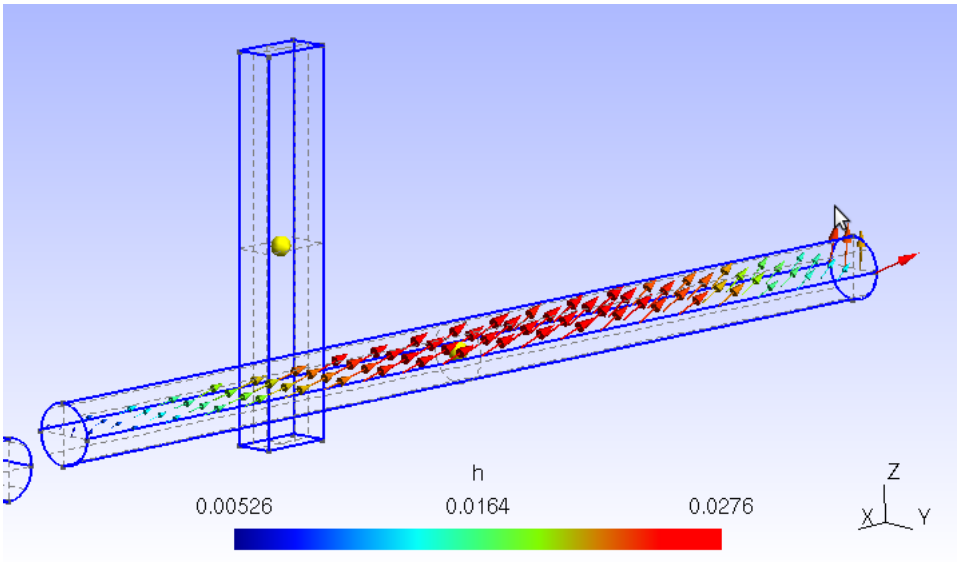

Figure 3.31 – *H-field inside the rod due to the magnet and an external H-field of* $15 A/m$ *parallel to the rod*

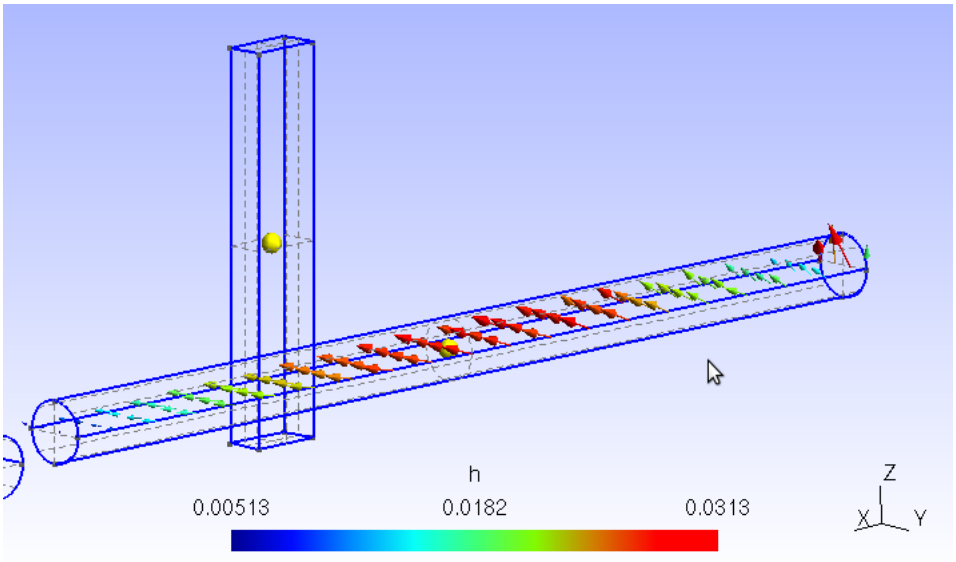

Figure 3.32 – *H-field inside the rod due to the magnet and an external H-field of* $-15A/m$ *parallel to the rod*

3.7.4 Conclusion

The rotational rate was expected to slow down to less than $1^o/s$ in one orbit (less than $2h$) [11] and [24]. Two effects were however not taken into account :

- the finite elongation of the rods (Section 3.5)
- the influence of the magnet (Section 3.6)

The elongation of 18 reduces drastically the rod efficiency, and if the magnet's field is taken into account one of the hysteretic rod provides an even more reduced damping .

3.8 OUFTI-1's case

OUFTI-1's Passive Magnetic Attitude Stabilisation

The first critical point which draws our attention is the magnet's interaction with the hysteretic bars. It limits the magnetic moment of the magnet, and it forces a design whith sufficient distances between the magnet and the hysteretic materials. It is particularly tricky in nanosatellites where the distance between the magnet and the hysteretic materials is limited. Moreover, if a component of the magnet's field is directed along the rod, there is a displacement of the working point in the hysteresis cycle. For that reason, the rods should ideally be as close as possible of the plane that is perpendicular to the magnet axis and passes through its center. Any displacement from this plane leads to a component of the vector field H_{magnet} directed along the rod, which may therefore affect the damping efficiency. This suggests that the rods should ideally be placed as depicted in Figure 3.33. Those two criterions are ensured to be of negligible impact if H_{magnet} in the rods is less than 30A/m, which is a typical value of the earth magnetic field on OUFTI-1's orbit.

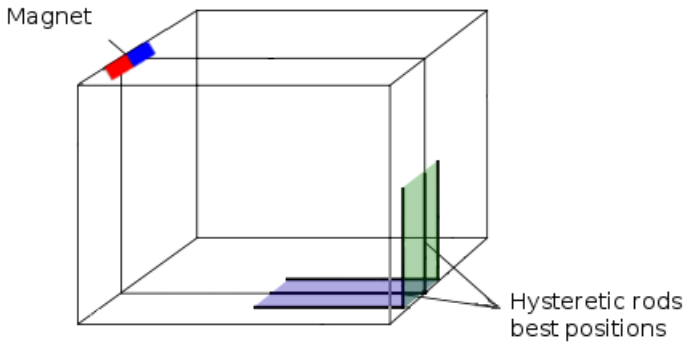

Figure 3.33 – *Ideal positionning of the hysteretic rods*

The criterions for the positioning of the magnet and of the hysteretic bars are summarized here :

- The hysteretic bars are placed orthogonal to the magnet to damp excess angular velocities.
- The magnet's field does not exceed $30 A/m$ which is a typical value of the earth magnetic field on OUFTI-1's orbit.
- The hysteretic bars are close to perpendicularity compared to the magnet's field.

First design

The magnet was first placed next to the batteries close to the center of the -X side of OUFTI-1. The hysteretic bars were placed as far as possible in agreement with the subsystem structure. That arrangement has shown an important influence of the magnet on the hysteretic bars which was likely to reduce the damping efficiency. Figure 3.35 shows the H-field due to the magnet in the vicinity of the hysteretic materials. A new design was therefore advisable.

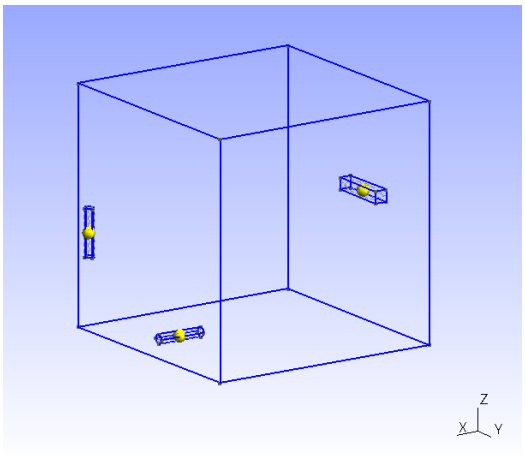

Figure 3.34 – *First design of OUFTI-1 PMAS*

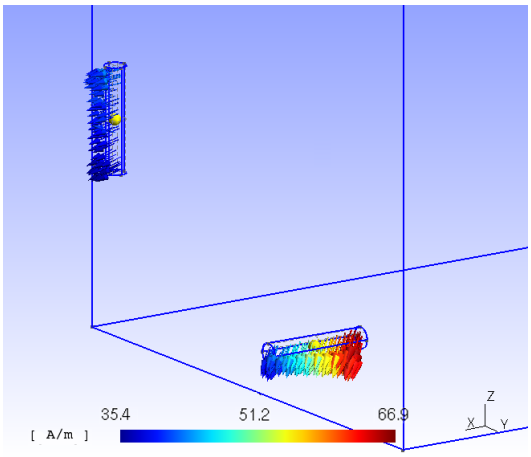

Figure 3.35 – *H-field in the hysteretic bars (AlNiCo magnet of* $5 \times 5 \times 25mm$*)*

Second design

The shift of the magnet has been solicited to the subsystem structure, and another arrangement was found. The magnet will be placed on top of the -X and +Z face. That new arrangement ensures the lowest possible influence of the magnet on the hysteretic bars.

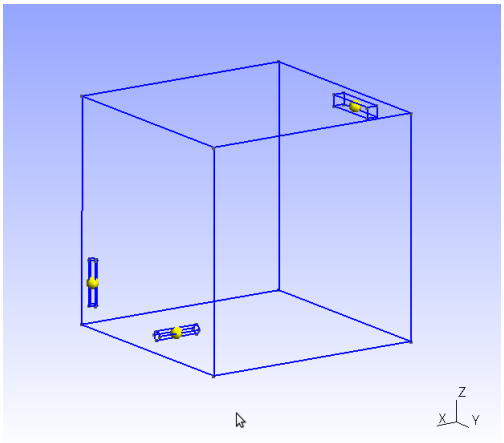

Figure 3.36 – *Second design of OUFTI-1 PMAS*

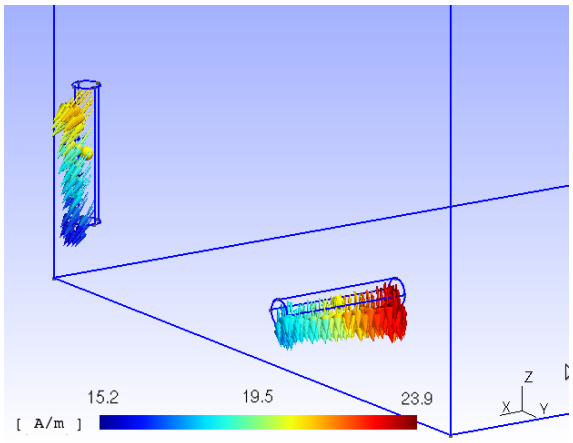

Figure 3.37 – *H-field in the hysteretic bars (AlNiCo magnet of* $5 \times 5 \times 25mm$*)*

Third design

The critical point of the elongation of the rods had not been studied yet, and it appeared that it was crucial to have a high elongation. In order to satisfy this necessity, a new design had to be made. This new design considers the possibility of using two parallel bars in each direction perpendicular to the magnet for a total of four bars. This improves the overall system efficiency and will be discussed further in Section 3.9.2 dedicated to the sizing of the hysteretic materials.

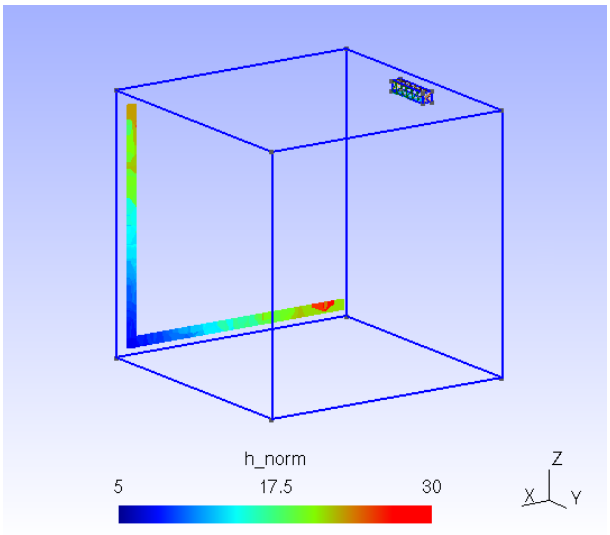

Figure 3.38 – *Third design of OUFTI-1's PMAS (AlNiCo magnet of* $4 \times 4 \times 20mm$*)*

3.9 Practical design of a PMAS for OUFTI-1

This section discusses the final design of the PMAS. The exact sizes, the types of materials as well as the positions are given. The required materials have been ordered and they are described here.

3.9.1 The magnet

The magnetization axis of the permanent magnet must be placed with its magnetic axis parallel to the antennas' plane to encounter the requirements of COM. The exact location is at the center of the edge between face -X and +Z.

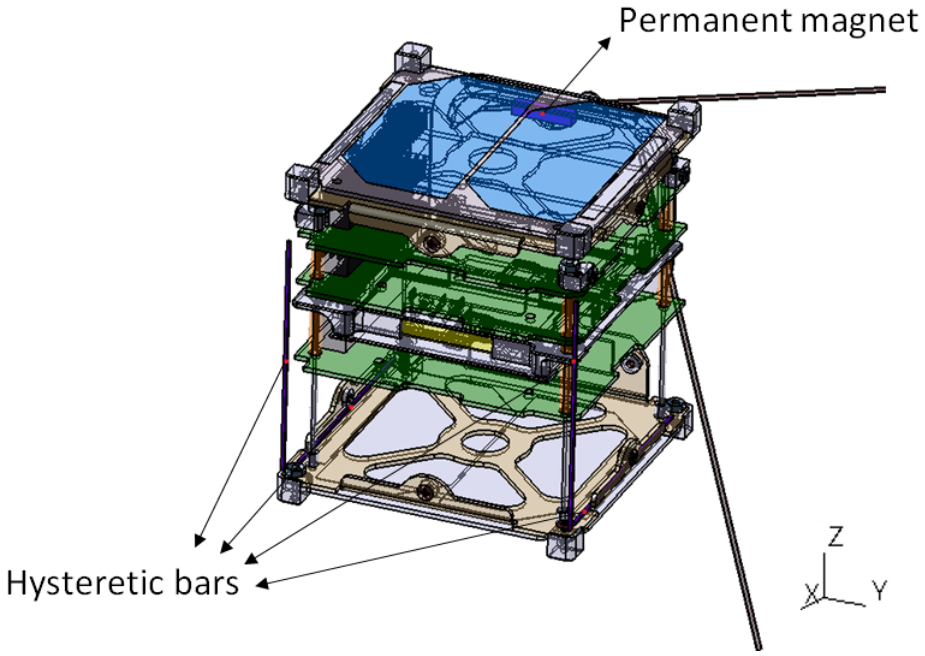

Figure 3.39 – *PMAS configuration (Reference [25])*

The ideal geometry of the magnet is a rectangular parallelepiped to facilitate the integration in the nanosatellite. The commercially available dimensions in AlNiCo-5 parallelepiped are rather restrictive. Two custom-built AlNiCo-5 magnets $4 \times 4 \times 20mm$ with magnetization along the length have been ordered at EUROMAG. The magnets were delivered at the end of May 2010. The main properties of the furnished material is summarized in Table 3.4. Their magnetic moment μ is 0,32 $A.m^2$ and they require no further processing.

	Remanence B_r $[T\ (G)]$	Coercive force H_c $[kA/m\ (Oe)]$	Maximum specific energy $(BH)_{max.}$ $[KJ/m^3\ (MGOe)]$	Density $\rho[g/cm^3]$
Typical	1.26 (12600)	50 (630)	42 (5.30)	7,3
Min.	1.23 (12300)	48 (600)	38 (4.80)	

Table 3.4 – *AlNiCo-5 magnet properties given by the producer*

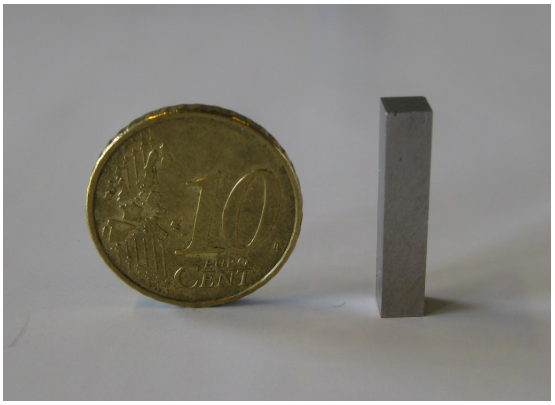

Figure 3.40 – *Picture of one of the magnets delivered by EUROMAG*

3.9.2 Hysteretic materials

The quantity of material required for OUFTI-1's PMAS is not enough to start dedicated production. The German company VACUUMSCHMELZE GmbH & Co. proposed to offer us sample rods with 4 mm diameter of Permenorm 5000 H2. This offer has been accepted, and two samples of 25 cm in length have been received in April 2010. The shaping and heat treatment have still to be performed. The bars will be glued on the chassis of the main structure.

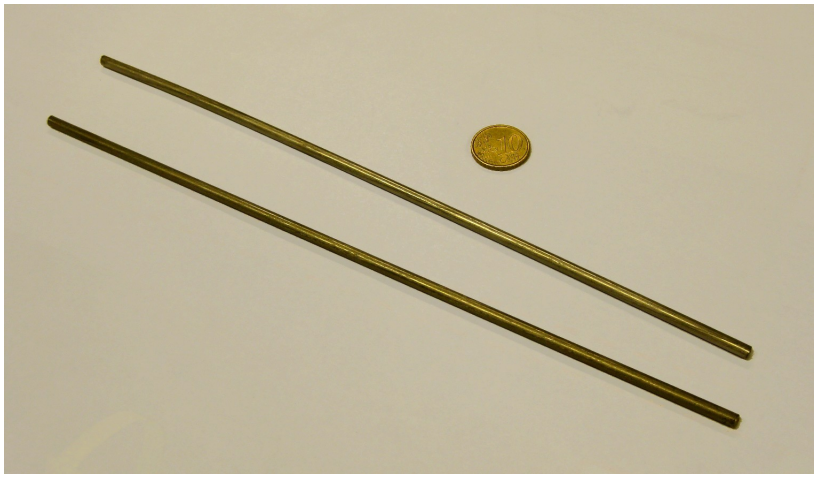

Figure 3.41 – *Picture of the Permenorm 5000 H2 rods received from VACUUMSCHMELZE GmbH & Co*

A trade-off between elongation, volume and practical considerations has to be found for the hysteretic bars in order to optimize the damping efficiency. On the one hand, the rod length is very limited in a nanosatellite, so that an improvement of the efficiency can mainly come from a reduction of the rod cross section. On the other hand, the energy dissipation per cycle is proportional to the volume. Given that the maximum length is about 8 cm, the magnetic dipole efficiency depends on two contributions to the diameter d of the rod's circular cross section.

- The efficiency is proportional to the volume and therefore to d^2.
- The efficiency is proportional to the square of the apparent permeability, and it

therefore increases faster than $1/d^2$ for elongations typically smaller than 200 as seen in Figure 3.42.

Summing up these two effects leads to an efficiency which actually slightly increases with a reduction of the cross section area for the same length. The rod thickness is a compromise between the rod efficiency, the weight, the rod structural robustness and the manufacturing process.

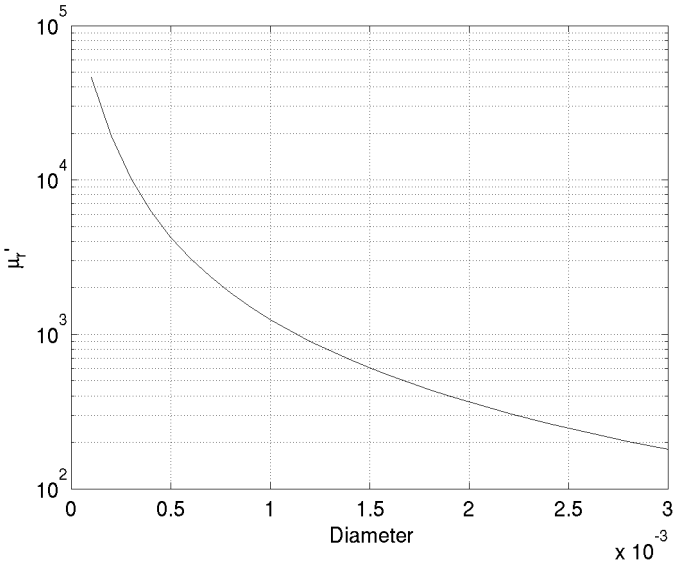

Figure 3.42 – *Apparent permeability as a function of diameter for a* $80mm$ *long rod with a circular cross section*

Since the length of the rods are limited, many parallel bars can be used. This maintains a good rod efficiency while increasing the volume. The parallel rods shouldn't be too close in order to avoid bar mutual demagnetization. If the distance between bars is more than about one third of the length, bar mutual demagnetization can be neglected (Reference [23]). In the OUFTI-1's case, a total of 4 bars can be used as shown in Figure 3.39.

A diameter of 1 mm lead to an elongation of 80 and an energy loss per cycle and per unit volume of $4 \cdot 10^{-3} J/cycle/m^3$. If four bars are used, the total volume is $2,5 \cdot 10^{-7} m^3$. The energy loss per cycle is then approximated by $10^{-9} J/cycle$. Taking I as $0,002 kg.m^2$ and assuming that this cycle is covered at every rotation, Equation 3.1 can be used to get an estimation of the damping efficiency. We get a decrease rate of $8 \cdot 10^{-8} rad/sec^2$ which suggests a time of about 15 days to slow down by 0,1 radian/s. For the same reasons as explained for Delfi-C3's case (Section 3.7), the damping may be even more efficient. To get an accurate estimation, measurements of the hysteresis cycle after shaping and heat treatment should be performed.

3.9.3 Final heat treatment

The necessary information to perform heat treatment is available in Reference [26]. After machining, the rods must be cleaned thoroughly to remove impurities. The magnetic

materials must then be subjected to a final heat treatment to set the optimum magnetic properties. The duration, temperature and, in many cases, the cooling conditions must be strictly respected. Figure 3.43 illustrates the effect of final heat treatment on the magnetic properties using MUMETALL as an example. The required heat treatment consists of 5 hours at 1150 degrees in a H_2 atmosphere to prevent oxidation. A protecting bag made of metal foil can also be used to prevent oxidation. The metal of the bag oxidizes then faster than the rod material, and it thus protects the rod.

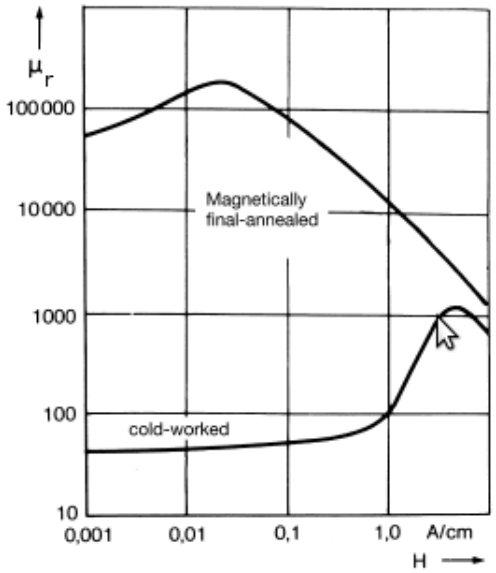

Figure 3.43 – *Effect of heat treatment on MUMMETALL (Reference [19])*

3.10 Simulation of OUFTI-1's attitude

Simulink and the "ode45" solver of Matlab are used for the simulations of OUFTI-1's attitude. The block diagram for the attitude simulations is given in Appendix A.2.

Many calculations are performed at each time step, and the time steps can not be higher than about one second. Simulations of several days in orbit are therefore difficult to perform. This is mainly due to CPU time and memory allocations. Simulations of one to two days have however been obtained as seen in Figure 3.44. The estimation of a stabilization time can be obtained by interpolation. The satellite will take about 15 days to stabilize, which is in accordance with the analytic estimation developed in Section 3.9.2.

3.10.1 Effects of the environmental torques

The damping of the hysteretic bars is quite low, and the effect of environmental torques could therefore be feared. The environmental torques are of the order of $10^{-9} N.m$ and the aerodynamic torque even go up to $10^{-7} N.m$ when the satellite altitude is lower than 400 km. This can be seen in Figure 3.45.

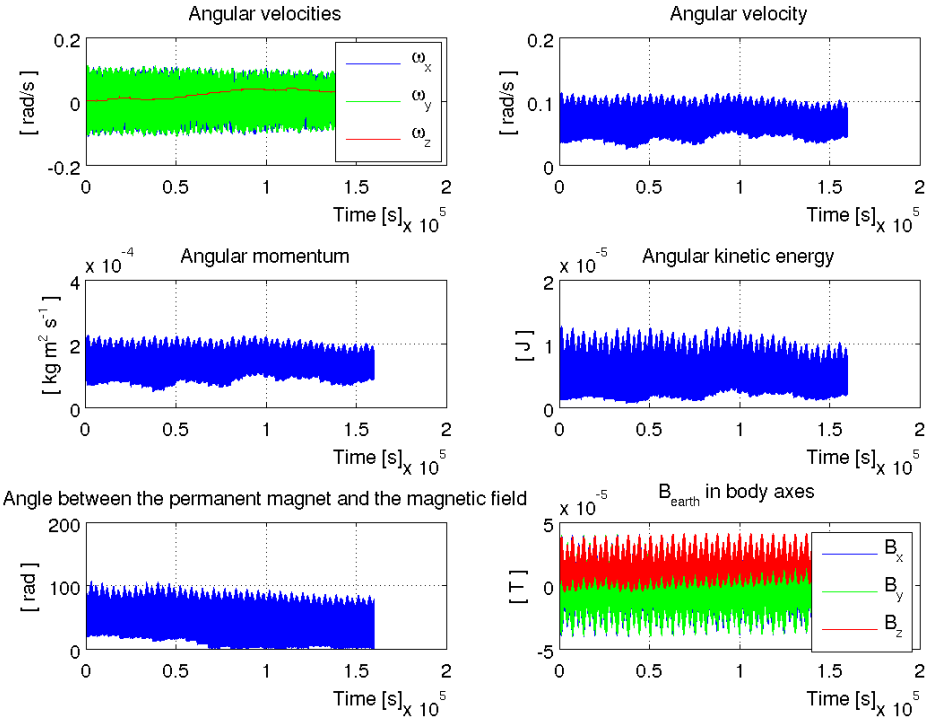

Figure 3.44 – *Simulation of the attitude over a time period of 45 hours*

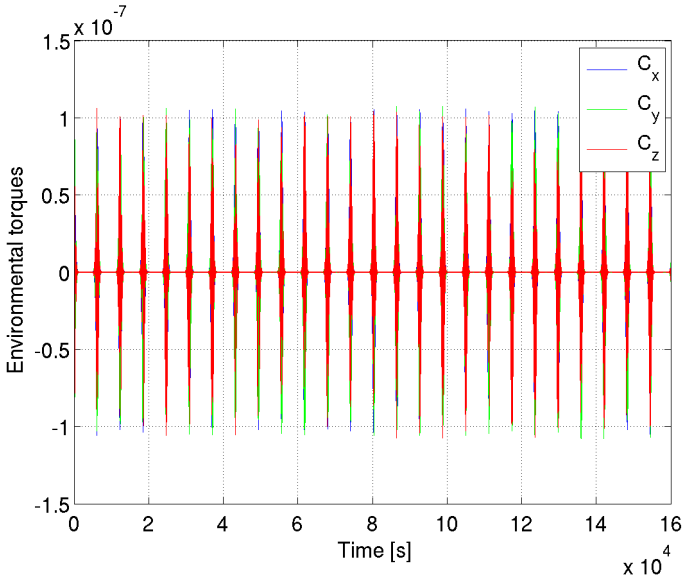

Figure 3.45 – *Environmental torques*

Since $\frac{d\boldsymbol{I\omega}}{dt} = \boldsymbol{T}_{tot}$, secular torques of that magnitude would accelerate the rotation of the satellite much faster than the damping occurs. Even in considering a very optimistic $T_{tot} = 10^{-9} N.m$, the corresponding angular acceleration is $\dot{\omega} = 5 \cdot 10^{-7} rad/s^2$. After about ten days , angular velocity could grow by 0,1 rad/s. However, as it is explained in Section 2.4, the torques are cyclic, and they do not have a significant continuous contribution. Their distribution can be considered as stochastic and they therefore do not imply an angular

acceleration over a long period of time. Figure 3.46 illustrates the angular momentum generated by environmental torques. The "discontinuities" come from the transit into the lowest altitude part of the orbit, which generates high environmental torques.

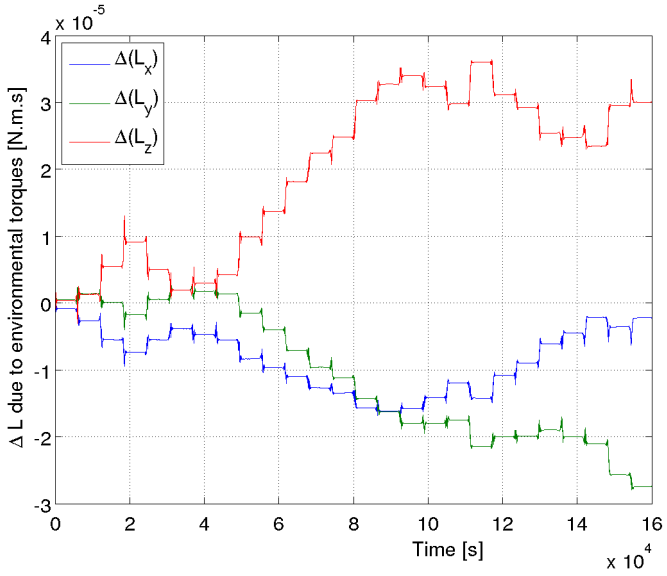

Figure 3.46 – *Angular momentum generated by environmental torques*

The angular momentum differences due to environmental torques over that period of time is of the same order of magnitude as the ones produced by the hysteretic torques, which makes the interpolation more difficult and approximative.

3.10.2 System resolution

The remaining angle between the magnet and the hysteretic rods can be important when one ignores the finite elongation of the rod. The remaining magnetic moment would then be given by $\frac{B_r}{\mu_0}V$. For a volume corresponding to the two parallel bars with a length of $80mm^3$ and a radius of $1mm^3$, it is $0.07A.m^2$.

$$\alpha = \arccos\left(\frac{\left|\vec{\mu_{magnet}}\right|}{\left|\vec{\mu_{tot}}\right|}\right) = \frac{0.32}{\sqrt{0.32^2 + 0.07^2 + 0.07^2}} \approx 20^\circ$$

This is however a very pessimistic result since the hysteresis cycle is not covered thoroughly, which implies that the remanent magnetic field is lower.

3.11 Attitude determination of OUFTI-1

The goal of the attitude determination of OUFTI-1 is to get an estimation of the rotational speed in orbit. This will provide a feedback which allows to compare with the simulations that were performed.

Many sensors exist to determine the attitude. In this case, it is advantageous to use the existing solar panels as analogue sun sensors. The accuracy is fairly rough but it does not necessitate adding any sensors on-board of the nanosatellite. According to the power the satellite gets on each side, the position of the sun with respect to the satellite can be determinated. This kind of 2 axis sun sensor has a precision of the order of a few degrees, which is enough for our purpose. Since it is desired not to use any additional sensor, there is no possibility to retrieve any information about the rotation of the satellite around the sun vector. The information which must be retrieved is therefore the rotational speed perpendicular to the sun vector.

We neglect the 0.5^o angular diameter of the sun viewed from the Earth and consider the sun rays as parallel. The Energy flux E through a surface of area dA with unit normal $\boldsymbol{N}$ is then

$$E = \boldsymbol{P} \cdot \boldsymbol{N} dA$$

where $\boldsymbol{P}$ is the Poynting vector. The power transmitted to the photocells on the faces +x, +y and +z will therefore be

$$E_x = E_{max} sin\theta cos\phi$$

$$E_y = E_{max} sin\theta sin\phi$$

$$E_z = E_{max} cos\theta$$

where E_{max} is the power transmitted to the photocells when the face is perpendicular to the solar rays. It is given by

$$E_{max} = C_s \cdot Efficiency \cdot Panels' area$$

where C_s is the solar constant which fluctuates from 1.41 kW/m^2 in early January to 1.32 kW/m^2 in early July due to the Earth's varying distance from the Sun.

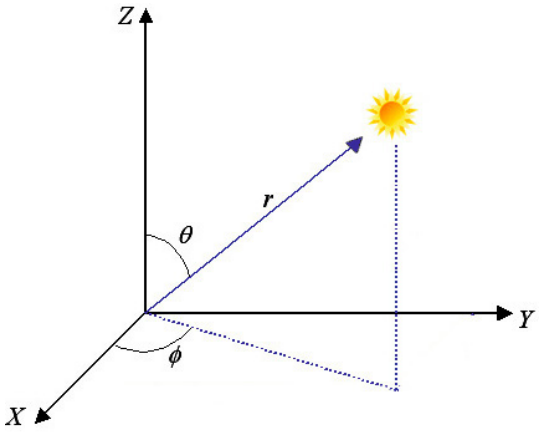

Figure 3.47 – *Sun vector representation*

The sun vector has a unit length, and it gives orientation information. It is given in the body frame by

$$v_s = \begin{pmatrix} sin\theta cos\phi \\ sin\theta sin\phi \\ cos\theta \end{pmatrix}$$

It is now assumed that the efficiency of the solar cell does not depend on the power transmitted, nor on the incidence angle. X, Y and Z are defined as being ± 1 depending on the sides that are reached by the solar rays. The sun vector can then be expressed as

$$v_s = \begin{pmatrix} X & & \\ & Y & \\ & & Z \end{pmatrix} \begin{pmatrix} E_x \\ E_y \\ E_z \end{pmatrix} \frac{1}{E_{max}}$$

E_{max} is estimated thanks to this formula taken into account the fact that v_s must have a unit length.

One problem remains. The OUFTI-1 satellite has only five faces covered with solar panels. This means that half the time measurements from only two faces are obtained. E_{max} can then be estimated thanks to the previous measurements when three faces are towards the Sun.

From different measurements of E_x, E_y and E_z, the rotational speed can be deduced. The frequency of the measurements must be higher than twice the angular velocity expressed in turns per second to avoid aliasing. That is assumed in the following.

The sun vector in body axes at different times gives an estimation of the rotational speed perpendicular to the sun vector. The rotation angle θ between time t and $t+1$ is given by

$$v_s^t \cdot v_s^{t+1} = cos\theta$$

The magnitude of the rotational speed perpendicular to the sun vector is therefore calculated by

$$\|\boldsymbol{\omega_s}\| = \frac{arcos(v_s^t \cdot v_s^{t+1})}{\Delta t}$$

Moreover $\boldsymbol{\omega_s}$ is orthogonal to v_s^t and v_s^{t+1}. The sense and direction of $\boldsymbol{\omega_s}$ is given by

$$v_s^t \wedge v_s^{t+1}$$

The measurements that are observed over time contain noise and different inaccuracies. To lessen the errors a Kalman filter can be used.

What precision can be expected?

The sine model of the power transmitted to one solar panel that was described here is an approximation. A solar cell produces power proportional to the light flow in the linear range when the efficiency is constant, but non-linearities can appear. They differ from one solar panel system to another. Improvements in the model can thus be achieved by taking those non-linearities into account.

Significant errors appear when the angle of incidence is close to 0° (when sunlight is almost perpendicular to the solar cell) because a small change in θ does not lead to a significant relative change in the power transmitted. Significant errors also appear when the angle of incidence is close to 90° (when sunlight is almost parallel to the solar cell) because the sine model is inaccurate for these angles. Moreover the power transmitted to the solar cell is low and other perturbations (albedo, ...) can thus blur the estimation.

Other sources of errors come from the 0.5^o angular diameter of the sun which is not taken into account in this model. Moreover temperature directly impacts the cells'efficiency. Long term fluctuations such as the fluctuation of the solar constant and solar cells'efficiency also limits accuracy.

3.12 Conclusion

In this chapter, the two major issues for a PMAS were identified and studied. The finite elongation of the hysteretic rods drastically reduces the PMAS efficiency, and the interaction between magnet and rods can reduce it further if it is not carefully studied. Those problems are sometimes not taken into account in the literature or too roughly estimated. One example is the Delfi-C3's case. The design of its PMAS neglected those two phenomena, which led to low performance as well as deceptive predictions of the attitude behaviour.

A design of the PMAS has been developed for the OUFTI-1 nanosatellite in which a compromise has been found between the different constraints on the design. The magnet and the hysteretic materials have been ordered and received. The final shaping and heat treatment of the hysteretic rods is explained and the magnet doesn't require any further treatment.

Finally, a method to get an estimation of the rotational speed in orbit thanks to the existing solar panels has been developed.

4

Towards an active control for Oufti-2

Concerning OUFTI-2, the objective of this master thesis is to analyse the feasibility of an active control to meet the requirements of the mission. The main parts of the active control will be covered, and the critical points will be developed more deeply.

In this chapter, the requirements are defined, and the different existing possibilities for attitude determination as well as attitude control are covered.

4.1 Payload, orbit and requirements

A first estimation of the requirements was made in collaboration with the Royal Meteorological Institute of Belgium (RMI) and the OUFTI-2 team.

- The attitude control system should achieve a *pointing accuracy of less than* 3^o *for earth and sun pointing*, and it should maintain a *pointing stability of about* $1^o/s$. Simba will have a field of view large enough in order to allow slight misalignment without missing any radiations coming from the Earth.
- Sun pointing should occur about once a month during about one orbit. Otherwise it should point to the Earth.
- The *pointing knowledge of the sun should be of the order of* $0.1°$ in order to measure the sun flux accurately. According to RMI, a specific sun sensor can be considered to meet this particular requirement.

Other requests have been formulated. These demands do not however directly concern the feasibility study, and they should therefore be taken into account in the next phase.

- A slight manoeuvre should be made possible during Earth observation when the sun goes through the Earth skyline so that measures are not disrupted by the sun. This manoeuvre could be avoided depending on the chosen orbit.
- The spatial uniformity of the cavity should be checked by sweeping the incidence angle of sun rays on the instrument.
- The cosmic microwave background should be pointed during one orbit and once a month.

4.2 Attitude determination

The attitude of a satellite is determined by measuring the directions from the spacecraft to some known points of interest. Each of those provides a unit vector measurement which brings two pieces of information. For instance, a spacecraft equipped with a sun sensor has two known quantities, and the rotation along the sun vector is undetermined. For precise attitude determination, an overdetermined attitude (at least two directions) with gyroscopes is often used together with a statistical method such as a Kalman filter. A Kalman filter lessens the overall error on attitude estimation by incorporating measurement history. The book published by Wertz (Reference [50]) provides many information on the subject.

A full three-axis knowledge requires at least the knowledge of two directions of observables. Indeed, with the measurement of a single direction, the rotation around the measured direction is unknown. More than two sensors can be used, and the attitude determination algorithm of the satellite uses all the different measurements to provide an estimation of the current attitude.

The attitude determination part of an the active attitude control system is essential. On the one hand the attitude determination errors will be superimposed to the attitude control part misalignment. On the other hand an accurate knowledge of the attitude of the OUFTI-2 nanosatellite is needed for the payload needs.

Attitude determination is a huge field in itself, and a deep study of the determination part is out of the scope of this feasibility study. All the suitable sensors commercialy available will therefore not be studied. It is however necessary to have an idea of the attitude determination accuracy which is achievable, and the most common attitude determination hardware types for nanosatellites are shortly presented here. The criteria to choose the sensors are, among others, their mass, their size, their power consumption and their accuracy.

4.2.1 Sun sensors

Sun sensors are the most widely used sensors in attitude determination. They are sun detectors which measure one or two angles. Available sun sensors for CubeSats can provide an accuracy of less than one degree. The main drawback of that kind of sensors is that measurements are not available during the eclipse period.

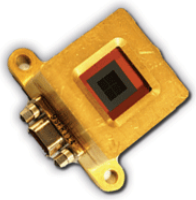

Figure 4.1 – *TNO sun sensor available on http://www.cubesatshop.com*

	TNO sun sensor	Comtech AeroAstro's medium sun sensor
Accuracy	0.5°	1°
Field Of View	128° × 128°	60°
Mass	50g	36g
Size	$30 \times 30 \times 14mm$	$20 \times 20 \times 10mm$

Table 4.1 – *Parameters of two commercially available sun sensors*

The use of a Micro-Opto-Electro-Mechanical System (MOEMS) sun sensor is a possibility in order to reduce the relatively important weight and volume of a sun sensor. The Technical University of Denmark has designed a promising MOEMS sun sensor for DTUsat. It measures about $7 \times 8mm^2$, and it has a FOV of about 70°. It has been designed and tested. Resolution better than 1° has been obtained in the FOV of 40°, and beyond those angles, the resolution is slightly higher than 1°.

A main issue for OUFTI-2 is the pointing knowledge of the sun which should be of the order of 0.1°. This is an important issue which requires at least one fine sensor on the instrument's side.

4.2.2 Magnetometers

Magnetometers are simple and light sensors which measure the local magnetic field strength. A single three-axis magnetometer measurement can give two axes worth of attitude information. Magnetometers can be found as Micro-Electro-Mechanical Systems (MEMS), and they provide an accuracy of about one degree. The main cause of inaccuracy comes from the earth magnetic field models. Moreover, magnetometers can be subjected to important errors due to special momentary conditions such as sun storms.

The use of magnetometers often requires to schedule the use of the magnetic torquers such that they do not create any magnetic field when measurements are taken. An other possibility if the magnetometers do not saturate during the use of magnetic torquers is to retrieve the contribution of the magnetic actuators from the earth magnetic field measurement.

4.2.3 Gyroscopes

Gyroscopes do not provide the direction of an observable function as other sensors do, but they detect the spinning rate for each axis rather than the orientation itself.

The bias, or bias error, is the signal output when it is not experiencing any rotation. There always exists a small drift in the gyroscope bias over time which must often be compensated by other sensors to get accurate results.

4.2.4 Star sensors

A star tracker, or star sensor, is an optical device that measures the positions of stars using photocells. It compares the measurements to its database in order to determine the attitude. This type of sensor allows very accurate attitude determination typically lower than 0.1°. Its size and weight are often an issue in a nanosatellite.

A commercially available star sensor for CubeSat is the "SPEC's Nanosatellite Sensor Suite". It combines a GPS and imaging sensors (for star tracker and earth reference) into a single module that supplies attitude and position data for navigation and control of small satellites. The main parameters are summarized in Table 4.2.

Imaging Sensor	CMOS Digital Imager
Size	$9 \times 10 \times 3cm$
Angle accuracy direction	$0.01°$
Position accuracy	1m

Table 4.2 – *A few parameters of the SPEC's Nanosatellite Sensor Suite*

4.3 Attitude control

4.3.1 Magnetic torquers

A magnetic torquer (also known as magnetotorquer, torque rod or torque bar) is an actuator used for satellite attitude control. The principle is to produce a controllable magnetic moment μ which interacts with the Earth's magnetic field to produce a mechanical torque onto the satellite. This torque is given by

$$T = \mu \wedge B_{Earth} \tag{4.1}$$

Magnetic torquing method is attractive for attitude control of small satellites in low Earth orbits where stringent pointing accuracy is not required. Magnetic torquers are light, simple and low-power consuming. They use electrical power in order to generate controllable torques. However, Equation 4.1 highlights the principal problem of magnetic actuators : the system is under-actuated. The torque rods can only provide a torque about the directions that are perpendicular to the local magnetic field vector.

In a rough approximation, the Earth is a magnetic dipole. The smallest magnetic field for a given altitude is then above the equator, and it is given by

$$B_{Earth} = \frac{B_0}{R^3}$$

where $B_O \approx 3 \cdot 10^{-5}T$ and $R = \frac{R_E+h}{R_E}$ with h being the altitude and R_E the Earth radius which is $6350km$. The magnetic actuators must be sized optimally taking that effect into account.

The necessary magnetic moment to conteract the disturbance torques can be estimated. The higher control torque is needed at the perigee ($h \approx 400km$) where it must counteract the atmospheric drag. The necessary control torque is of the order of $10^{-6}Nm$. B_{Earth} is $25\mu T$ at the perigee, and a magnetic moment from the magnetic torquer of the order of $5 \cdot 10^{-2}Am^2$ is therefore needed. A more accurate value of the needed magnetic moment will be found thanks to the simulations.

A magnetic torquer rod is essentially a long metallic wire, which can be wounded either around a ferromagnetic core or simply air. With a core, the magnetic torquer can generate a larger magnetic dipole moment with lower mass, less room and lower power consumptions, but it is at the expense of a limited linear range and possible residual magnetic moment. The two types of magnetic torquers are briefly discussed here.

Magnetic torquers without ferromagnetic core

The main advantage of using a coil without ferromagnetic core is its simplicity. The generated magnetic moment can be precisely and easily adjusted . It linearly depends on the current, and it is given by

$$\boldsymbol{\mu} = NIA\boldsymbol{n}$$

where $\boldsymbol{n}$ is the unit vector perpendicular to the loop, N is the number of turns, I is the current in the coil, and A is the area of the coil plane.

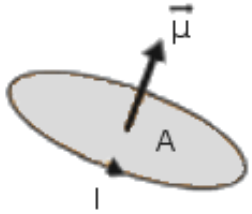

Figure 4.2 – *Magnetic moment created by a single loop of wire*

The optimum is to obtain the best required magnetic moment with the smallest volume of wire as well as the smallest power consumption. Let l_w and A_w be the length and the cross-sectional of the wire, respectively. A square coil with side length s is assumed. With that geometry, the number of turns is given by

$$N = \frac{l_w}{4s}$$

The magnetic moment can then be expressed as

$$\mu = l_w A_w J \frac{s}{4} \tag{4.2}$$

For a given current density J, μ is proportional to s and the wire volume V_w. A square side as large as possible has to be used, and a compromise between the magnetic moment and the volume has to be found.

The power consumption can be optimized under the constraint that J must be taken as the maximum current density safely allowed. The accepted current density is about $5A/mm^2$ for copper on earth, but due to the absence of convection this limit is reduced. An accurate value depends on the geometry of the set-up, and it could be given by a thermal analysis. The power consumption can be calculated by

$$P = VI = VJA_w$$

Considering the available voltage being fixed, the power consumption decreases with the cross-sectional area. This holds without changing the magnetic moment if the total volume

of wire is kept constant. An important limitation is that A_w cannot be too small because the resistance of the wire is given by

$$R_w = \frac{\rho_e l_w}{A_w} = \frac{\rho_e V_w}{A_w^2}$$

where ρ_e is the electrical resistivity. The resistance must be smaller than $\frac{V}{I}$, and this leads to the following condition

$$A_w \geq \frac{\rho_e V_w J}{V} \tag{4.3}$$

The optimum is to make that condition hold with a strict equality, but if due to practical considerations, that is not possible, a resistance must then be added in series

$$R_{series} = \frac{V^2}{P} - R_w$$

In order to get ideas of the possibilities offered by this type of magnetic torquers, some assumptions can be made. The available voltage is considered to be fixed at 3V and the maximum current density as $J_{max} = 1A/mm^2$. The length of the square-coil side s is taken as 8cm. The electrical resistivity of copper is $\rho_e = 17,2n\Omega.m$, and the mass density of copper is $\rho_d = 8,9kg/dm^3$. With these assumptions, some possible magnetic torquers are described in Table 4.3. The wire insulation is not taken into account in the mass, cross-sectional area and volume of the wire.

$P(W)$	$V(V)$	$J(A/mm^2)$	$m(g)$	$A_w(mm^2)$	$V_w(mm^3)$	$l_w(m)$	$R_{series}(\Omega)$	$\mu(Am^2)$
0,05	3	1	20	0,017	2247	134	40,9	0,045
0,1	3	1	30	0,033	3371	101	37,8	0,067
0,1	3	1	50	0,033	5618	169	3,0	0,112

Table 4.3 – *Possible magnetic torquers without ferromagnetic core*

As can be seen on Table 4.3, the maximum obtainable magnetic moment is proportionnal to the mass due to Equation 4.2. To limit the power consumption, a cross-sectional area as small as possible but which respects Equation 4.3 has to be used. According to equation 4.2, it can be noted that the ratio magnetic moment/mass can be enhanced proportionally to J_{max}. It is then important to determinate it accurately to obtain the best efficiency without risk of burning the wire.

Magnetic torquers with ferromagnetic core

A ferromagnetic core rod will enhance the efficiency of the magnetic torquer, but a main drawback comes from the non-linear hysteresis. Different possibilities exist to take care of the non-linear behaviour. The first possibility is simply to stay in the linear range of the ferromagnetic coil. This technique however limits the magnetic moment for a given weight of ferromagnetic core. The second possibility is to use some methods to extend the linear range of the torquer. For fairly big magnetic torquers, a common way to do so is to sense the magnetic field near the torquer in order to generate a feedback signal. Another way is to use a mathematical model of the hysteresis.

Some magnetic torquers for CubeSat applications are commercially available. Magnetic torquers with ferromagnetic core and a magnetic moment of $0,1$ to $0.2A.m^2$ are commercialized by Zarm technik.

Figure 4.3 – *Magnetic Torquer MT0.1-1 for PCB mounting by Zarm technik (Reference [51])*

Summary

Table 4.4 compares the different possibilities. The magnetic torquers with ferromagnetic core have a smaller mass, and take less room, but the power consumption is not an advantage for the magnetic torquers provided by Zarm technik.

	mass(g)	power(mW)	voltage(V)	magnetic moment(Am^2)
without core	20	≈ 50	3	0.04
without core	30	≈ 100	3	0.07
without core	40	≈ 100	3	0.1
With core(MT0.1-1)	2.9	300	5	0.1
With core (MT0.2-1, mass optimized)	6.2	300	5	0.2
With core (MT0.2-1) power optimized)	9,9	150	5	0.2

Table 4.4 – *Possible magnetic torquers*

4.3.2 Momentum exchange devices

The first main difference between momentum exchange flywheels and other types of actuators is that they can only exchange angular momentum with the satellite. The flywheels include control momentum gyroscopes, momentum wheels and reaction wheels.

- A control momentum gyroscope (CMG) consists of a spinning rotor and one or more motorized gimbals that tilt the spinning rotor. As it tilts, the change in angular momentum causes a gyroscopic torque that rotates the spacecraft.
- A momentum wheel is mainly used for gyroscopic stabilization of spacecraft. They have high rotation speeds (around 6000 RPM) and mass.
- A reaction wheel is a type of flywheel used by satellites to change their angular momentum without using fuel for rockets or other reaction devices.

The reaction wheels are the most common, and they have now been used in several nanosatellites. Many of the launched CubeSats have chosen for attitude control magnetic torquers for their simplicity even though they offer low pointing accuracy and slow manoeuvres when compared to momentum exchanged devices. The launch of cubesats with reaction wheels actually started in 2008 when two satellites with reaction wheels, AAUsat-2 and CanX-2, were launched on a Polar Satellite Launch Vehicle (PSLV).

A first possibility for the reaction wheels is to design it from commercially off-the-shelf components (COTS). They can basically be built from a suitable DC-micro-motors and an inertia wheel (the AAUsat-2 approach). A second possibility is to use commercially available reaction wheels such that the CanX-2 wheel which was developed in cooperation with Sinclair Interplanetary.

Nominal Momentum	$0.01 kgm^2s^{-1}$ $(N \cdot m \cdot s)$
Nominal Torque	$10^{-3} kgm^2s^{-2}$ $(N \cdot m)$
Size	$50mm \times 50mm \times 30mm$
Mass	120 g mass
Control Mode	Speed or Torque, built-in control CPU
Heritage	CanX-2

Table 4.5 – *Main characteristics of one type of the reaction wheels developed at the Space Flight Laboratory of the University of Toronto in collaboration with Sinclair Interplanetary*

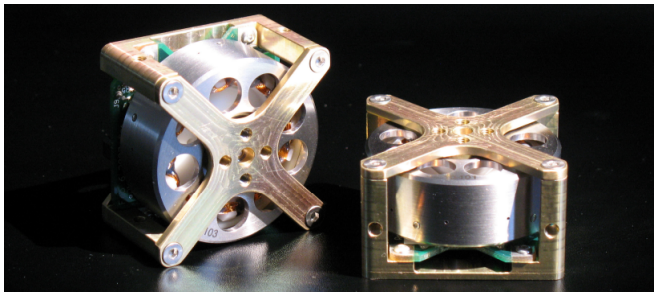

Figure 4.4 – *Picosatellite reaction wheels developed at the Space Flight Laboratory of the University of Toronto in collaboration with Sinclair Interplanetary (Reference [49])*

4.3.3 Thrusters

Low thrust propellant or electric systems used to produce torques onto the satellite are becoming available for nanosatellites. The drawback of thrusters is their cost, their weight and the limited amount of propellant that is available for the whole mission. Thrusters are not common in nanosatellites however they represents a growing field. They have for instance been used in the CubeSat ION where four micro-vacuum arc thrusters are capable of lateral movement and fine control of the attitude.

4.4 Existing hardware for active control

There exists commercially available packages comprising sensors as well as actuators. The Space Flight Laboratory at the University of Toronto offers an actuator and sensor package that draws directly from the CanX-2 heritage. The main informations are summarized in Table 4.6.

Achievable pointing accuracy	2 deg in sunlight
Actuators	3 reaction wheels, 3 magnetic torquers
Sensors	Sun sensors and magnetometers
Dimensions	$95 \times 95 \times 61$ mm box containing reaction wheels, four sun sensors and three magnetic torquers. Two sun sensors and one magnetometer external to box.
Heritage	CanX-2

Table 4.6 – *Space Flight Laboratory at the University of Toronto ADCS package*

Achievable pointing accuracy	1 deg
Actuators	3 reaction wheels, 3 magnetic torquers
Sensors	Not specified
Dimensions	100 x 100 x 79 mm box
Price	46.000 Euro
Heritage	Not specified

Table 4.7 – *ADCS package IMI-100 from http://www.cubesatshop.com*

4.5 Conclusion

The existing types of actuators in attitude control have been listed. In the next chapter, the attitude control with and without reaction wheels will be studied further.

The existing types of sensors for attitude determination have been studied. The attainable accuracy is about 1° without star sensors and better than 0.1° with it. The attitude determination is not the main issue in this feasibility study but the pointing knowledge of the sun of about 0.1° will necessitate special care. A deep study of the choice of sensors and the attainable attitude determination accuracy is out of the scope of this feasibility study.

5 Simulations of an active attitude control

Chapter 4 described the different possibilities for three-axis attitude control. A simulator will be developed to assess the obtained attitude control achieved with the different actuators. An automatic feedback controller will be included in the simulator to generate control torques and orient the spacecraft. The goal is to find the simplest solution which meets the requirements. One of the main questions is to determinate whether magnetic torquers alone are sufficient to obtain acceptable attitude control. The improvements obtained with reaction wheels will also be discussed.

5.1 Parametrization of the attitude

The attitude of a satellite is the orientation of a three axis coordinate system (the body frame) in respect of a reference coordinate system (the ECI frame for instance). It is described with three independent parameters such as Euler angles. However the attitude is often described with more parameters such as with the Direction Cosine Matrix (DCM) or quaternions.

5.1.1 The Direction Cosine Matrix (DCM)

Let $\boldsymbol{u}$,$\boldsymbol{v}$,$\boldsymbol{w}$ be the unit vectors which define the coordinate system of the body frame. The direction cosine matrix completely describes the attitude, and it can be defined as

$$\mathbf{A} = \begin{bmatrix} \hat{\mathbf{u}}_x & \hat{\mathbf{u}}_y & \hat{\mathbf{u}}_z \\ \hat{\mathbf{v}}_x & \hat{\mathbf{v}}_y & \hat{\mathbf{v}}_z \\ \hat{\mathbf{w}}_x & \hat{\mathbf{w}}_y & \hat{\mathbf{w}}_z \end{bmatrix}$$

The advantage of this representation is that the direction coordinate matrix maps vectors from the reference coordinate system to the body frame and conversely

$$\boldsymbol{a}_{body} = \mathbf{A}\boldsymbol{a}_{ref}$$

$$\boldsymbol{a}_{ref} = \mathbf{A}^{\mathbf{T}}\boldsymbol{a}_{body}$$

On the other hand, it uses six redundant parameters, and it is time consuming for calculations.

5.1.2 Quaternions

Unit quaternions provide a convenient mathematical notation for representing rotations. They are more efficient than rotation matrices, and compared to Euler angles, they are more practical and avoid singularities. These reasons make it a clever choice although other ways are also used. Quaternions have applications in many fields of sciences such as computer graphics, robotics and of course attitude control of satellites. A short introduction to quaternions is presented, and the properties used in the model are also introduced.

Quaternions are an extension of complex numbers: $\mathfrak{q} = w + x\boldsymbol{i} + y\boldsymbol{j} + z\boldsymbol{k} = (w, \boldsymbol{v})$. The real part is w and the imaginary part is $x\boldsymbol{i} + y\boldsymbol{j} + z\boldsymbol{k}$ which is also noted $\boldsymbol{v}$. Properties of $\boldsymbol{i}, \boldsymbol{j}, \boldsymbol{k}$:

$$\begin{aligned} &\boldsymbol{i}^2 = \boldsymbol{j}^2 = \boldsymbol{k}^2 = -1 \\ &\boldsymbol{ij} = \boldsymbol{k},\ \boldsymbol{ji} = -\boldsymbol{k} \\ &\boldsymbol{jk} = \boldsymbol{i},\ \boldsymbol{kj} = -\boldsymbol{i} \\ &\boldsymbol{ki} = \boldsymbol{j},\ \boldsymbol{ik} = -\boldsymbol{j} \end{aligned}$$

Product of quaternions (not commutative):

$$\mathfrak{q}_1\mathfrak{q}_2 = (w_1w_2 - \boldsymbol{v}_1.\boldsymbol{v}_2,\ w_1\boldsymbol{v}_2 + w_2\boldsymbol{v}_1 + \boldsymbol{v}_1 \wedge \boldsymbol{v}_2)$$

Conjugate quaternion:

$$\begin{aligned} &\bar{\mathfrak{q}} = w - x\boldsymbol{i} - y\boldsymbol{j} - z\boldsymbol{k} \\ &\mathfrak{q}\bar{\mathfrak{q}} = w^2 + x^2 + y^2 + z^2 \end{aligned}$$

Unit quaternions and 3D rotations

After a brief review of the main properties of quaternions, a closer look to unit quaternions used to model rotations can now be taken. A unit quaternion respects the following rule

$$\mathfrak{q}\bar{\mathfrak{q}} = 1 \qquad \Rightarrow \qquad \mathfrak{q}^{-1} = \bar{\mathfrak{q}}$$

Rotation by an angle θ around $\boldsymbol{u}$ of a right handed Cartesian coordinate system is described thanks to

$$\mathfrak{q}_{(\theta,u)} = (\cos\frac{\theta}{2}, u_x \sin\frac{\theta}{2}, u_y \sin\frac{\theta}{2}, u_z \sin\frac{\theta}{2})$$

The rotation is clockwise if our line of sight points in the direction pointed by $\boldsymbol{u}$

The Conversion $(w, \boldsymbol{v}) \longrightarrow (\theta, \boldsymbol{u})$ is then computed as follow

$$\begin{aligned} \cos(\theta/2) &= w \\ \sin(\theta/2) &= \|\boldsymbol{v}\| \\ \boldsymbol{u} &= \boldsymbol{v}/\|\boldsymbol{v}\| \end{aligned}$$

Let $\boldsymbol{v}$ be an ordinary vector in three-dimensional space, considered as a quaternion with a real coordinate equal to zero. Then the quaternion product

$$\mathfrak{q}\boldsymbol{v}\mathfrak{q}^{-1}$$

yields the vector $\boldsymbol{v}$ rotated by an angle θ around the $\boldsymbol{u}$ axis.

Three other properties are listed here

- Inverse rotation: $\mathfrak{q}_{(\theta,u)}{}^{-1} = \mathfrak{q}_{(-\theta,u)} = \mathfrak{q}_{(\theta,-u)} = (-w, \boldsymbol{v}) = (w, -\boldsymbol{v})$

- The time derivative of the unit quaternion $\mathfrak{q}$ defining the orientation of a solid with angular velocity $\boldsymbol{\omega}$ is: $\dot{\mathfrak{q}} = \frac{1}{2}\boldsymbol{\omega}\mathfrak{q}$ with $\boldsymbol{\omega}$ expressed in the fixed coordinate system.

- If one is a rotation by α around the axis directed by vector $\boldsymbol{v}$, the other is a rotation by $360° - \alpha$ around the axis directed by vector - $\boldsymbol{v}$.

Unit quaternions and rotation of Cartesian coordinate systems

The Direction cosine matrix is directly linked to quaternions by

$$\mathcal{A} = \begin{bmatrix} -1 + 2q_1^2 + 2q_0^2 & 2(q_1q_2 + q_3q_0) & 2(q_1q_3 - q_2q_0) \\ 2(q_1q_2 - q_3q_0) & -1 + 2q_2^2 + 2q_0^2 & 2(q_1q_0 + q_2q_3) \\ 2(q_1q_3 + q_2q_0) & 2(q_2q_3 - q_1q_0) & -1 + 2q_3^2 + 2q_0^2 \end{bmatrix}$$

Let $R_{2/1}$ be the rotation matrix which maps vectors expressed in S_1 to S_2. The coordinate vector expressed in S_2 as a function of the coordinate vector expressed in S_1 is then given by

$$\boldsymbol{v}_{S2} = R_{2/1}\boldsymbol{v}_{S1}$$

Similarly let $\mathfrak{q}_{2/1}$ be the quaternion corresponding to the rotation of the Cartesian coordinate system S_1 towards S_2. Then the coordinate vector in S_2 can be expressed from the coordinate vector in S_1 by

$$\boldsymbol{v}_{S2} = \mathfrak{q}_{2/1}^{-1}\ \boldsymbol{v}_{S1}\ \mathfrak{q}_{2/1}$$

In the case of a combination of rotations, let's consider three Cartesian coordinate systems S_1,S_2,S_3.

- A first rotation of an angle θ_1 around a unit vector $\boldsymbol{u}_1$ expressed in S_1 is considered. This rotation transforms S_1 in S_2 and is described by $\mathfrak{q}_{2/1}$.

- A second rotation of an angle θ_2 around a unit vector $\boldsymbol{u}_2$ expressed in S_2 That rotation transforms S_2 in S_3 and is described by $\mathfrak{q}_{3/2}$.

The quaternion describing the composition of the two rotations which transforms S_1 in S_3 is then expressed by

$$\mathfrak{q}_{3/1} = \mathfrak{q}_{2/1}\mathfrak{q}_{3/2} \tag{5.1}$$

5.1.3 Application of quaternions to active control

The goal of sensors is to provide a unit quaternion which describes the rotation between the ECI frame and the body frame which will be called $\mathfrak{q}_{estim} = q_{2/1}$. Moreover $\mathfrak{q}_{target} = q_{3/1}$ is the quaternion which represents the rotation between the ECI frame and the expected attitude. Finally the quaternion that represents the control error in the body axes will be denoted $\mathfrak{q}_{error}$. It represents the transition between $\mathfrak{q}_{estim}$ and $\mathfrak{q}_{target}$, and it is noted $\mathfrak{q}_{3/2}$. $\mathfrak{q}_{error} = [1, 0, 0, 0]$ corresponds to a perfect pointing.

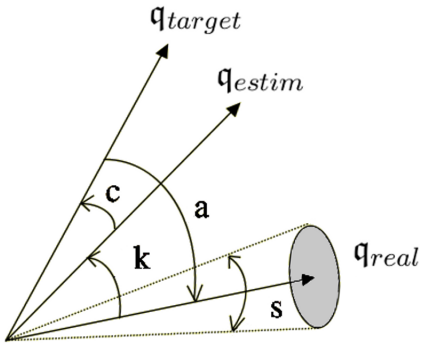

Figure 5.1 – *Representation of the different elements used in a quaternion-based attitude control.* $\mathfrak{q}_{target}$ *is the desired pointing,* q_{real} *is the actual pointing,* $q_{estimate}$ *is the estimate of pointing, a represents the pointing accuracy, s the stability, k the knowledge error and c the control error*

From Equation 5.1, one gets

$$\mathfrak{q}_{3/2} = \mathfrak{q}_{2/1}^{-1}\mathfrak{q}_{3/1}$$

which can be written equivalently as

$$\mathfrak{q}_{error} = \mathfrak{q}_{estim}^{-1}\mathfrak{q}_{target} \tag{5.2}$$

Equation 5.2 is used as a feedback for the controller.

The following property can also be noted

$$\mathfrak{q}_{2/3} = \mathfrak{q}_{3/2}^{-1} = \mathfrak{q}_{3/1}^{-1}\mathfrak{q}_{2/1}$$

5.2 Attitude determination

The simulations will be performed assuming a perfect knowledge of the attitude. In the worst case, the attitude determination error would add to the control error.

5.2.1 Torque free motion

The torque free motion has a major importance in attitude dynamics for attitude prediction and attitude control. The key concepts are described in this section.

Two types of attitude motion can occurs. *Pure rotation* is the case when the rotation axis is aligned with a principal axis. *Nutation* is the general case when the rotation axis is not aligned with a principal axis.

Complications in the description can appear if a principal axis is not aligned with a geometrical axis which defines the orientation of the attitude. The geometrical axes then rotate about the angular momentum vector. This is called *coning*. If possible, it is preferred to work with geometrical axes corresponding to the principal axes. In this case, the angular momentum vector $\boldsymbol{\omega}$ rotates about $\boldsymbol{L}$.

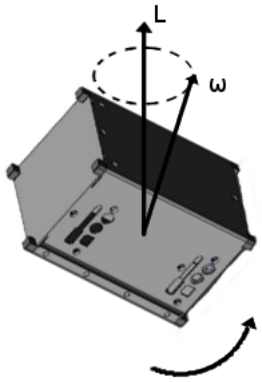

Figure 5.2 – *Nutation*

5.3 Attitude control models

The controller generates control torques and orients the spacecraft in a given attitude. The general idea behind feedback systems is to automatically correct the spacecraft attitude whenever it has been sufficiently perturbed.

5.3.1 General parameters for the active control simulations

Typical manoeuvre

The main manoeuvres that will be necessary for the nanosatellite OUFTI-2 are to point the radiometer to the Sun and to the Earth once a month. The position of the instrument is not known yet, and a simple manoeuvre will be studied as a first step. Unless otherwise specified, the initial orientation of the satellite is assumed to be aligned with the ECI frame : $\mathfrak{q}_{init} = [1, 0, 0, 0]$, and it has to rotate around y axis of an angle of 90° such that $\mathfrak{q}_{target} = [\frac{\sqrt{2}}{2}, 0, \frac{\sqrt{2}}{2}, 0]$. Afterwards, it has to keep that orientation indefinitely.

Orbit

Unless otherwise specified, the simulations are carried out on a sun-synchronous orbit with an altitude of about $650km$. The orbital parameters are summarized in Table 5.1

Orbit	Sun-synchronous
Altitude	$650km$
Inclination	98°
Period	$100min$

Table 5.1 – *Orbit parameters chosen for the phase 0 simulations*

Disturbance torques

The disturbances are torques which affect the attitude control performance. They can be either deterministic or random. Torques are called deterministic if they are known function of the spacecraft position and orientation. Typically, gravity gradient, solar radiation pressure torque or even aerodynamic torque could be considered as deterministic. However,

the uncertainty on these torques can be too large to take advantage of their model in a controller.

Torques due to aerodynamic drag and solar flux linearly depend on the distance between the gravity centre and the geometrical centre while the gravity gradient depends on the inertia matrix. The satellite inertia is calculated as a homogeneous volume of $10 \cdot 10 \cdot 20cm$ with a total mass of 2kg :

$$I_x = I_y = \frac{5ma^2}{12} = 0.0083kg.m^2$$

$$I_z = \frac{ma^2}{6} = 0.0033kg.m^2$$

The gravity centre is approximated to be at coordinates $(5 \cdot 10^{-3}, 5 \cdot 10^{-3}, 5 \cdot 10^{-3})$ in the body frame which is a distance of $0.9cm$ from the geometrical centre.

The loss of symmetry due to the double CubeSat shape of the satellite increases the gravity gradient strongly in low earth orbit as compared to a single CubeSat such as OUFTI-1. The gravity gradient is of the order of $10^{-8}Nm$ while the aerodynamic torque is of the order of $10^{-9}Nm$ at altitude of $650km$. Figure 5.3 shows the typical environmental torques applied onto the satellite during the rotation around y-axis of 90°. It can be noted that no torque around the z-axis due to gravity gradient appears since the satellite is assumed to have a symmetric inertia matrix around the z-axis.

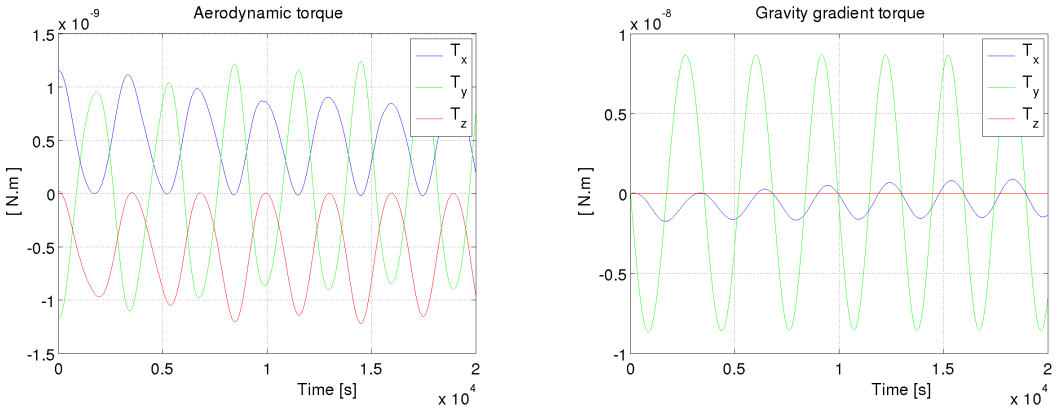

Figure 5.3 – *Typical environmental torques on a sun-synchronous orbit during the manoeuvre around the y-axis*

As explained in Section 2.4.2, the aerodynamic drag decreases very strongly with altitude while the gravity gradient drag has the same order of magnitude for any low Earth orbits. In order to reduce the gravity gradient torque, one approach is to take care of the layout of the satellite to get an inertia matrix closer to symmetry. A second approach is to include a model of the environmental torque to the controller in order to limit its effect.

5.3.2 PID controller

A Proportional-Integral-Derivative controller (PID controller) is the most widely used controller with feedback mechanism. It is one of the simplest control algorithms, and in the

absence of knowledge of the underlying process, PID controller is often the best choice. A linear PID controller is sometimes used in space applications, but more complex controller also exist (see Section 5.3.3).

The transition quaternion $\mathfrak{q}_{error}$ is first calculated from the estimation of the current attitude and the desired target. The PID controller then calculates the proportional part for the control torque to apply to the system. The integral part of the control torque is based on the sum of recent errors, and the derivative part determines the control torque based on the rotational velocities estimations.

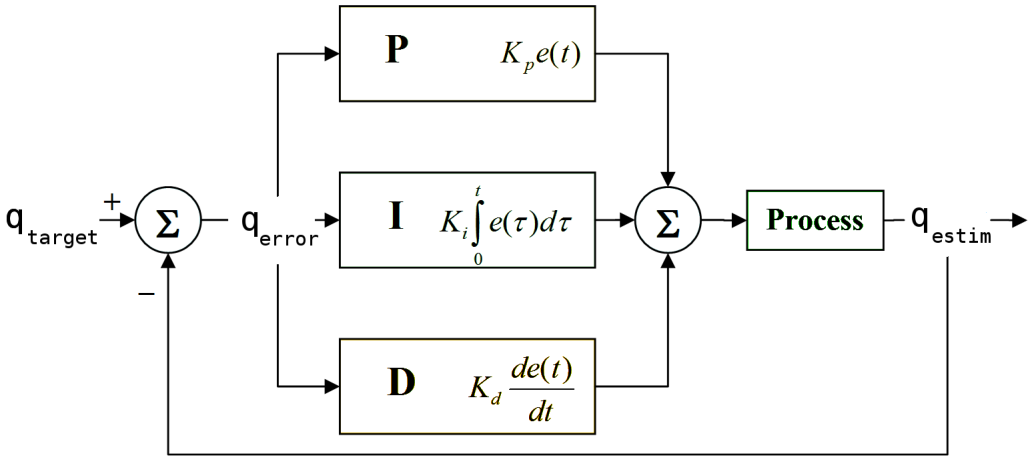

Figure 5.4 – *General PID with feedback for attitude control*

From $\mathfrak{q}_{error}$, one knows the vector $\boldsymbol{u}$ and the angle α such that rotation of an angle α around $\boldsymbol{u}$ gives the right orientation of the satellite. Angle α can be bigger than π, which means that a reorientation manoeuvre has to rotate by an angle of $2\pi - \alpha$ around $\boldsymbol{u}$:

$$\begin{aligned} &if\ \alpha > pi \\ &\quad \alpha = 2\pi - \alpha; \\ &\quad \boldsymbol{u} = -\boldsymbol{u}; \\ &end \end{aligned}$$

The proportional part of the control torque is thus ideally proportional to $\alpha \cdot \boldsymbol{u}$. The derivative part is ideally proportional to the angular velocity in body axes $-\boldsymbol{\omega}$. A Proportional-Derivative controller generates the ideal control torque $T_{control}$:

$$T_{control} = C_p \cdot \boldsymbol{u} \cdot \alpha - C_d \cdot \boldsymbol{\omega}$$

The PID parameters used must be tuned according to the nature of the system (inertia matrix, maximum control torques, ...). The determination of the parameters C_p and C_d is an important task in order to obtain an optimal behaviour. The control is however time-varying, it depends on the orbit parameters, and for magnetic actuators, the torques are limited to the plane perpendicular to the local magnetic field (see Section 5.5). For these reasons, an analytical procedure to determine them does not seem to be feasible. The choice of the parameters C_p and C_d therefore requires some iterations to get the best obtainable behaviour. An advanced method can be found in Section 5.3.3.

The three angular rates about the body axes of the spacecraft are essential for the torque control law. They can be obtained from gyroscope measurements. Generally they are mandatory not only to obtain precise angular velocity but also to obtain a precise attitude by integrating those rates (see Reference [52]). If such instrumentation is either unavailable or not included in order to simplify the hardware, the angular velocity in body axes can be estimated from the derivative of the satellite quaternion. The estimated orientation is obtained from attitude position measurements using a horizon sensor, sun, or star sensors. Since the calculated quaternions are noisy, the differentiation must naturally be performed with adequate noise filters.

The control laws proposed so far assume the existence of hardware which can generate the ideal control torques. It is however rarely as simple. Let's consider two possible types of actuators to introduce the possible difficulties.

- Magnetic torquers using the earth magnetic field
- Reaction wheels

The magnetic torquers can only apply a torque perpendicular to the local magnetic field, and the torque level is relatively low. The manoeuvres are therefore slow and relatively inaccurate if they are the only available actuators (see Section 5.5). For accurate and fast manoeuvres, the reaction wheels are often necessary (see Section 5.4).

Fuzzy control is sometimes also used in attitude control. Fuzzy control is based on continuous values between 0 and 1 for the decision variables, in contrast to classical or digital logic, which operates on discrete values of either 0 or 1. Bang-bang solutions for a satellite attitude control problem use fuzzy logic.

5.3.3 The linear quadratic regulator controller

A more advanced method than PID such as the Linear Quadratic Regulator (LQR) expresses the control problem as a mathematical optimization, and it then looks for the best controller. Let's consider the attitude dynamics written in continuous time by

$$\dot{\boldsymbol{x}} = \mathrm{A}\boldsymbol{x} + \mathrm{B(t)}\boldsymbol{u}$$

where $\boldsymbol{x}$ represents the state vector of the system and $\boldsymbol{u}$ the control vector. The general idea in the LQR is to minimize the objective quadratic function

$$J = \frac{1}{2}\int_0^{t_f} \boldsymbol{x^T(t)}\mathrm{Q}\boldsymbol{x(t)} + \boldsymbol{u^T(t)}\mathrm{R}\boldsymbol{u(t)}dt$$

with Q, R being semi-positive definite. That criterion can be understood easily. On the one hand, the minimization of $\boldsymbol{x^T(t)}\mathrm{Q}\boldsymbol{x(t)}$ implies to bring the system as close as possible to the origin ($\boldsymbol{x(t)} = 0$). By shifting the origin, the target state variables can be brought to any constant values. On the other hand, the additional term $\boldsymbol{u^T(t)}\mathrm{R}\boldsymbol{u(t)}$ penalizes large inputs, and it thus seeks to minimize the power consumption and to obtain more realistic designs since the inputs are limited. Therefore, the minimization of the objective function implies to bring the system as close as possible to the target state while minimizing the input $\boldsymbol{u(t)}$.

The goal is to find the best state feedback

$$\boldsymbol{u(t)} = -\mathrm{F(t)}\boldsymbol{x(t)}$$

to minimize the objective function. That method is often used in three-axis attitude control. It is a more advanced method than a basic PID, and it can take advantage of a the underlying process model. It was implemented for instance in the ION CubeSat developed by the University of Illinois. An outgrowth of that theory is the more recent H^{∞} theory (during the 1980's). That theory aims to give a robust controller with respect to model uncertainty (see for instance Reference [54]).

5.3.4 Detumbling controller based on B-dot

The first attitude control task to be executed after launch is stabilizing the angular rate which is sometimes called detumbling. An efficient and simple solution to detumble a satellite using magnetic actuation is the so-called B-dot ($\dot{B}$) algorithm. The control law is based on the magnetometers' measurements and the principle of a B-dot controller is to minimize the derivative of the local magnetic field vector. The applied torque is then opposite to the derivative of the magnetic field vector in the body axes $\boldsymbol{\dot{B}_{body}}$:

$$T = -k\boldsymbol{\dot{B}_{body}}$$

where k is a controller gain. B can be used directly without the usual cross product because the derivative of the local magnetic field is perpendicular to the local field. The magnetic actuators are then well suited to provide such a torque. That method is similar to a "D controller" with the component of the torque along the earth magnetic field removed.

5.4 Attitude model with full controllability

The principle of conservation of angular momentum says that a rotating wheel inside the satellite produces angular torque when accelerated. The change of angular momentum is transferred between the wheels and the satellite.

For full controllability, at least three reaction wheels with non-parallel rotational axes are required. The reaction wheels can be mounted with the rotational axes in any direction relatively to the body frame. It can however be noted that the rotational axis of each three reaction wheels parallel to the satellite body axes makes the simplest control algorithm since torques around each axis can be applied independently. A fourth wheel is however often used to increase reliability. The additional wheel can provide reduced torques around each of the three initial perpendicular axes, and the controllability is then single failure free.

In any case, the total momentum of the reaction wheels can be expressed in the reference frame as $\boldsymbol{h_w} = [h_{wx}, h_{wy}, h_{wz}]$. The maximum control torques as well as the maximum angular momentum stored in each axis depends on the type of reaction wheels used and on their orientations. The control torque obtained with the reaction wheels is given by

$$\boldsymbol{T_w} = \dot{h_w}$$

A complete dynamic model of the motors which drive the wheels is necessary in order to obtain the required torque.

One drawback of a reaction wheel is that it accumulates angular momentum if used to counteract constant external disturbances. If nothing is done, it reaches saturation, which make it unusable. The magnetic torquers or other actuators must therefore slow sometimes the wheel sometimes while preventing the angular momentum to be given back to the satellite. This process is called dumping or detumbling of the wheel. On the other hand, momentum wheels are very efficient for attitude manoeuvres. If the needed control torques have no component with null frequency, the stored momentum will not accumulate angular momentum.

Figure 5.5 shows the attitude manoeuvre of a rotation of $\pi/2$ about the y-axis. The maximum torque allowed is fixed at $10^{-6}N.m$ which is significantly less than the maximum achievable torque of the order of 10^{-4}N.m on commercially available reaction wheels for nanosatellites. Since the initial rotation rate is very low, the torques have very low zero-frequency component, and the angular momentum accumulated by the wheels is only temporary. The angular momentum storage on commercially available reaction wheel is $10^{-3}kg.m^2/s$ which is less than needed for the manoeuvre. At the end of the manoeuvre, if initial rotation and perturbing torques are negligible, the wheels have not accumulated angular momentum. The depointing angle in the simulation inferior of $10^{-}3$ rad, but this value does not take into account inaccuracies coming from the attitude determination part and from real actuators.

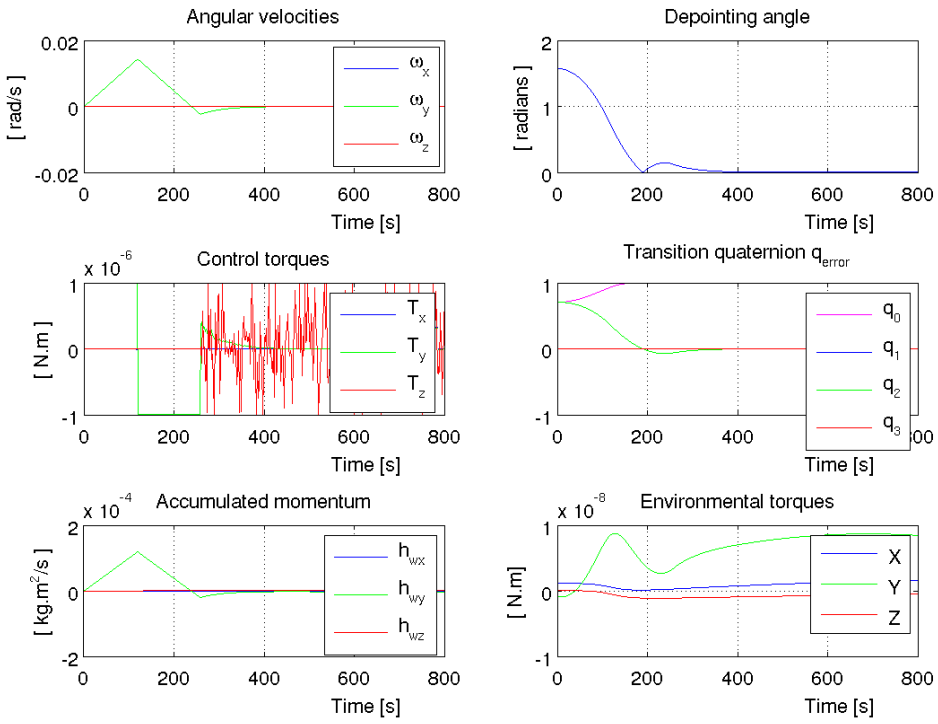

Figure 5.5 – *Attitude manoeuvre using Proportional-Derivative controller* *($C_p = 0.005$, $C_d = 0.025$)*

Figures 5.6 and 5.7 show the same manoeuvre but with different PID parameters. Larger values of the proportional term typically mean faster response, but an excessively large

proportional gain will lead to a high overshoot and oscillations.

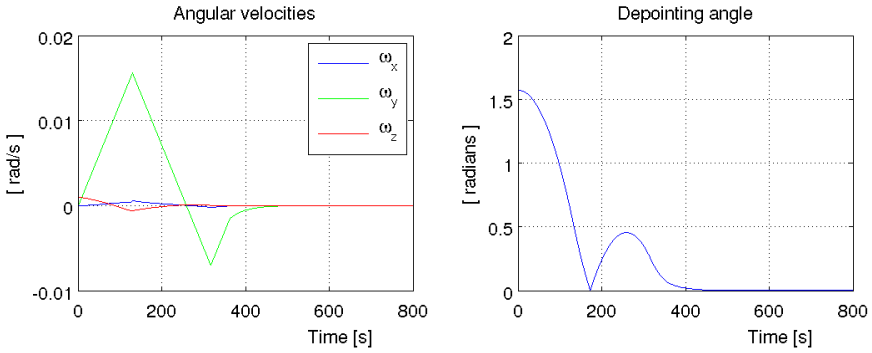

Figure 5.6 – *Attitude manoeuvre using Proportional-Derivative controller ($C_p = 0.007$, $C_d = 0.025$)*

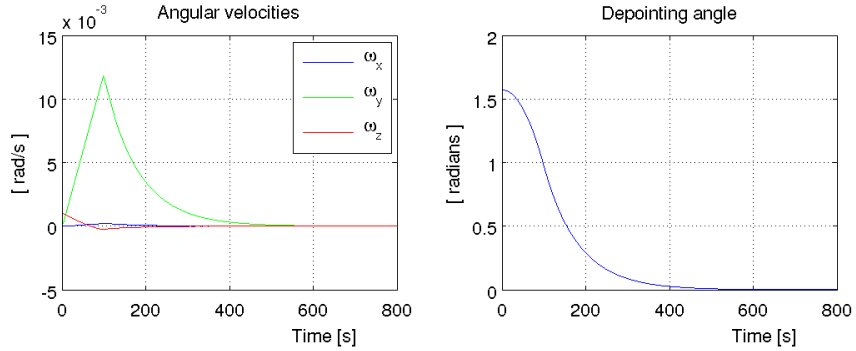

Figure 5.7 – *Attitude manoeuvre using Proportional-Derivative controller ($C_p = 0.003$, $C_d = 0.025$)*

The attitude control is usually divided into two phases : detumbling and attitude acquisition (see Figure 5.8). The objective of the first phase is to reduce the angular velocity of the satellite. The second phase is a reorientation phase. If the initial rotation rate of the satellite leads to an angular momentum which is higher than the maximum stored momentum in the wheels, only other type of actuators will be used during the first detumbling phase.

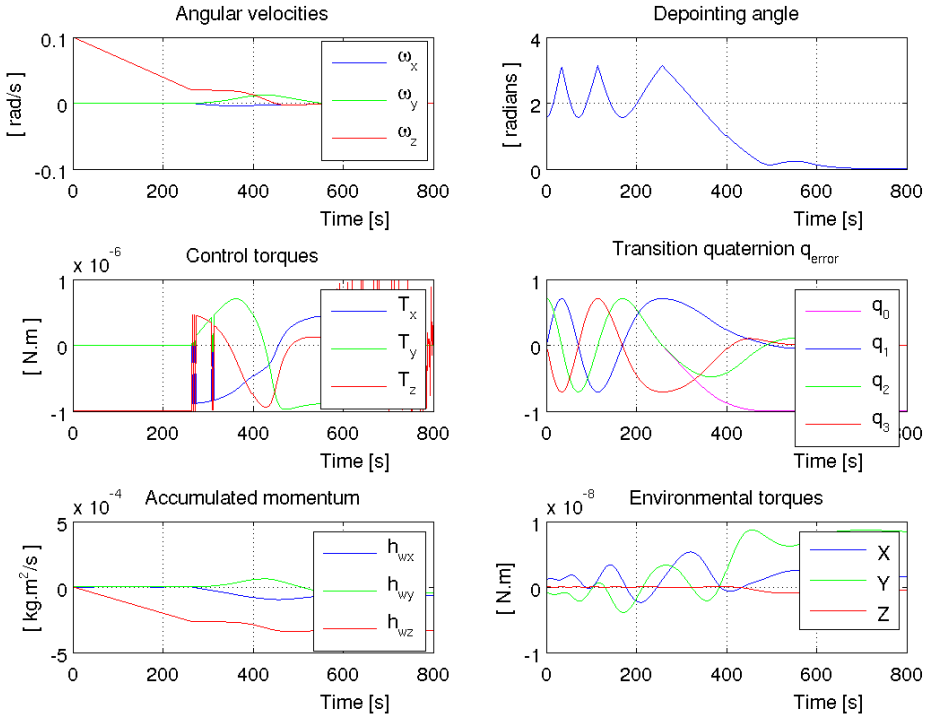

Figure 5.8 – *Attitude manoeuvre using two different phases* ($C_p = 0.003$, $C_d = 0.025$) $\omega_{init} = [0, 0, 0.1]$

For an adequate operation, a reaction wheel should be as close as possible from standstill. Indeed, it should be far from saturation to allow maximum reactivity. Moreover viscosity torques produced on a rotating wheel increase power consumption. Finally, the existence of angular momentum in the satellite causes control difficulties when manoeuvres have to be executed. The norm of the wheels' angular momentum should therefore be minimized by magnetic torquers or by a thruster. During desaturation of the wheels, the attitude is controlled to the same steady-state value, although transient errors can be induced in practice (Reference [50]).

The basic control equation for momentum unloading is

$$T = -k(\boldsymbol{h} - \boldsymbol{h}_N)$$

where k is the desaturation control gain, $\boldsymbol{h}$ is the wheels' momentum vector, and $\boldsymbol{h}_N$ is the desired wheel momentum vector. If magnetic actuators are used, the torque component along the local earth magnetic field cannot be applied, but the desaturation occurs on average while the satellite experiences different earth magnetic field directions.

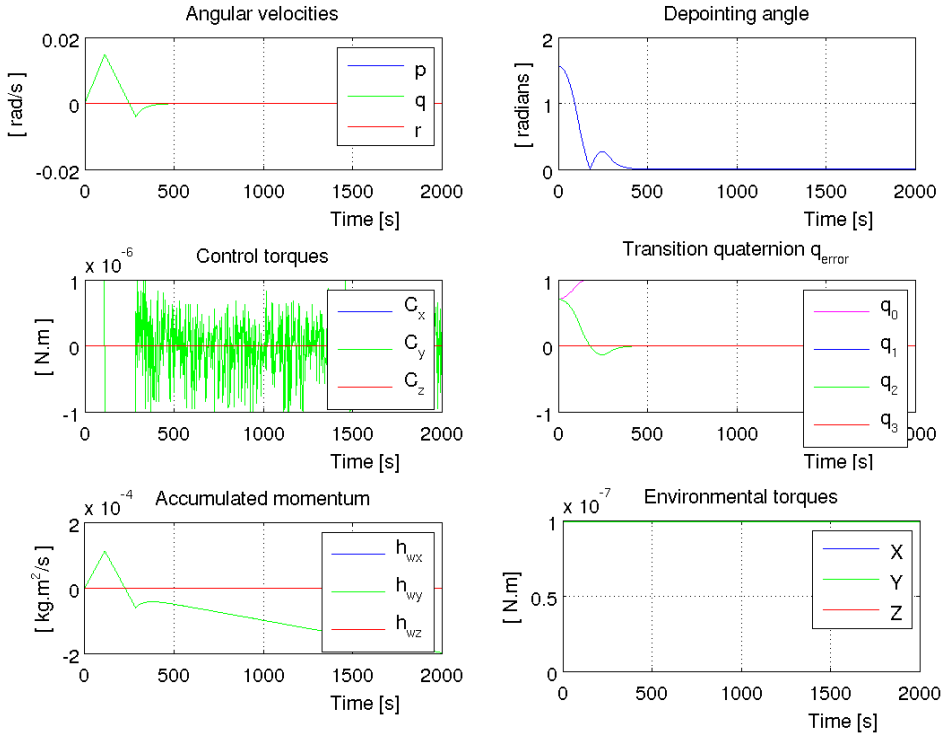

Figure 5.9 – *coupley [0;1;0]*($C_p = 0.005$, $C_d = 0.025$)

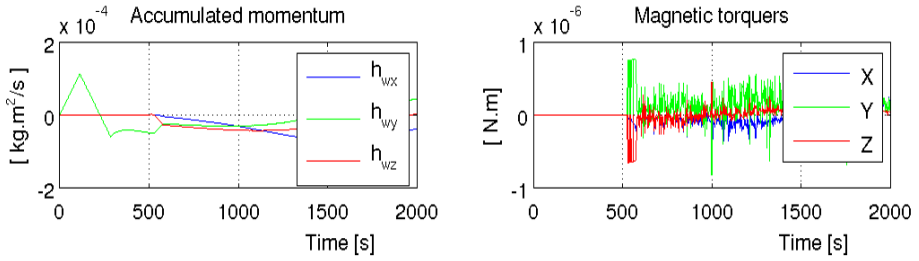

Figure 5.10 – *coupley [0;1;0]*($C_p = 0.005$, $C_d = 0.025$)

For the same reasons as the PID parameters cannot be calculated analytically (see Section 5.3.2), the desaturation control gain is obtained here by "cut-and-try" to get the best obtainable behaviour. Another possibility is to use the general method developed in Section 5.3.3 for a more advanced control. Figure 5.9 illustrates the momentum accumulation in one of the wheel induced by a constant torque along the y-axis. Figure 5.10 shows the momentum unloading using basic control equation for momentum unloading.

The magnetic torquers in the x and y directions also produce parasitic torques which must be handled by the reaction wheels. That is not the main difficulty since the maximum torque of the wheels is greater than that of the magnetic torquers. However, the wheel has to be desaturated while perturbing the attitude as little as possible.

5.5 Attitude model with only magnetic torquers

Most of the algorithms found in the literature assume application of reaction wheels and/or thrusters for three axis stabilization. Attitude control with only magnetic torquers has the significant challenge that the system is not fully controllable. The attitude dynamics can be expressed by Euler's Equations 2.2 :

$$I\frac{d\boldsymbol{\omega}}{dt} = -\boldsymbol{\omega} \times I\boldsymbol{\omega} + T_{coils} + T_{dist}$$

The control torque is constrained to the plane perpendicular to the local geomagnetic field at each time instant with only magnetic torquers. This always leaves an uncontrollable direction parallel to the local field. Nevertheless, attitude stabilisation is possible because magnetic field direction in an inertial space as seen from the spacecraft is varying during the orbit. Orbits with low inclinations can lead to less efficient control since the magnetic field direction is not varying much. Nevertheless, attitude stabilisation is therefore possible because on average the system possesses strong controllability properties for a wide range of orbit inclinations (see for instance Reference [55]).

A basic control law has been set up. The ideal torque is calculated with a proportional derivative controller. The component along the local magnetic field is then removed in order to be applied by the magnetic torquers. An improvement is made by not applying the torque if it differs by an angle of more than 45° as compared to the ideal torque. With no disturbance torques, the attitude can be achieved as seen in Figure 5.11. It takes about one orbit to stabilize with a pointing accuracy of less than 1°.

The maximum magnetic moment developed by the magnetic actuators limits the applied torque. In our case, the maximum control torque is $10^{-6}N.m$ which is handled by a magnetic moment of $5 \cdot 10^{-2}A.m^2$. However an extremely similar behaviour is obtained as long as the possible applied torques do not go below a given threshold of the order of $10^{-7}N.m$ and which increases with the disturbance torques. A bigger magnetic actuator does therefore not improve the attitude control.

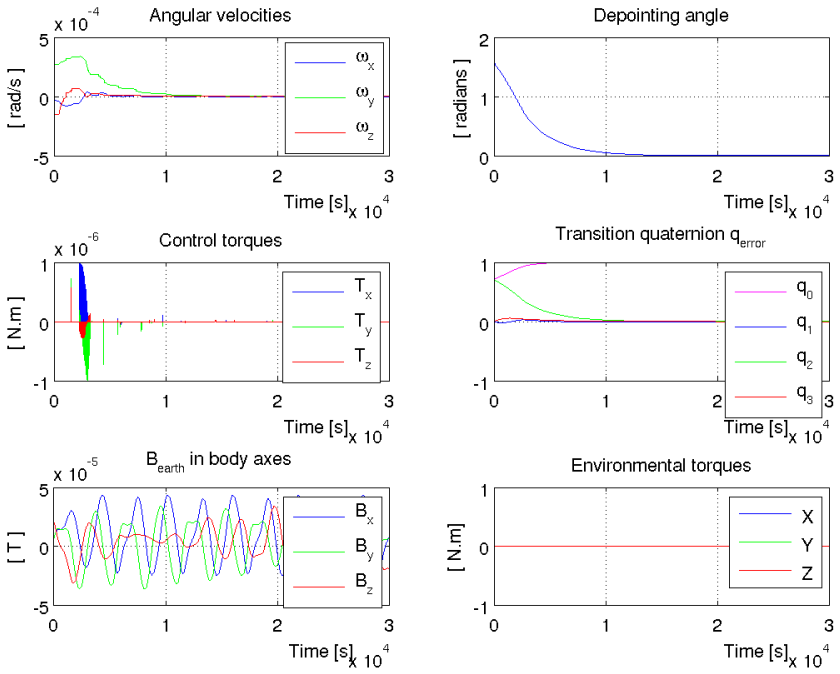

Figure 5.11 – *Attitude manoeuvre with only magnetic torquers and with the assumption that there is no disturbance torque* (Cp=10^{-5}, Cd=$3 \cdot 10^{-2}$)

In a double or triple CubeSat, the gravity gradient tends to be predominant for altitudes higher than 500km, which makes the active control difficult. With the assumptions made concerning the inertia matrix as well as the position of the gravity centre in section 5.3.1, the pointing accuracy is about $1rad$ if only magnetic torquers are used. That result can be seen in Figure 5.12.

It is of main importance to reduce as much as possible the disturbance torques in any three-axis stabilized satellite. Making the assumption that the overall torque has been diminished by a factor of 5, the pointing accuracy is then 8° as shown in Figure 5.13. However reducing the disturbance torque is a nut to crack. On the one hand, mass distribution cannot be strongly changed in order to get close of a spherically symmetric distribution. On the other hand the gravity gradient drag has the same order of magnitude for any low earth orbit.

Another parameter which is of main importance for the obtainable pointing accuracy is the type of orbit. It strongly influences the Earth's useful magnetic field for magnetic torquers. In a low inclination orbit, magnetic torquers will have difficulty to change the satellite's angular momentum component parallel to the Earth's North-South axis due to the magnetic field line directions undergone in its orbit. If the inclination is too low, the average controllability on the orbit can be lost as shown in Figure 5.14.

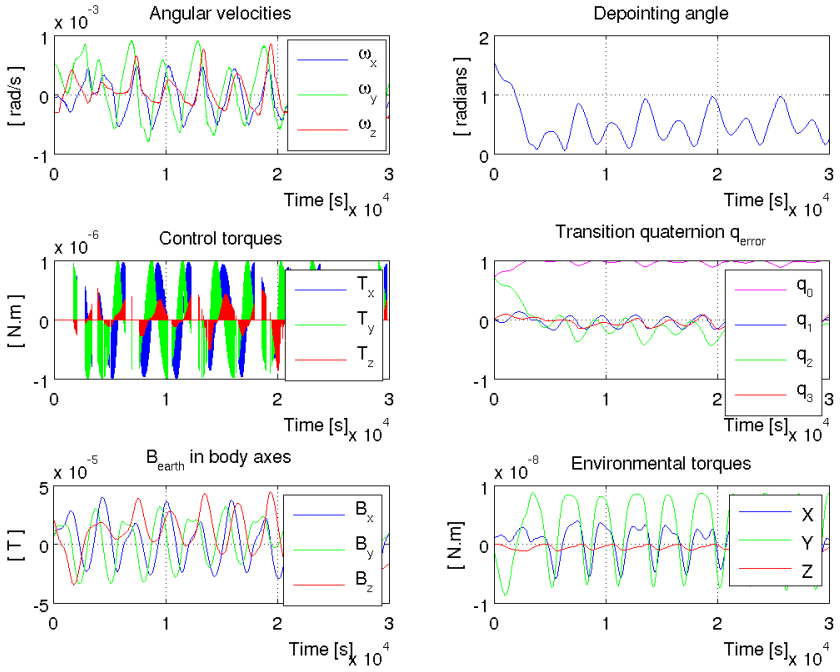

Figure 5.12 – *Attitude manoeuvre with only magnetic torquers and with disturbance torques* (Cp=$2 \cdot 10^{-5}$, Cd=$3 \cdot 10^{-2}$)

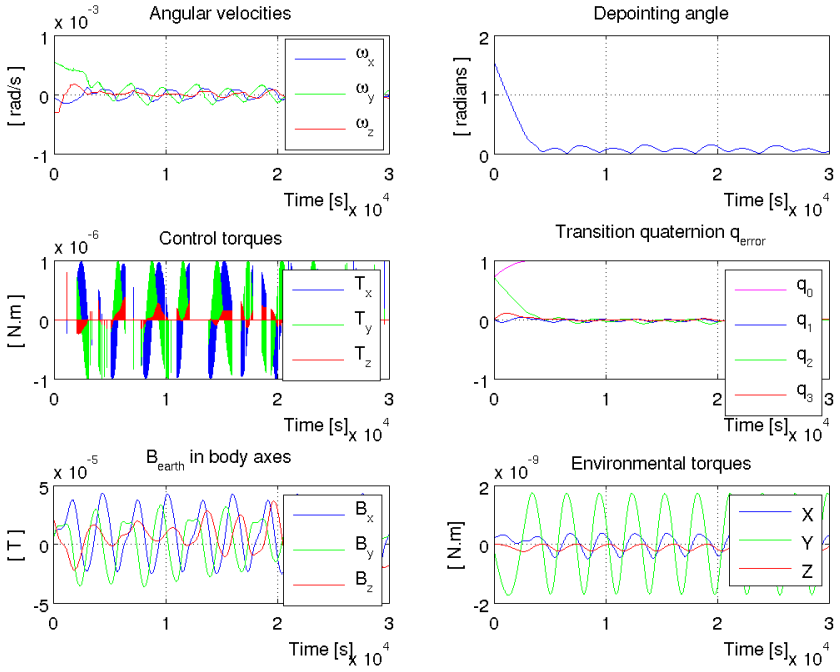

Figure 5.13 – *Attitude manoeuvre with only magnetic torquers and with lowered disturbance torques by a factor of 5* (Cp=$2 \cdot 10^{-5}$, Cd=$3 \cdot 10^{-2}$)

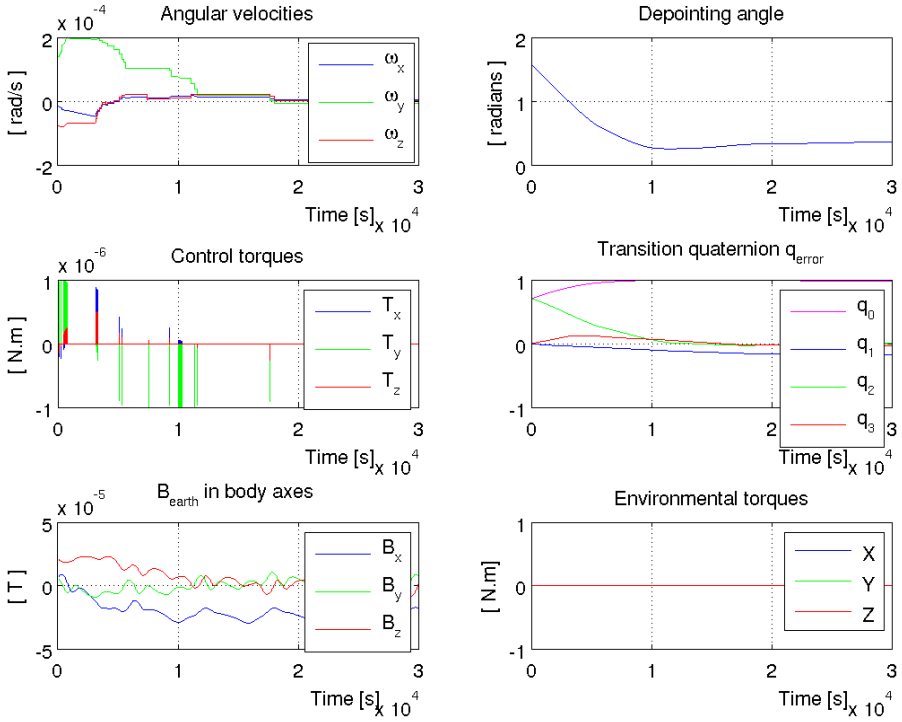

Figure 5.14 – *Manoeuvre on low inclination orbit without torques* (Cp=10^{-5}, Cd=$3 \cdot 10^{-2}$)

5.5.1 Magnetic torquers with one reaction wheel

The magnetic torque acting on the satellite (Equation 2.1) can be written in matrix form as

$$T_{mag} = \begin{pmatrix} 0 & B_z & -B_y \\ -B_z & 0 & B_x \\ B_y & -B_x & 0 \end{pmatrix} \begin{pmatrix} \mu_x \\ \mu_y \\ \mu_z \end{pmatrix}$$

For a desired torque, one must generate the magnetic moment vector $\boldsymbol{\mu} = [\mu_x, \mu_y, \mu_z]^T$. However, the limitations on the possible directions of the magnetic torques is striking by the fact that the matrix is singular. The kernel of this matrix is given by the local magnetic field vector in body axes B(t) which means that at each time instant it is not possible to apply a control torque along the direction of B(t). In order to get full controllability at each time instant, one solution is to replace one magnetic torquer by a reaction wheel (Reference [52]). If a reaction wheel with its axis aligned along the Z body axis, the control equations becomes

$$\begin{pmatrix} T_x \\ T_y \\ T_z \end{pmatrix} = \begin{pmatrix} 0 & B_z & 0 \\ -B_z & 0 & 0 \\ B_y & -B_x & 1 \end{pmatrix} \begin{pmatrix} \mu_x \\ \mu_y \\ \dot{h_w} \end{pmatrix}$$

This matrix becomes invertible as long as B_z differs from zero. A solution with one reaction wheel improves the instantaneous controllability, and it has the advantage of being lighter and cheaper than an ACS with three reaction wheels. That can be useful for particular types of attitude control requirements.

5.6 Conclusion

In the literature, an accuracy of less than five degrees has never been achieved with only magnetic actuators in a nanosatellite. The magnetic torques are constrained on a plane perpendicular to the local magnetic field, which causes problems of controllability. The disturbance torques generate an important depointing angle even though special care is taken to minimize them.

A control law based on a Proportional-Derivative controller has been set up to illustrate the encountered problems when only magnetic actuators are used. The main problem in a double CubeSat comes from the relatively high gravity gradient torques which prevent a good pointing accuracy.

A first study of the use of reaction wheels usage has also been performed. This complicates the ADCS, but simulations shows a much better controllability as well as improved performances.

6 Conclusions

6.1 Future work

6.1.1 OUFTI-1

A design of the PMAS has been developed for the OUFTI-1 nanosatellite. The magnet and the hysteretic materials have been ordered. The magnet does not require any further treatment. The final shaping and heat treatment of the hysteretic rods have still to be performed and the fixations of the magnet and of the hysteretic materials have to be finalized.

Estimations of the stabilization time have been obtained with finite element methods and simulations. The required time to slow down by 0.1 rad/sec is estimated to be about 10 days. To get an accurate estimation, measurements of the hysteresis cycle after shaping and heat treatment should be performed. Mutual influence of the rods could also be studied in the final configuration. A test in a Helmholtz cage could also better characterize the attitude behaviour the satellite will experience in orbit.

6.1.2 OUFTI-2

The use of magnetic torquers alone has been shown to be inefficient to obtain the needed accuracy of 3°. Advanced control laws should be studied further to improve the attitude control, but it is likely that reaction wheels are necessary in addition to magnetic torquers. Little hope is still present for the use of magnetic torquers only if the controller is improved, and if the gravity gradient torque can be reduced drastically.

The use of reaction wheels in addition to magnetic torquers is advisable even though it complicates the ADCS. The reaction wheels would, in addition to improving the pointing accuracy, improve the controllability for the complex manoeuvres. The existing possibilities for reaction wheels have been briefly discussed in chapter 4. An in-depth study is necessary if the reaction wheels must be "home made". That requires an accurate built-in control, and special care must be taken for the hardware (motor and fly wheel).

Concerning the attitude determination, the main issue is the required pointing knowledge of the sun of about 0.1°. This may necessitate a special sensor.

6.2 Miscellaneous activities

For this master thesis, I had the opportunity to participate in different activities.

- Presentation of the OUFTI-1 project at Agoria with Belgian companies and Mr Ganem (President of the Brazilian space agency)
- Participation at a two-day Internal Technical Review at Redu focused on the interfaces between subsystems and functional blocks of OUFTI-1.
- Publication of an article at the URSI forum held in Brussels on May 18, 2010.
- Participation in a seminar held in "Centre Spatial de Liège" on the Delfi nanosatellites.

A

Appendix

A.1 OUFTI-1's parameters

OUFTI-1's Orbit

The orbital parameters for the OUFTI-1 nanosatellite are summarized in Table A.1

Orbit	LEO
Perigee altitude	354 km
Apogee altitude	1447 km
Inclination	71 degrees
Period	100min

Table A.1 – *OUFTI-1's orbital parameters*

Disturbance torques

For a given orbit, the disturbance torques mainly depends on the inertia tensor and the position of the gravity center.

- The inertia tensor of OUFTI-1 used in the simulations is:

$$\underline{J} = \begin{bmatrix} 2.10^{-3} & -5,86.10^{-5} & -1,311.10^{-5} \\ -5,86.10^{-5} & 2.10^{-3} & -1,078.10^{-4} \\ -1,311.10^{-5} & -1,078.10^{-4} & 2.10^{-3} \end{bmatrix} [Kg.m^2]$$

- The gravity centre is approximated to be at coordinates $(10^{-2}, 10^{-2}, 10^{-2})$ in the body frame which is a distance of $\sqrt{3}$ cm from the geometrical centre. The aerodynamic torque and the solar radiation torque are proportional to these coordinates.

A.2 Block diagram for the attitude simulations of a PMAS

The block diagram used for the attitude simulations throughout chapter 3 is shown in Figure A.1. The initial value problem for ordinary differential equations is solved with the "ode45" solver of Matlab.

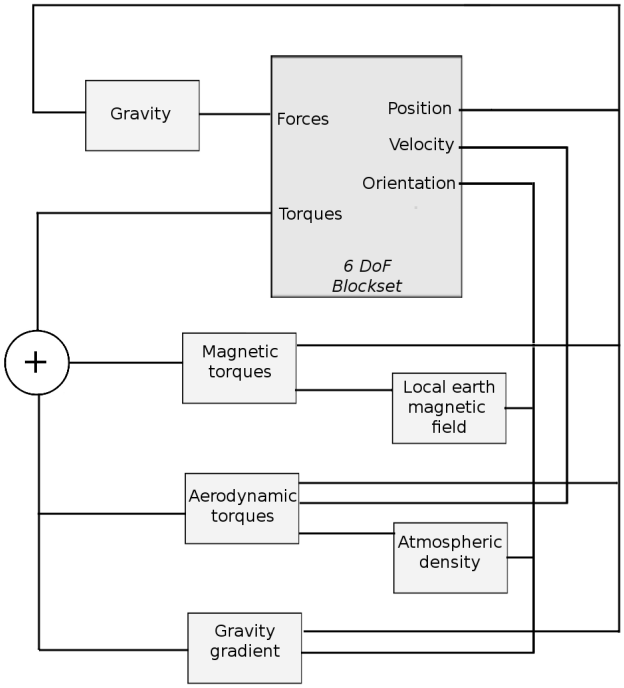

Figure A.1 – *Block diagram for the attitude simulations of a PMAS*

A.3 Finite element methods for magnetostatics problems

In order to study the possible causes of efficiency reduction, finite element methods are developed. That allows to characterize the effect of the demagnetizing field inside the rod (see Section 3.5) as well as the influence of the magnet on the hysteretic rods (see Section 3.6). The programs used are GetDP and Gmsh (References [57] and [58]).

A.3.1 General equations

Equations that relate the electric and magnetic fields to their sources, charge density and current density, are the four Maxwell's partial differential equations.

Name	Differential form	Integral form
Gauss's law	$div\mathbf{D} = \rho_f$	$\iint_{\partial V} \mathbf{D} \cdot \mathrm{d}\mathbf{A} = Q_f(V)$
Gauss's law for magnetism	$div\mathbf{B} = 0$	$\iint_{\partial V} \mathbf{B} \cdot \mathrm{d}\mathbf{A} = 0$
Faraday's law of induction	$curl\mathbf{E} = -\frac{\partial \mathbf{B}}{\partial t}$	$\oint_{\partial S} \mathbf{E} \cdot \mathrm{d}\mathbf{l} = -\frac{\partial \Phi_{B,S}}{\partial t}$
Ampère's law	$curl\mathbf{H} = \mathbf{J}_f + \frac{\partial \mathbf{D}}{\partial t}$	$\oint_{\partial S} \mathbf{H} \cdot \mathrm{d}\mathbf{l} = I_{f,S} + \frac{\partial \Phi_{D,S}}{\partial t}$

Table A.2 – *Maxwell's equations*

- $\boldsymbol{H}$ is the magnetic field ($[A/m]$)
- $\boldsymbol{B}$ is the magnetic induction field ($[T]$)
- $\boldsymbol{E}$ the electrical field ($[V/m]$)

- $\boldsymbol{D}$ the electrical displacement ($[C/m^2]$)
- $\boldsymbol{j}$ the current density ($[A/m^2]$)
- ρ which is the volume charge density ($[C/m^3]$)

The constitutive equations are given by

$$\begin{cases} \boldsymbol{B} = \mu \boldsymbol{H} \\ \boldsymbol{D} = \epsilon \boldsymbol{E} \\ \boldsymbol{j} = \sigma \boldsymbol{E} \end{cases}$$

with

- μ the permeability (H/m)
- ϵ the permittivity (F/m)
- σ the conductivity (S/m)

The Maxwell equations simplify in the case of magnetostatics to

$$curl\boldsymbol{H} = \boldsymbol{j} \tag{A.1}$$

$$div\boldsymbol{B} = 0 \tag{A.2}$$

The boundary conditions between two media are

$$\boldsymbol{n} \wedge \boldsymbol{H}|_\Gamma = \boldsymbol{j_s}$$

$$\boldsymbol{n}.\boldsymbol{B}|_\Gamma = 0$$

with j_s the surface current density.

Two finite element formulations will be developed to solve the magnetostatics problems: the scalar potential formulation and the vector potential formulation. The first one provides theoretically a lower bound of the field while the second provides an upper bound. This is valid on average over the whole domain, but it can be assumed locally in a good approximation. The comparison of the two methods is a good way to get an idea of the results accuracy.

A.3.2 The scalar potential phi formulation

If $j = o$ on Ω, the problem simplifies and Equation A.1 is equivalent to

$$H = -grad\phi$$

Therefore Equation A.2 can be written as

$$div\Big(\mu(-grad\phi)\Big) = 0 \tag{A.3}$$

This further simplifies to the Laplace equation if μ is a constant

$$\Delta\phi = 0$$

where Δ is the Laplace operator.

Equation A.3 can be written as a weak formulation. We look for ϕ such that the relation

$$\int_\Omega (div\ (\mu grad\phi)) \cdot \phi' d\Omega = 0$$

holds for all the test functions ϕ' belonging to the same space $F_h^0(\Omega)$ than ϕ. This can then be rewritten as

$$-\int_\Omega \mu \cdot grad\phi \cdot grad\phi' d\Omega + \int_{d\Omega} \mu \cdot \boldsymbol{n} \cdot grad\phi \cdot \phi' d\Gamma = 0$$

Taking into account the boundary conditions, one gets

$$-\int_\Omega \mu \cdot grad\phi \cdot grad\phi' d\Omega = 0$$

This is the weak formulation of the scalar potential phi formulation. The magnetostatics problem can be solved with that formulation using GetDp. The resolution is done by using piecewise polynomial functions s_n defined on the mesh (the simplest is piecewise linear functions). The space $F_h^0(\Omega)$ describing ϕ and ϕ' becomes $S_h^0(\Omega)$ and we describe ϕ as

$$\phi = \sum_{n=1}^{n=N} \phi_n s_n$$

where N is the total number of nodes and ϕ_n are the unknowns. The ϕ_n corresponding to the boundary nodes are fixed by the boundary conditions. The discrete weak formulation becomes

$$-\int_\Omega \mu \cdot grad(\sum_{n=1}^{n=N} \phi_n s_n) \cdot grads_m d\Omega = 0$$

$\forall s_m, m = 1, ..., N$ with the corresponding value not fixed by the boundary conditions. The result is a set of equations for the unknown s_n.

If $j \neq 0$, there are two possibilities.

a) Where j=0, we have $h = -grad\phi$ and the previous method can be used on a simply connected domain. We then cut the domain into different simply connected domains. Sources of magnetic field can be supported by applying discontinuities or "cuts" to the potential field. The source j can then be applied at the discontinuity.

b) The current density j is written as $curl\ h_s$ and we then have $curl\ h - curl\ h_s = 0$

A.3.3 The vector potential a formulation

From Equation A.2, the magnetic induction can be written as a function of a potential vector.

$$\boldsymbol{B} = rot\boldsymbol{a}$$

Therefore Equation A.1 can be written as

$$rot\Big(\frac{1}{\mu}(rot\boldsymbol{a})\Big) = j \tag{A.4}$$

If μ is a constant, this further simplifies to the Laplace's equation using the Coulomb gauge ($\boldsymbol{\nabla a} = 0$)

$$\Delta \boldsymbol{a} = \mu \boldsymbol{j}$$

The Method of Weighted Residuals is hereby explained to solve Equation A.4. We wish to approximate $\boldsymbol{a}$ on the domain by a linear combination of edge basis functions. That is,

$$\boldsymbol{a} = \sum a_i \boldsymbol{s_i}$$

- a_i is the circulation of a on the edge i.
- $\boldsymbol{s_i}$ is the form function associated to edge i. It is a vectorial function with the following properties
  - Its circulation along edge ij is 1
  - Its circulation along all other edges is 0
  - Its value is non-zero only on the elements which has ij as an edge.

The circulation of the potential vector $\boldsymbol{a}$ around a closed curve represents the magnetic induction flux which goes through this curve. In one element of the mesh,

$$\oint_{\partial S} \mathbf{a} \cdot \mathrm{d}\mathbf{l} = \Phi_{B,S}$$

The unknowns are the $\Phi_{B,S}$. Equivalently, the potential vector $\boldsymbol{a}$ on the edges can be used. For the potential vector formulation a tree which covers the whole graph is built on the mesh. The tree is created so that it can include the boundary conditions. The remaining a_i on the edges of the tree are set to zero. The unknowns are on the co-tree and are in a number equal to the surface elements of the mesh.

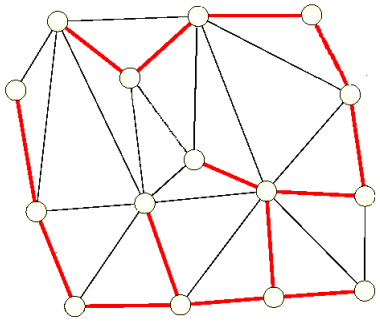

Figure A.2 – *Example of a 2D-Tree. This one does not include the whole boundary* Γ *of the domain*

In practice, a zero value can be fixed for all circulations along edges of a tree which includes the boundary.

The weak formulation is now developed to solve the magnetostatics problem numerically. The Ampere's law can be written as:

$$\int_{\Omega} (curl\ \boldsymbol{H} - \boldsymbol{j}) \cdot \boldsymbol{a'} d\Omega = 0$$

where $\boldsymbol{a'}$ is the test function. The method which consists in cancelling on average this equation on the design domain Ω is known as the method of 'weighted residuals'. One can use the same shape functions and the same interpolation functions. It is then called the 'Galerkin method'.

Applying the second Green formula, one gets the following form:

$$\int_\Omega \boldsymbol{H} \cdot curl\ \boldsymbol{a'} d\Omega - \int_\Gamma \boldsymbol{H} \wedge \boldsymbol{n} \cdot \boldsymbol{a'} d\Gamma - \int_\Omega \boldsymbol{j} \cdot \boldsymbol{a'} d\Omega = 0$$

The tree is imposed to include the boundary Γ where

$$\boldsymbol{n} \wedge \boldsymbol{H}|_\Gamma = 0$$

It follows

$$\int_\Omega \frac{1}{\mu}\ curl\ \boldsymbol{a} \cdot curl\ \boldsymbol{a'} d\Omega - \int_\Omega \boldsymbol{j} \cdot \boldsymbol{a'}\ d\Omega = 0$$

$$\int_\Omega \frac{1}{\mu}\ curl\ \sum a_i \boldsymbol{s_i} \cdot curl\ \boldsymbol{s_j}\ d\Omega - \int_\Omega \boldsymbol{j} \cdot \boldsymbol{s_j}\ d\Omega = 0, \forall j$$

$$\sum a_i \int_\Omega \frac{1}{\mu} curl\ \boldsymbol{s_i} \cdot curl\ \boldsymbol{s_j}\ d\Omega = \int_\Omega \boldsymbol{j} \cdot \boldsymbol{s_j}\ d\Omega, \forall j$$

The result is a set of n equations for the n unknowns a_i .

A.4 Exploded view of OUFTI-1 nanosatellite

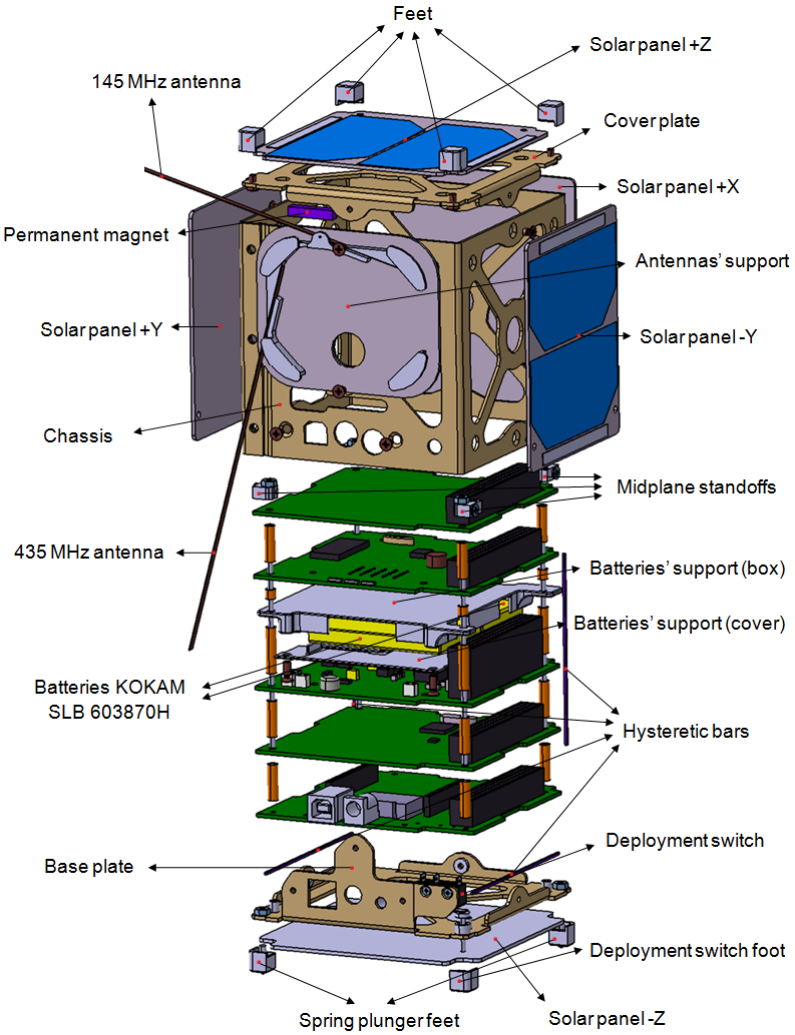

Figure A.3 – *Detailed exploded view of OUFTI-1 nanosatellite (Reference [25])*

List of Figures

List of Tables

Bibliography

[1] V. Beukelaers, *From mission analysis to space flight simulation of the OUFTI-1 nano-satellite*, Master thesis report, University of Liège, 2009 (cited on pp 10, 94)

[2] S. Hannay, *Modelling of the attitude control of the nanosatellite OUFTI 1*, Master thesis report, University of Liège, 2009 (cited on pp 11, 13, 18, 31)

[3] The MathWorks, *Aerospace Blockset User's Guide*, 2008. (cited on pp 15, 97)

[4] *http://www.esa.int/* (cited on pp 18, 94)

[5] P. Rajendra Prasard et al, *Review of air density models for orbit determination*, ISRO Satellite Centre, India (cited on p 19)

[6] C. Geuzaine, *Modeling and design of electromagnetic systems*, Lecture notes, 2009-2010

[7] G. Kerschen, *Satellite Engineering*, Lecture notes, 2009

[8] P. Rochus, *Conception d'expériences spatiales*, Lecture notes, 2009-2010

[9] A. Genon, *Conception assistée par ordinateur du matériel électrique*, Notes de cours, 2004

[10] Magnetic Materials producers association, *Standard spacifications for permanent magnet materials*, Chicago, USA (cited on p 24)

[11] F. Poppenk, *Design and Testing of a Attitude Control System of a Nano Satellite*, Delft university of Technology, The Netherlands (cited on pp 26, 39, 46, 95)

[12] J-F Levesque, *Passive Magnetic Attitude Stabilization using Hysteresis Materials*, Technical report, MS., Intelligent Systems, Mechatronics and Aerospace (SIgMA) (cited on p 26)

[13] A. Mercadante and L. Jacques, *Déploiement des antennes d'OUFTI-1*, Technical report, University of Liège, 2009 (cited on p 28)

[14] Hoffait S. and Brüls O., *Etude du déploiement des antennes de OUFTI-1*, Technical report, University of Liège, 2009 (cited on pp 29, 30, 94)

[15] Polytechnical School of Lausanne, *SwissCube, : http://swisscube.epfl.ch/*, Switzerland (cited on pp 29, 30, 94)

[16] J. Wertz, *Conception et réalisation du système de déploiement des antennes du nanosatellite OUFTI-1*, Master thesis report, University of Liege, 2009 (cited on pp 30, 94)

[17] A. Denis and J. Pisane, *OUFTI-1 Phase A: Mission definition, Space and ground systems description*, September 2009 (cited on pp 30, 94)

[18] K. Nadjet, *Modélisation de l'hystérésis magnétique en vue de son intégration dans un code de calcul de champ électromagnétique*, Thèse de doctorat, Université de Batna, 2006 (cited on p 31)

[19] Vacuumschmelze GMBH & Co. KG, *Soft Magnetic and Semifinished Products*, Edition 2002 (cited on pp 31, 52, 95)

[20] B.D. Cullety and C.D. Graham, *Introduction to Magnetic Materials*, IEEE Press (cited on p 32)

[21] M.Yu.Ovchinnikov and V.I.Penkov, *Passive Magnetic Attitude Control System for the Munin Nanosatellite*, Cosmic Research, Vol.40, No. 2, 2002, pp 142-156 (cited on p 33)

[22] M. Sato and Y. Ishii, *Simple and approximate expressions of demagnetizing factors of uniformly magnetized rectangular rod and cylinder*, Journal of Applied Physics 66, 1989 (cited on p 34)

[23] F. Santoni and M. Zelli, *Passive magnetic attitude stabilization of the UNISAT-4 microsatellite*, Elsevier Science Ltd., 2009 (cited on pp 36, 51)

[24] M. Raif et al, *Dynamic System Simulation of Small Satellite Projects*, 60th International Astronautical Congress, Daejong, Republic of Korea, 2009 (cited on pp 40, 46)

[25] N. François, *Dynamic Analysis and Launch Qualification of OUFTI-1 Nanosatellite*, Master thesis report, University of Liège, 2010 (cited on pp 49, 93, 95, 96)

[26] Vacuumschmelze GMBH & Co. KG, *Our soft magnetic alloys*, Brochure, Edition 2001 (cited on p 51)

[27] Dexter Magnetic Technologies, *Permanent magnet catalog, www.dextermag.com*

[28] Magnet Sales and Manufacturing Inc., *High Performance Permanent Magnets*, Culver City, USA

[29] California Polytechnic State University, *Cubesat design specification*, eleventh revision, 2008

[30] California Polytechnic State University, *Cubesat design specification*, twelfth revision, 2009

[31] A. Denis. *Progress report for OUFTI-1*, tenth edition. Technical report, University of Liège, BELGIUM, October 2009

[32] A. Denis. *Progress report for OUFTI-1*, eleventh edition. Technical report, University of Liège, BELGIUM, November 2009

[33] A. Denis. *Progress report for OUFTI-1*, twelfth edition. Technical report, University of Liège, BELGIUM, December 2009

[34] A. Denis. *Progress report for OUFTI-1*, thirteenth edition. Technical report, University of Liège, BELGIUM, January 2010

[35] A. Denis. *Progress report for OUFTI-1*, fourteenth edition. Technical report, University of Liège, BELGIUM, February 2010

[36] A. Denis. *Progress report for OUFTI-1*, fifteenth edition. Technical report, University of Liège, BELGIUM, March 2010

[37] A. Denis. *Progress report for OUFTI-1*, sixteenth edition. Technical report, University of Liège, BELGIUM, April 2010

[38] *http://www.cubesatkit.com/*

[39] G. Bovens, *Modélisation du système de contrôle d'attitude et d'orbite du satellite PROBA-2*, Master thesis report, University of Liège, 2006

[40] R. Wisniewski, *Satellite attitude control using only electromagnetic actuation*, PhD thesis, Aalborg university, Denmark

[41] A. Foletti and Piyawat Kaewkerd, *Phase A of ADCS report*, Ecole polytechnique de Lausanne, 2006

[42] B. Despont, *Phase B : System Engineering and development and test of the ADCS breadboard for SwissCube*, Ecole polytechnique de Lausanne, 2007

[43] H. Péter-Contesse, *Phase B/C : ADCS System and hardware*, Ecole polytechnique de Lausanne, 2007

[44] University of Toronto, *CanX2 : http://www.utias-sfl.net/nanosatellites/CanX2/*, Canada

[45] Technical University of Denmark *DTUsat-1 : http://dtusat1.dtusat.dtu.dk/*, Denmark

[46] Aalborg University, *AAU Cubesat : http://www.aausatii.auc.dk/*, Denmark

[47] University of Michigan, *M-Cubed: http://umcubed.org/*, USA

[48] University of Illionis *ION : http://courses.ece.uiuc.edu/cubesat/*, USA

[49] *http://www.sinclairinterplanetary.com/* (cited on pp 65, 96)

[50] J.R. Wertz et al, *Spacecraft Attitude Determination and Control*, 1978 (cited on pp 59, 78)

[51] Zarm Technik, *Magnetic Torquers for CubeSat application*, brochure, 2009 (cited on pp 64, 96)

[52] M.J. Sidi, *Spacecraft Dynamics and Control : a practical engineering approach*, Cambridge university press, 1997 (cited on pp 74, 83)

[53] P. Fortescue, J. Stark and G. Swinerd, *Spacecraft Systems Engineering*, Third Edition, 2003

[54] B. Hassibi, A.H. Sayed and Thomas Kailath, *A unified approach to H^2 and H^∞ theory*, Society for Industrial and applied mathematics, philadelphia, USA (cited on p 75)

[55] M. Loveraa and A. Astolyb, *Spacecraft attitude control using magnetic actuators*, Elsevier Science Ltd., 2004 (cited on p 80)

[56] M.L. Psiaki, *Magnetic torquer attitude control via asymptotic periodic linear quadratic regulation*, Cornell University, Ithaca, USA, 2000

[57] P. Dular and C. Geuzaine, *GetDP : a general environment for the treatment of discrete problems, http://www.geuz.org/getdp/* (cited on p 88)

[58] C Geuzaine and J-F Remacle, *Gmsh: a three-dimensional finite element mesh generator with built-in pre- and post-processing facilities, http://geuz.org/gmsh/* (cited on p 88)